Phenomenology and Technology in Support of Sub-Terahertz Radar Systems

by

Amr Ibrahim

A dissertation submitted in partial fulfillment
of the requirements for the degree of
Doctor of Philosophy
(Electrical Engineering)
in the University of Michigan
2017

Doctoral Committee:
Porfessor Kamal Sarabandi, Chair
Professor Ehsan Afshari
Professor Anthony Grbic
Professor Jerome P. Lynch

Amr Ibrahim

amralaa@umich.edu

ORCID iD: 0000-0003-4354-211X

© Amr Ibrahim 2017

DEDICATION

To the one who first taught me that the physical meaning always come first, Iman El-Sawy,
a loving mother and exceptional electrical engineer

ACKNOWLEDGMENTS

First and foremost, I would like to thank god for giving me the perseverance to endure this long journey. Without his guidance, I would not have been able to make it through successfully. Second, I would like to sincerely thank my adviser, Prof. Kamal Sarabandi, for recognizing my potential and helping me to realize it throughout my graduate study. This thesis would not be possible without the endless hours of discussion we had in his office. He is an exceptional engineer and an amazing mentor. I am deeply grateful for my thesis committee members; Professor Anthony Grbic, Professor Ehsan Afshari, and Professor Jerome Lynch for their valuable comments to improve the thesis.

I would like to extend my gratitude to all current and former Radlab members, especially, Armin Jam, Hatim Bokhary, Walid Alomar, Abdulrahman Alaqeel, Faris Alsolamy, Michael Benson, Shang-Hua Yang, Jihun Choi, Meysam Moallem, Jungsuek Oh, Behzad Yektakhah, Nikolaos Chiotellis, Xiuzhang Cai, Navid Barani, Michael Giallorenzo, Mani Kashanianfard, Jiangfeng Wu, Young Jun Song, and Fikadu Dagefu. Special thanks go to my Egyptian friends; Mostafa Zaky, Omar Bakry, Mahmoud Moneeb, and Mohamed Banani for all of the fun and delicious meals we had together. I think that is what kept me sane during the past five years.

Experimental setups could not be possible without the help of Dr. Adib Nashashibi. I can not thank him enough for his help with fabricating lots of hardware component in the machine shop. He was more than a friend to me and I learned a lot from him. As for software issues, Dr. Leland Pierce was the first person to come to mind. His experience with many programming languages is just remarkable. I would like also to acknowledge all the staff and users in the Lurie nanofabrication facility (LNF), especially, Rob Hower, Pilar Herrera-Fierro, Nadine Wang, Katharine Beach, Greg Allion, Kevin Owen, Brian Armstrong, Shawn Wright, David Sebastian, Matthew Oonk, and Anthony Sebastian for all of their assistance, valuable ideas, and recommendations for the microfabrication process. A special thanks is also extended to all the Radlab staff including Jennifer Feneley, and Michelle Chapman. They made the Radlab a truly welcoming environment. I also do not want to forget our graduate coordinator, José-Antonio Rubio. He is a very friendly person and has a magical ability to lift your spirit whenever you feel down.

I am truly grateful for my wife, Sama Tarek, for her unconditional love and support. She joined me at the last year of my Ph.D. journey when I was the most busy and she was indeed a great source of motivation and encouragement. Finally, words cannot express my gratitude to my family. I could not have been this person if it was not for them; my parents Iman El-Sawy and Alaaeldin Ibrahim, my brother Mohamed, and my sister Abrar. To them I owe everything that I have achieved in my life.

TABLE OF CONTENTS

Chapter II. Simulation of Long Distance Wave Propagation in 2D Sparse Random Media: A Statistical S-Matrix Approach in Spectral Domain 19

LIST OF FIGURES

LIST OF TABLES

LIST OF ABBREVIATIONS

ACC	Adaptive Cruise Control
ACF	Angular Correlation Function
BiCMOS	Bipolar CMOS
CMOS	Complementary Metal Oxide Semiconductor
DAS	Driver Assistant Systems
DFT	Discrete Fourier Transform
DRIE	Deep Reactive Ion Etching
eWLB	embedded Wafer Level Ball grid array
FEM	Finite Element Method
FFT-BPM	Fast Fourier Transform - Beam Propagation Method
FoM	Figure of Merit
FoV	Field of View
GaAs	Gallium Arsenide

GaN	Gallium Nitride
HBTs	Heterojunction Bipolar Transistors
HEMT	High Electron Mobility Transistor
IACT	Isolated Antenna Calibration Technique
InP	Indium Phosphide
MEFSS	Miniaturized-Element Frequency Selective Surface
MESFET	Metal Semiconductor Field Effect Transistor
MMIC	Monolithic Microwave Integrated Circuits
MMW	Millimeter-wave
PDF	Probability Density Function
PEC	Perfect Electric Conductor
pHEMT	pseudomorphic-HEMT
PMC	Perfect Magnetic Conductor
PSD	Power Spectral Density
PZT	Lead Zirconate Titanate
RADAR	Radio Detection and Ranging
RCS	Radar Cross Section

SAR	Synthetic Aperture Radar
SiGe	Silicon Germanium
SSWaP-SD	Statistical S-matrix Approach for Wave Propagation in Spectral Domain
Sub-THz	Sub- Terahertz
THz-TDS	Terahertz - Time Domain Spectroscopy
UWB	Ultra Wideband
VNA	Vector Network Analyzer

ABSTRACT

Sub-terahertz (Sub-THz) systems operate at the border of electronics and photonics, and have profited from the development of both fields. One of the main driving forces to develop such systems originates from security applications and, in particular, stand-off imaging of persons and hidden objects. Other important applications include very high speed, short distance, line-of-sight communication links, as well as short-range navigation radars used in vehicles and aircrafts. These systems have the potential to approach the resolution of optical imaging systems while operating under adverse conditions of weather.

Based on these applications and the potential for improved performance, the main theme of this thesis is to investigate and characterize the unique advantages as well as performance limitations of such systems working around 240 GHz in typical outdoor environments. The research has three main directions. The first direction is the development of novel scattering models that can accurately describe the propagation of electromagnetic waves in realistic communication channels. Specifically, a semi-numerical propagation model is developed to predict the attenuation as well as the back scattered power from 2D, very long, discrete, sparse random media. Such sparse random media can be used, in general, to model environments like rain, snow, or dust. The model is named Statistical S-matrix Approach for Wave Propagation in Spectral Domain, or SSWaP-SD in short. The advantage of this model is that it is a coherent one, and it can capture the multiple interactions of the electromagnetic wave with the scattering particles to all orders. Being a coherent model, it is then extended to study the degradation in imaging resolution for a Synthetic Aperture Radar (SAR) working in such rainy environments. The second direction is related to the characterization of different synthetic and artificial targets found in typical radar environments. In this part, a free-space, transmission-only, dielectric characterization setup is custom built to measure the dielectric constant of different fabric materials (wool, polyester, jeans, etc). Such measurements are important in the context of concealed object detection algorithms. In addition, a fully polarimetric, network analyzer-based instrumentation radar system working at 222 GHz is built to characterize the back scattering coefficient of different natural and synthetic rough surfaces found in typical outdoor driving environments like asphalt, concrete, grass, etc. The third direction of the research is related to the development of a major component of an electronic beam-steering radar which is the phase shifter. Specifically, a rectangular waveguide-based phase shifter is designed to provide 360^{o} variable phase shift at 240 GHz. The proposed structure relies on mechanically actuating a tunable perfect magnetic conductor (PMC) inside a modified TE_{10} rectangular waveguide. A prototype is manufactured using silicon micro-fabrication techniques and the PMC is actuated electrically using an external piezoelectric actuator. The proposed phase shifter shows very small insertion loss which is important for realizing high efficiency electronic beam-steering antennas at sub-THz frequencies.

CHAPTER I

Introduction

The word “RADAR” stands for Radio Detection and Ranging. In its most basic form, a radar system is simply an electromagnetic sensor that is used for detecting and locating different reflecting objects. It does that by radiating energy into space and detecting the echo signal from different targets. By comparing the echo signal with the transmitted signal, the target range as well as other target-related information can be inferred. The ability of the radar to perform such a function in all-weather conditions is what distinguish it from other imaging sensors.

The basic principle of a radar is shown in Fig.1.1. A transmitter generates an electromagnetic signal that is radiated in free space by an antenna. Part of the transmitted energy is intercepted by the target and re-radiated back in many directions including the radar direction. The re-radiated energy towards the radar is collected by the radar antenna, and delivered to the receiver. By processing the received signal, the presence of the target can be detected, as well as its radial range from the radar. The range can be simply calculated by measuring the time delay between the transmitted pulse and the echo pulse. The target location in azimuthal and elevation angles can be found from the the direction of the narrow-beamwidth radar antenna when the received echo signal is maximum in amplitude.

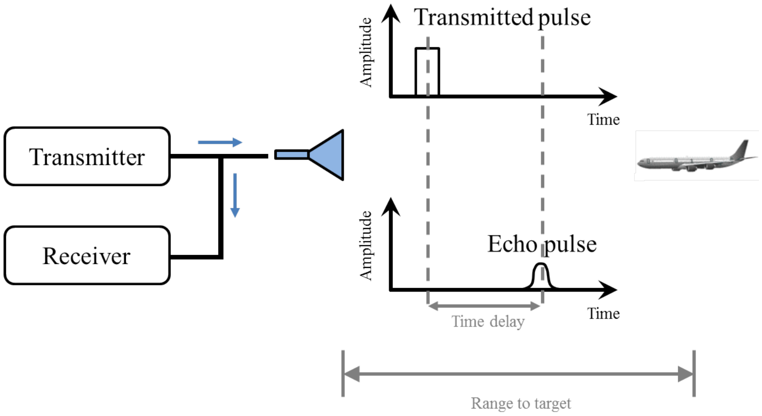

Figure 1.1: Basic Principle of a radar.

In this way, a radar system can produce a 3D image of the scene of interest.

The most important parameter of any imaging system is the resolution which basically characterizes the ability of the system to discriminate between two nearby objects. In radar terminology, there are two types of resolutions as shown in Fig.1.2. The first type is called the range resolution. This resolution describes the ability of the radar to distinguish between two objects at slightly different ranges given that the antenna beam is fixed in a specific direction. From Fig.1.2(a), we can immediately see that this resolution is related to the pulse duration. If long pulses are used, then the two returned echo pulses from two nearby objects will overlap in the time domain and the radar will 'see' the two targets as a bigger single target. On the other hand, if short pulses are transmitted, then the two echo pulses can be easily distinguished apart in the received signal. Mathematically, the radar range resolution is given by [1]–[3]:

$$\Delta R_r \propto \frac{cT_R}{2} = \frac{c}{2 \times BW} \tag{1.1}$$

where $c = 3 \times 10^8$ m/s is the speed of light, T_R is the transmitted pulse duration and BW is the system bandwidth which is also the inverse of the pulse duration. It can be seen from (1.1) that the only way to increase the radar range resolution is through increasing the system bandwidth. It is also important to emphasize here that larger bandwidth can be easily achieved at higher center frequency compared to lower center frequency (i.e. having a 1 GHz bandwidth at 100 GHz center frequency is much easier to design than a 1 GHz bandwidth at 3 GHz center frequency). The second type of resolution is called the cross-range resolution which is shown in Fig.1.2(b). It describes the ability of the radar to distinguish between two nearby targets at the same range, but slightly different azimuthal or elevation angles. This resolution is directly related to the radar antenna beamwidth. Mathematically, we have [1]–[3]:

$$\Delta R_c \propto Antenna\, Beamwidth \times Range = \frac{D}{\lambda} \times Range = \frac{D \times f}{c} \times Range \qquad (1.2)$$

where D is usually taken to be the largest dimension of the radar antenna (e.g. length of a dipole antenna, or diameter of dish antenna), λ is the operating wavelength, and f is the frequency . From the previous equation , the radar cross-range resolution can be enhanced by either increasing the antenna size at a fixed frequency, or increasing the operating frequency for a fixed antenna size.

Depending on the application, usually the radar system has many constraints in terms of size, weight, power consumption ...etc. By looking at equations (1.1) and (1.2), it can be concluded that increasing the operating frequency is a good candidate for enhancing both the range- and cross-range resolutions. A logical question to ask at this point is wither there is a limitation on how large the operating frequency can be increased. To answer

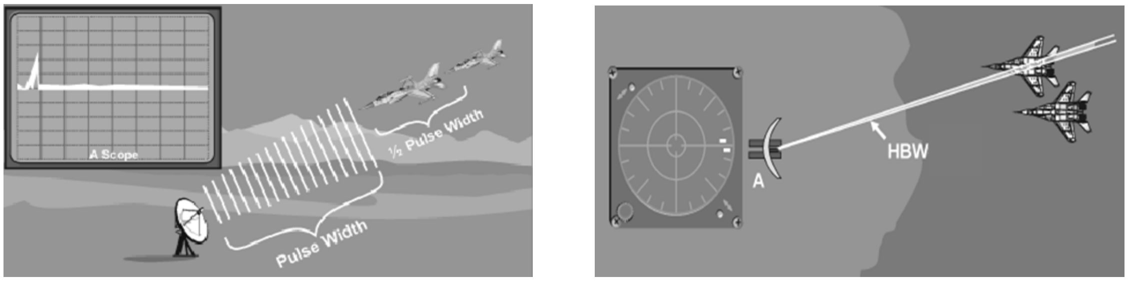

(a) (b)

Figure 1.2: Radar resolution: (a) Range resolution. (b) Cross-range resolution.

this question, let us examine Fig.1.3 which represents the atmospheric attenuation of the electromagnetic energy versus frequency. The attenuation curve is characterized by number of peaks which corresponds to the molecular resonance of the different gases comprising the atmosphere. For example, the water vapor has a molecular resonance at 22 GHz, while the oxygen molecule has multiple resonances including 60, 118, and 183 GHz. Between these peaks, there are valleys commonly referred to as 'atmospheric windows'. Most of the high frequency radar systems operate at these atmospheric windows to take advantage of the minimal atmospheric attenuation. For example, Ka-band radars operate around 35 GHz, while the majority of the automotive radars operate around 77 GHz. It can also be seen from the figure that there is a nice wide atmospheric window around 240 GHz with attenuation on the order of 1.5 dB/km. The next atmospheric windows are relatively narrow and they suffer from considerable atmospheric attenuation on the order of 10 dB/km. Thus, we conclude that there is an upper limitation on the radar operating frequency imposed by the atmospheric attenuation. The focus of this thesis is to investigate the potential of sub-THz radars operating around 240 GHz for relatively short range applications.

It is important to emphasize here there is no agreement in the literature on the definition of terahertz frequency bands [4]–[7]. Here, we will adapt the common definition of the frequency

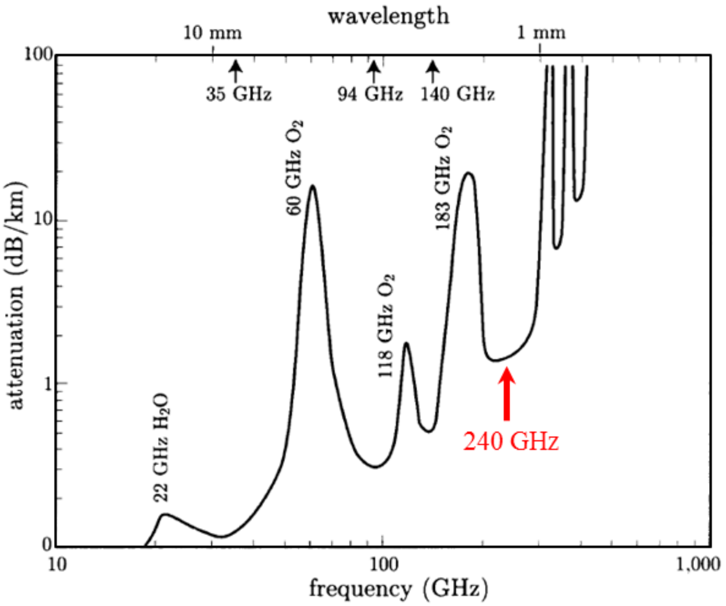

Figure 1.3: Attenuation of the electromagnetic wave due to propagation in the atmosphere versus frequency [8].

band spanning from 0.1 THz to 10 THz. On the other hand, the Millimeter-wave (MMW) frequency band is commonly used to refer to the band spanning from 30 GHz to 300 GHz. For radar systems operating in the range between 100 GHz and 300 GHz, they are sometimes referred to as sub-MMW or sub-THz systems. In this thesis, we will use these two terms synonymously.

1.1 Sub-THz Radar Technology

For the past century, the development of radar systems has been supported predominantly for their military applications. The implementation of the early systems made extensive use of waveguide technology which was bulky, heavy, expensive and not well suited to high production volume. With the advent of Monolithic Microwave Integrated Circuits (MMIC), novel scientific and commercial applications have emerged. Traditionally, expensive III-V semiconductor chipsets and discrete components have been used to implement front-ends in the MMW domain. This includes (GaAs), Indium Phosphide (InP), and more recently Gallium Nitride (GaN). GaAs has long been recognized for its advantages at high frequencies. The GaAs technology can offer benefits in terms of signal gain, power delivering capabilities, and noise performance making it very attractive for MMW applications. Initial GaAs circuit developments were based on the Metal Semiconductor Field Effect Transistor (MESFET). Over time, a number of more sophisticated GaAs based field effect transistor devices, such as the High Electron Mobility Transistor (HEMT) and pseudomorphic-HEMT (pHEMT), have evolved. These have more complex material layering structures than the conventional MESFET, which improve further their high frequency characteristics. GaAs based bipolar transistors, Heterojunction Bipolar Transistors (HBTs), have also been developed which are suitable for high power applications at high frequencies and these make possible levels of performance simply not achievable with conventional silicon bipolar transistors. The availability of such high frequency devices from high frequency fabrication processes facilitates the development of MMIC designs for new high volume production [9], [10]. Fig.1.4(a) shows the trends and expectations for both the cut-off frequency f_T (defined as the frequency at which the short-circuit current gain becomes unity) and the maximum frequency of oscillation f_{max} (defined as the frequency at which the unilateral power gain becomes unity) as expected by the International Technology Roadmap for Semiconductors (ITRS) for different transistor technologies [11], [12]. The current technology is in the sub-THz regime but the trends show very progressive scaling towards the multiple THz regime. Recent publications in the field have demonstrated very promising results. For example, in [13], a 650 GHz low-noise amplifier with 30 dB gain is reported in a 30nm InP HEMT process along with a 670 GHz receiver with 15 dB noise figure. Similarly, [14] presents 15 dB gain, 460 GHz amplifiers in a GaAs HEMT process and [15] reports a 630 GHz transmitter with an integrated phased lock loop in a 130nm InP Heterojunction Bipolar Transistor (HBT) process. Of course, GaAs does have disadvantages. The technology is very expensive and has low manufacturing yields, and thus offer limited integration possibilities. Furthermore, the technology is not expected to scale in cost as rapidly as silicon based technologies [16].

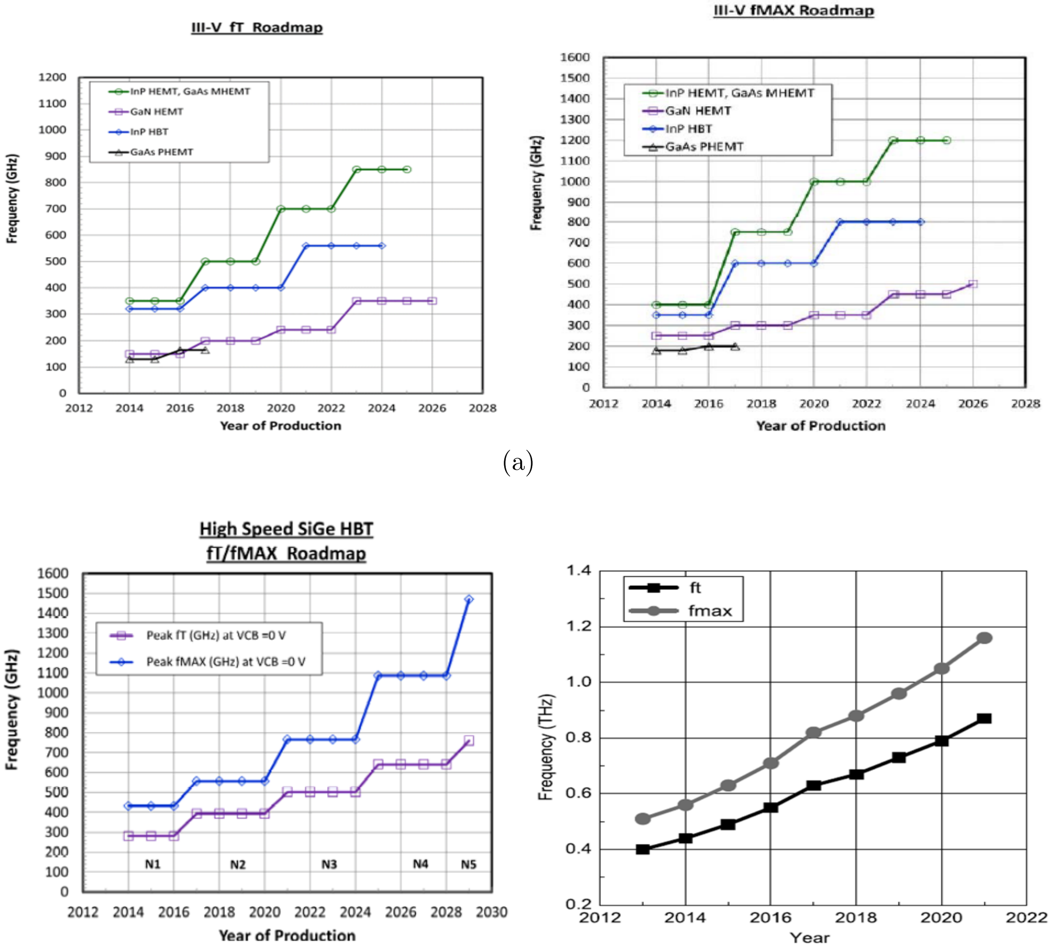

(a)

(b)

(c)

Figure 1.4: Trends and expectations for both f_T and $f_{max}$of transistors in different technologies as specified by the ITRS roadmap [11], [12]. (a) III-V. (b) SiGe. (c) Si NMOS.

Silicon-based technologies (Complementary Metal Oxide Semiconductor (CMOS), Silicon Germanium (SiGe), and Bipolar CMOS (BiCMOS)) have become popular over the last decade, enabling revolutionary growth in consumer electronics and communication systems. SiGe technology offers designers the many performance virtues of SiGe HBTs, i.e., high gain, low noise, good linearity, and good power handling, among others, within a low-cost, highly-integrated, silicon-compatible technology platform [4], [17]. SiGe also provides on-die silicon Complementary Metal–Oxide–Semiconductor (CMOS) multi-level metallization with low-loss transmission lines, and a suite of integrated passive elements, such as antennas [18], for a true system-on-a-chip technology platform. The performance of SiGe technology has improved dramatically in recent years and has been used to develop HBTs with a transistor $f_T > 300$ GHz and $f_{max} > 500$ GHz, respectively [19]. High-performance SiGe-based front-ends for radar and communication systems have been demonstrated at MMW frequencies (e.g., 60 GHz) [20]. First attempts to realize SiGe-based front-ends in the THz band have already been demonstrated at 200 to 300 GHz [21] and even up to 840 GHz [22].

Recently, several CMOS-based transmitting and receiving components have been developed in THz [12], [23]–[25]. Silicon RF technology is relatively inexpensive, and in the case of CMOS, practically 'free'. The burden and major cost to develop silicon CMOS technology was provided by a large digital microprocessor market and analog and RF applications could leverage many of the innovations in the manufacturing of silicon circuits. Fig.1.4(d) shows the ITRS projected roadmap of f_T and f_{max} for NMOS transistors. By the year 2020, the f_{max} of CMOS transistors will be higher than 1 THz. Standard CMOS technology is always considered as the most cost effective solution to combine all digital, analog and MMW system designs. Unfortunately, the transmitting power in a standard CMOS technology is usually limited by the small source drain maximum voltage, while the receiver sensitivity is limited by the poor noise figure. In general, the CMOS technology has the potential to replace the more expensive III-V technology in most blocks in the MMW front-end except for few niche applications such as power amplifiers [16].

While fully integrated transceiver modules have been reported in the literature at sub-THz frequencies, the integration of the antennas with the rest of the radar front-end remains a challenge. High directivity, high efficiency and sufficient bandwidth are all important parameters to compensate for the relatively high propagation loss at sub-THz frequencies. Many novel techniques have been proposed in the literature for integrating the transmit and receive antennas with the front-end. In general, there is a contradiction between the level of integration and the antenna efficiency. In [26], two external horn antennas were used for both the transmitter and receiver as shown in Fig.1.5(a). This scheme offers the lowest level of integration and leads to bulky radar sensors. On the other hand, very high efficiency antennas can be used with well controlled radiation pattern over the complete field of view. Also, mechanical beam steering can be incorporated in this scheme in a straightforward manner. A higher level of integration is demonstrated in [27] and shown in Fig.1.5(b). Here a 16-element phased array SiGe chip (for 77 - 81 GHz automotive applications) with RF beam forming capabilities is attached to a 16-element linear microstrip array on a Rogers RO3003 board. This scheme leads to a more compact overall radar sensor. However, it does not scale well to the sub-THz frequencies because of the extremely high substrate losses in the PCB board leading to poor efficiency designs specially in the power feeding network when large number of antennas is required. To mitigate the effect of the PCB losses, a solution is presented in [28] in which the antenna is integrated together with the SiGe transceiver inside a special package called 'embedded wafer level ball grid array' (eWLB) (Fig.1.5(c)). This scheme allows avoiding any transition of the MMW signal from the package to a PCB board, reducing the signal loss and the cost for the PCB. Due to limited size to implement the antenna, the efficiency is typically not high. Taking the integration one more step leads to the realization of the antenna directly on the chip. This has been demonstrated using patch antennas at 280 GHz in CMOS technology [25] (Fig.1.5(d)), and using bow-tie type antennas for large bandwidth operation [29]. Although this scheme offers the ultimate level of integration, it has the worst radiation efficiency as most of the energy is dissipated in the substrate. Furthermore, the conduction losses is usually high because of the thin

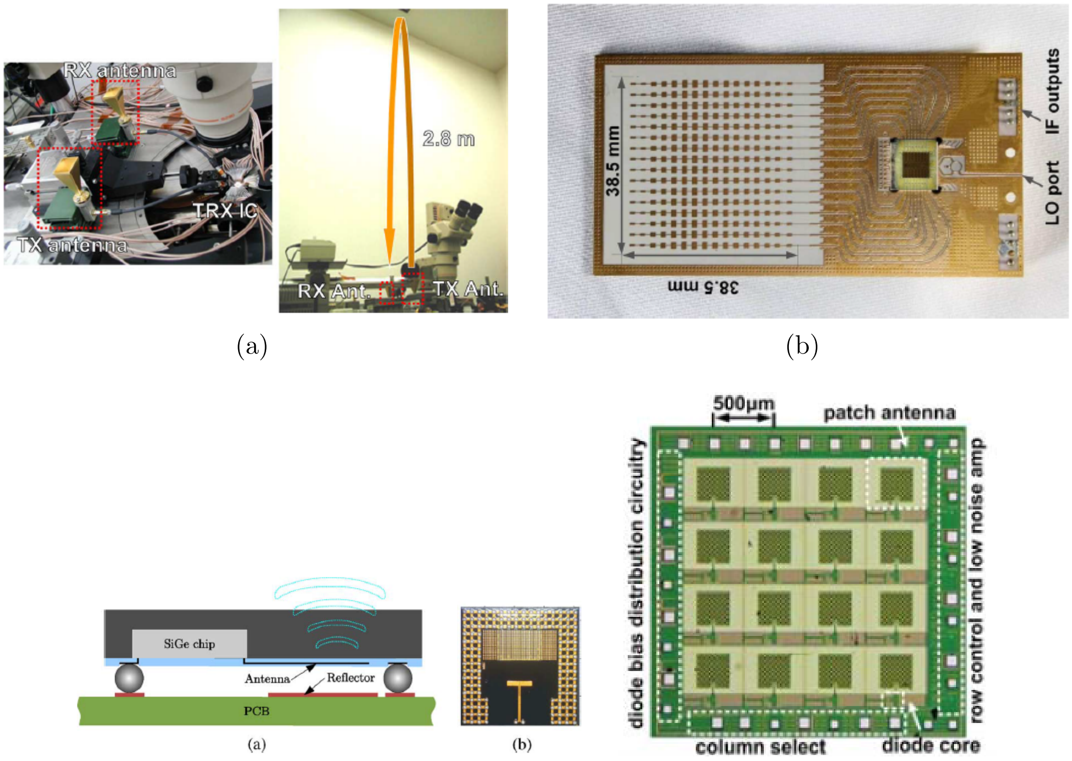

(a) (b) (c) (d)

Figure 1.5: Different schemes for connecting the transciever chip to the antennas. (a) External horn antennas coupled to the fully integrated 77 GHz CMOS Transceiver chips [26]. (b) A 77-81 GHz SiGe chip coupled to 16-element linear microstrip array on Rogers RO3003 substrate [27]. (c) Antenna in package [28]. (d) Antenna on chip [25].

metallization layers available from the process. Adding a thick dielectric layer [30], external lens [31], or external parasitic resonators [32] can help to increase the antenna directivity and reduce the losses.

1.2 Sub-THz Radar Applications

As mentioned before, sub-THz radar systems are charaterized by very high resolution capabilities with small sensor size. These characteristics have made them very attractive for a plethora of applications.

Automotive Radars

According to the Unites States Census Bureau, traffic accidents continue to exceed 10 million accidents per year. These accidents result in at least 30 thousand fatalities per year and many billions of dollars in loss in both human productivity and material. Causes of traffic accidents may be attributed to human error, highway congestion, or poor weather and road conditions. To reduce traffic accidents and physical injury to passengers, development of different driver assistant systems (DAS) to improve safety have been under consideration. These systems can have different functionalities from something as simple as parking aid, to more complicated tasks like adaptive cruise control (ACC) where the vehicle actively accelerates or brakes to maintain a constant distance to the vehicle in front of it, or automatic emergency braking where the car sharply decelerates in case of an obstacle on the road [33]. MMW radars have clear advantages over optical and infrared sensors, in terms of their capability to operate under inclement weather conditions, such as fog, rain, sand storms, and snow. Another attractive feature of MMW radar sensors that makes them suitable for autonomous vehicle control operations is their ability to measure the target's range and speed accurately. In the United States, the Federal Communications Commission (FCC) has allocated two bands for automotive radars. The first band is an ultra wideband (UWB) from 22 to 29 GHz (conventionally called the 24 GHz band). This band is charectrized by a very wide 7 GHz bandwidth (this translates to about 2 cm of range resolution using equation (1.1)) but with very strict emission restrictions in terms of the transmitted power [34]. This band is intended for short range vehicular sensing applications which require very high resolution such as blind spot detection, side and rear impact sensing, and assitive parking. The vision of the automotive industry is to incorporate several of such short range sensors around the vehicle to provide $360^{\underline{o}}$ awareness for the driver [16]. Of course, cost and power consumption are crucial for these sensors which might justify the relatively low frequency of operation. The second frequency band allocated by the FCC is located between 76-77 GHz (conventionally called the 77 GHz band). This band has a smaller bandwidth compared to the 24 GHz band, but enjoys much higher peak transmit power and is intended for long range ($>$ 100m) ACC applications. For such long range operations, a very narrow antenna beam is needed which can be obtained with a resonably sized aperture antenna at this frequency band. A host of sensors providing different functionality envisioned for future cars is shown in Fig.1.6 [16]. Several commercial radar sensors are already available in high-end cars [33].

Stand-off Imaging of Concealed Objects for Security Applications

A prerequisite of any image-based screening system is the ability to form an image in which there exists sufficient contrast between concealed objects and the background medium of the human body that they can be distinguished. This condition requires that the portion

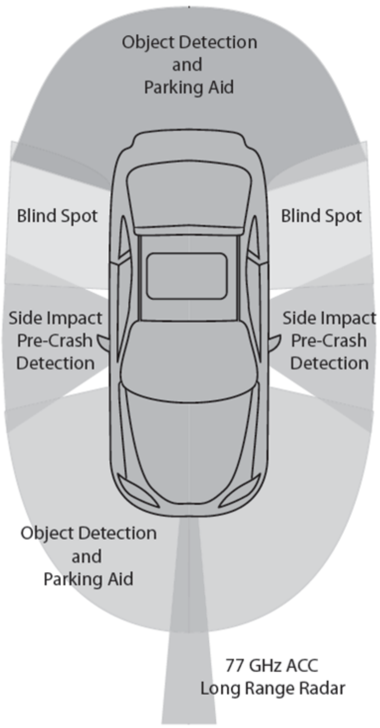

Figure 1.6: Top view of a car and the desired sensors [16].

of the electromagnetic spectrum utilized for image formation is not significantly attenuated by clothing materials, and also that the objects to be resolved have physical properties (reflectance) that are sufficiently different from that of the human body to give a resolvable difference in contrast in the formed image. Also important is that the imaging system has sufficient spatial resolution that the shape of the object can be resolved sufficiently well for a decision on the nature of it, or even permitting an identification to be made allowing, for example, the user to be able to discriminate between a handgun and a mobile phone. The only region of the electromagnetic spectrum where these conditions are easily met is in that of the MMW regime [35]. It has been demonstrated in the literature that sub-THz radiation can pass through typical clothing textiles without high attenuation [36], [37]. Several groups have reported different imaging systems for concealed object detection at varying frequencies. [38]–[41]. Fig.1.7 shows the radar image of a gun replica strapped to a mannequin at 670 GHz where the gun image can be clearly distinguished. It should be mentioned here that real time imaging is usually a big challenge for these systems as beam scanning is usually done using slow quasi-optical techniques.

Other Miscellaneous Applications

Other interesting applications of MMW and Sub-THz radars that have emerged in recent years include infrastructure monitoring [42], robotic indoor navigation and mapping [43], navigation of autonomous aircrafts [44], assivitive landing of aircrafts in optically obsecured environemnts [45], detection of foreign object debris in runways for airport saftey [46], and enhancement of infrared vision in fire fighting operations [47].

Figure 1.7: Imaging of a mannequin with a gun replica strapped to its back at 670 GHz. (a) The mannequin is wrapped in a damp T-shirt and plastic foil to simulate human skin. (b) The gun replica is hidden under a T-shirt. (c) Radar image of the front surface. (d) Radar image of the furthest surface. [38].

1.3 Radar Phenomenology in the Sub-THz Band

The phenomenology of radar return from different natural and man-made targets is essential for many sensing applications concerned beyond detection and ranging. In addition, the ability to model radar scenes is valuable when the performance of radars within complex scenarios is to be determined in a simulation environment. Unfortunately, the literature concerning the radar backscatter behavior of natural terrain at sub-THz frequencies, in general, and near the 240 GHz frequency window, in particular, is rather scarce. Previous efforts included wave attenuation and reflection studies through precipitation [48], [49], radar backscatter measurements of tree canopies and surfaces [50], [51] and snow covers [52]. Nevertheless, these studies were limited in terms of target types, angular ranges, and polarizations.

One of the main advantages of the radar technology is the all-weather working capabilities. Such property needs to be verified at sub-THz frequency range. In some cases, it becomes very difficult or expensive to perform controlled radar experiments as in the case of rain, snow, or dust. For these scenarios, developing a simulation model that accurately describes the propagation of the electromagnetic wave inside the random media with very high speed is extremely valuable. Conventional scattering theories for both surface- and volume-scattering can not be extended to the sub-THz frequency regime in a straight forward manner. The reason for that is most of the underlying assumptions and simplifications are not applicable at sub-THz frequency range. For example, at 240 GHz, the wavelength is about 1.2 mm and the diameter of a single rain droplet can be as high as 3.6 mm which is equivalent to 3 wavelengths. Thus, although the rain droplet appears to be physically small at this frequency range, it is electrically large leading to complex scattering patterns. As a result, something like Rayleigh scattering theory that is conventionally used to describe the scattering behavior of rain droplets at lower frequencies can not be used here and we must resort to the full-wave solution. Another ineresting observation is when considering the scattering from rough surfaces like asphalt and concrete, for example. At the microwave frequencies (say 10 GHz), these surfaces appear electrically smooth and not much scattered energy can be detected in the backscattering direction in the case of oblique incidence. At sub-THz frequencies on the other hand, these surfaces are electrically rough with subsurface aggregate sizes comparable with the wavelength resulting in substantial volume and surface scattering. This can lead to better detection of these types of surfacs for automotive applications, for example. Part of this thesis is dedicated to the development of very efficient scattering models for both surface and volume scattering that is applicable at sub-THz frequencies.

1.4 Dissertation Overview

This dissertation investigates the potential of radar systems operating in the 240 GHz atmospheric window working in typical outdoor environments. There are three main directions of research in the thesis, namely, theoretical, experimental, and fabrication.

In Chapter 2, a semi-numerical, coherent propagation model is presented that can accurately track the electromagnetic wave propagation inside a long, discrete, sparse random media with electrically large scatterers. Such random media can be used to describe media like rain, snow, dust ...etc at sub-THz frequencies. The model is named Statistical S-matrix Approach for Wave Propagation in Spectral Domain, or SSWaP-SD in short, and can be used to track both the magnitude and phase of the electromagnetic wave as it propagates inside the very long random medium. The theory behind the model is presented together with the underlying assumptions. To validate the model, comparison with full-wave simulations combined with Monte-Carlo technique is presented. Based on our understanding of the SSWaP-SD algorithm, an analytical formulation to solve the same problem is presented which we call Analytical SSWaP-SD, or ASSWaP-SD. The presented analytical model takes only few seconds to finish and yield the same statistical results calculated by the full-wave simulations in multiple days. Being a coherent model, it is then extended to to study the degradation in imaging resolution for a Synthetic Aperture Radar (SAR) working in such random media. Finally, a simple algorithm is proposed to reduce the speckle level of the SAR image without sacrificing its resolution.

Chapter 3 and 4 are concerned mainly with the experimental work. First, a free-space, transmission-only, network analyzer based dielectric characterization setup is described in chapter 3. The system works in the range 220 - 325 GHz and is used to measure the dielectric constant of different fabric materials (wool, polyester, jeans ...) in both dry and wet conditions. Such measurements are important in the context of concealed object detection algorithms. Two challenges are faced here as the fabric material does not have a well-defined thickness (it depends on how much you squeeze when you measure the thickness) and its surface is not perfectly smooth. A novel dielectric retrieval algorithm is presented to mitigate these two problems. The proposed setup is slightly adjusted to measure the dielectric constant of human skin through one-port reflection measurements. This is done by simply sticking the tissue under considerations at the end of an open-ended rectangular waveguide. The problem of an open-ended rectangular waveguide radiating in a half dielectric space is numerically solved and the results are used in the retrieval algorithm. In chapter 4, the measurements of the back scattering coefficient from different natural and synthetic rough surfaces at 222 GHz is presented. To this end, a fully polarimetric, network analyzer based, instrumentation radar system working at 222 GHz is built and mounted on genie lift, that is mounted on a flatbed truck to perform outdoor measurements. The polarimetric back scattering coefficient of asphalt, dirt, concrete, as well as different vegetation surfaces is measured at angles of incidence ranging from 25^{o} to 75^{o} from normal. A semi-empirical hybrid model for predicting the total backscattering coefficients of the different rough surfaces considered is presented and validated. In this model, the backscattering coefficient is considered to be the sum of the backscattering coefficients due to surface scattering and volume scattering. The proposed model agrees quiet well with the measured data over the considered range of angles of incidence.

A novel sub-THz phase shifter for beem-steering, leaky-wave antenna applications is presented in Chapter 5. Specifically, a rectangular waveguide based phase shifter is designed to provide a 360^{o} at 240 GHz with minimal insertion loss. In essence, the phase shifter is composed of a TE_{10} rectangular waveguide loaded with a tunable effective perfect magnetic conductor (PMC). By mechanically actuating the PMC surface, the dispersion relation of the resulting TE_{10} mode can be modified and, hence, the phase shifting action can be realized as the electromagnetic wave travels inside the waveguide. The design is optimized through simulation for best insertion loss performance. It is then fabricated using silicon micro-fabrication techniques and measured using a custom built rectangular waveguide probes. The mechanical actuation is achieved through an external piezoelectric actuator. Such phase shifter is intended to be used to realize a high efficiency, electronic beam-scanning leaky wave antenna.

The dissertation concludes with a summary of its contributions and the future directions for this research in Chapter 6.

CHAPTER II

Simulation of Long Distance Wave Propagation in 2D Sparse Random Media: A Statistical S-Matrix Approach in Spectral Domain

2.1 Introduction

In order to build reliable radars or communication systems at sub-THz frequencies, it is important to understand and quantify the phenomenology of wave propagation through typical communication channels such as atmospheric (rain, snow, etc.), foliage, and urban environments. Such environments are statistical in nature and accurate prediction of wave propagation often times entails complex mathematical models. When modeling the scattering from random media, it is common to represent the field as summation of two components, namely, the coherent or the mean field component, and the incoherent or fluctuating component, that is:

$$\overrightarrow{E}\left(\overline{r}\right) = \left\langle \overrightarrow{E}\left(\overline{r}\right) \right\rangle + \widetilde{E}\left(\overline{r}\right) \tag{2.1}$$

where the symbol $\langle ... \rangle$ refers to the ensemble average. Depending on the communication range and the degree of scattering in the medium, the incoherent part may be smaller, comparable, or even larger than the coherent part. Over the past century, many theories have been proposed in order to estimate both the coherent and incoherent part of the wave propagating in random media [1], [53]–[59]. Such theories involve many approximations and are usually applicable under specific conditions pertaining to: frequency of operation, concentration of the scatterers (sparse versus dense), or permittivity fluctuations of the scatterers against the background (strong versus tenuous). For example, at low frequency dielectric mixing formulas, for low volume fractions, can be used to treat the random medium as an effective homogeneous medium for which the mean-field can be calculated. However, this approach cannot predict the fluctuating part of the field. For tenuous random media, approximations based on the perturbation techniques (like the Born approximation) can be usually incorporated to simplify the analysis [53]. Such methods are not appropriate when dealing with strong permittivity fluctuations. The single scattering approximation is usually used for scattering from sparse discrete random media [53]–[55]. For dense random media, where multiple scattering takes place, higher order approximations such as the quasi-crystalline approximation (QCA) and the quasi crystalline approximation with coherent potential (QCA-CP) may be incorporated for estimation of the mean-field [56]. For estimation of the fluctuating fields, methods based on radiative transfer model [53], [56], [57], or single scattering theory [58] can be utilized.

The objective of this chapter is to present a mathematical framework for simulating long distance wave propagation and scattering in a sparse, discrete random medium composed of electrically large scatterers with high dielectric contrast against the background medium, and include multiple scattering among the particles in the random medium. The proposed model is coherent which means that it can be used to track both magnitude and phase of the electromagnetic wave as it propagates inside the random media. The model is used to estimate both the propagation path-loss as a function of distance, as well as the back scattered signal while preserving the phase information. In addition, the model is used to estimate the resolution degradation of a coherent imaging system called synthetic aperture radar (SAR) working in such random media. This model is appropriate for studying wave propagation in precipitation environments. It is noted that at sub-THz frequencies, the size of rain droplets can be comparable or even larger than the wavelength. For example, at 240 GHz, the wavelength is about 1.2 mm and the diameter of a rain droplet can be as high as 3.6 mm which is equivalent to 3 wavelengths. As a result, low or high frequency scattering approximation methods are not applicable. Also the rain medium cannot be treated as a tenuous random medium as the dielectric constant of pure water at 240 GHz is around $5.28 + j5.35$ according to the Debye model [1]. To examine the accuracy of the proposed mathematical frame work against full-wave solutions, we examine the 2D case in this chapter as it has similar physics to the more realistic 3D case, but requires much shorter simulation time.

The volume fraction of a rain medium is typically much lower than 1% [53]. Due to the sparse nature of such medium, the effective field approximation (Foldy's approximation [55]) which relies on single scattering assumption can be used. In this case, the effective complex permittivity of the medium is determined from a dispersion relation derived from a single interaction between the scatterer and the incident field. Foldy's approximation can only give the mean field and it is only accurate up to distances where the magnitude of the mean field is dominant compared to the fluctuating field components. As the wave propagates in the random medium, there is a distance at which the scattered wave in the forward direction, coming from multiple scattering, becomes statistically larger than the mean field. From this point 'knee point' forward, the attenuation rate in the random media changes to a lower value. Physically, this can be attributed to the ability of the medium to redirect some of the scattered energy towards the forward direction through multiple scattering (incoherent contribution). This phenomenon has been observed experimentally for propagation inside forest environments in which the propagation path-loss exhibited what is called “dual-slope” characteristics [60]–[62]. One of the objectives of this chapter is to estimate the distance at which this knee point occurs in a very fast and efficient manner. Such point is important because it can be used to estimate the usable range of coherent radar imaging systems.

This chapter is organized as follows: first, the statistical S-matrix approach for wave propagation in spectral domain (SSWaP-SD) is presented in Section 2.2 along with the underlying assumptions. Then in Section 2.3, the model is validated against Monte Carlo simulations using a full-wave scattering model. Path-loss attenuation curves as well as back scattered power curves are presented in Section 2.4 for a sparse uniformly distributed discrete random medium. Analytical expressions for the path-loss and back scattered power are also presented in the same section and validated against Monte Carlo simulations. The analytical formulation is then extended in Section 2.5 to analyze the resolution degradation of a coherent SAR system working in such random environment. Based on this analytical formulation , a simple method is used to reduce the speckle level of the SAR image without sacrificing its resolution. The material in this chapter can be found in [63]–[66].

2.2 Mathematical Formulation for the Proposed SSWaP-SD Algorithm

In the following discussion, time harmonic analysis with an implicit time dependence of the form ($e^{-j\omega t}$) is assumed. Also, for the 2D problem, only scalar fields ($\psi\left(x\right)$), representing field components (E_y,or H_y) parallel to the axis of the 2D cylindrical particles, are treated.

2.2.1 Basic Theory

The proposed SSWaP-SD model is depicted in Fig.2.1. The basic idea is to divide the discrete random medium into thin slabs with appropriate thickness. The wave interaction within each slab is then represented by an equivalent high dimensional bistatic scattering matrix that relates the incident and reflected plane waves (propagating in different directions) at the input of the slab to the incident and reflected plane waves at the output of the slab. Specifically, using the Fourier transform, the field at the input of the n$^{\text{th}}$ slab can be expressed as a superposition of plane waves propagating along $\overrightarrow{k} = k_x\hat{x} + k_z\hat{z}$ with $k_o^2 = k_x^2 + k_z^2$ (k_0 is the free space wave number). Denoting a_{n-1} as the amplitude spectrum of plane waves propagating in the $+z$ direction, and b_{n-1} as the amplitude spectrum of plane waves propagating in the $-z$ direction, the field at the input of the n$^{\text{th}}$ slab is given by:

$$\psi_{n-1}\left(x\right) \approx \int_{-k_o}^{k_o} a_{n-1}\left(k_x\right) e^{jk_x x} \mathrm{d}k_x + \int_{-k_o}^{k_o} b_{n-1}\left(k_x\right) e^{jk_x x} \mathrm{d}k_x \tag{2.2}$$

In this expression, only the propagating plane wave modes are included (the ones which have real $k_z = \sqrt{k_o^2 - k_x^2}$) as we are assuming the probability of having two particles, one at each slab, in the near-field of each other is negligible. Such approximation is justified by the

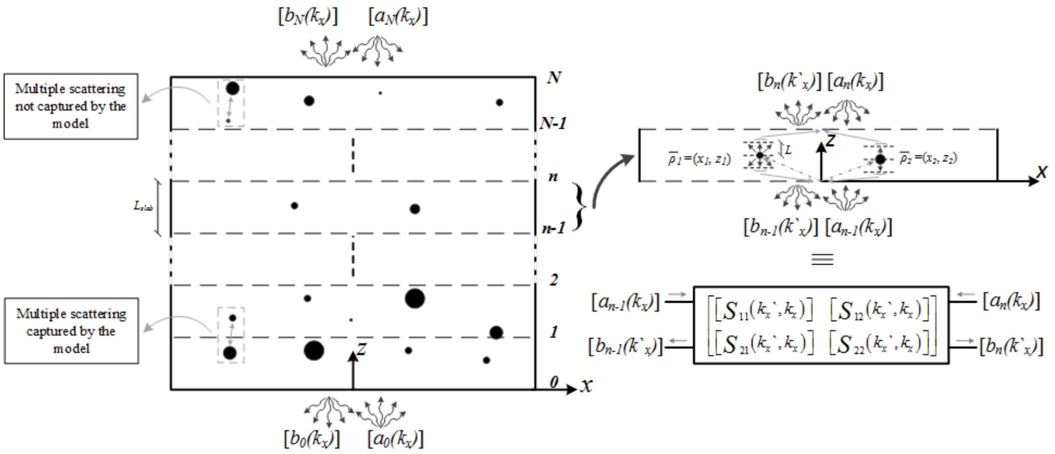

Figure 2.1: Realization of a 2D discrete random medium. Every slab is represented by an equivalent bistatic scattering matrix.

fact that the medium is sparse and the evanescent modes will decay rapidly as they travel away from the scatterer. The field at the output of the n$^{\text{th}}$ slab can also be represented similar to (2.2), and therefore the scattering matrix of the slab can be defined as:

$$\begin{bmatrix} b_{n-1}\left(\grave{k}_x\right) \\ b_n\left(k_x\right) \end{bmatrix} = \begin{bmatrix} S_{11}\left(\grave{k}_x, k_x\right) & S_{12}\left(\grave{k}_x, k_x\right) \\ S_{21}\left(\grave{k}_x, k_x\right) & S_{22}\left(\grave{k}_x, k_x\right) \end{bmatrix} \begin{bmatrix} a_{n-1}\left(k_x\right) \\ a_n\left(k_x\right) \end{bmatrix} \tag{2.3}$$

here $[a_n(k_x)]$ and $\left[b_n\left(\grave{k}_x\right)\right]$ are amplitude vectors of incident and reflected plane waves at the output of the n$^{\text{th}}$ slab for K discrete directions and $\left[S_{ij}\left(\grave{k}_x, k_x\right)\right]$ is a sub-matrix whose individual elements represent the reflected plane wave from the i$^{\text{th}}$ port in the direction $\grave{\theta} = \sin^{-1}\left(\grave{k}_x/k_o\right)$ due to an incident plane wave from the j$^{\text{th}}$ port in the $\theta = \sin^{-1}(k_x/k_o)$ direction. K has to be large enough in order to capture the angular (spectral) variations of the field components. To calculate the spatial variations of the fields, discrete Fourier transform as opposed to continuous Fourier transform (as shown in (2.3)), can be used. Once scattering matrices of the N layers are determined, the overall scattering matrix for the whole random medium can be easily computed.

To derive the scattering matrix of a single slab, we invoke the single scattering approximation [56]. In this approximation, the multiple scattering between the scatterers inside the same slab is neglected. Such approximation is valid for sparse media, but can lead to measurable errors if one of the scatterers happens to be is in the "shadow" region of other scatterer as depicted in the N$^{\text{th}}$ layer in Fig.2.1. This is due to the fact that scattering amplitude is strongest in the forward direction for electrically large scatterers. Note that this problem will not occur if the two scatterers are in consecutive slabs as in the second layer in Fig.2.1. This problem will be further addressed in the next section. Employing the single scattering assumption, the scattering matrix of the thin slab can be easily calculated from the bistatic scattering amplitude of the individual scatterers. As shown in Fig.2.2, the scattered field from a single 2-D scatterer is related to its bistatic scattering amplitude, $T(\theta)$, through [56]:

$$\psi_s(\vec{\rho}) = \frac{e^{jk_o\rho}}{\sqrt{\rho}} T(\theta) \tag{2.4}$$

where $\vec{\rho}$ is the position vector referenced with respect the scatterer's local coordinate. To obtain the equivalent plane wave spectrum at a distance (L) from the scatterer ($z = L$ plane as shown in Fig.2.2), Fourier Transform is applied to (2.4). Using the stationary phase approximation, the spectrum of the plane waves scattered in the z-positive direction is given by:

$$\Psi_s(k_x) = \int_{-\infty}^{+\infty} \frac{e^{jk_o\sqrt{L^2+x^2}}}{\left(L^2+x^2\right)^{1/4}} T\left(\tan^{-1}\left(\frac{x}{L}\right)\right) e^{jk_x x}\mathrm{dx} \approx \sqrt{\frac{2\pi}{k_o}} \frac{e^{j\left(\frac{\pi}{4}+k_o L\cos(\theta_s)\right)}}{\cos(\theta_s)} T(\theta_s) \tag{2.5}$$

where $\theta_s = \sin^{-1}\left({}^{k_x}/_{k_o}\right)$ is the direction of the scattered plane wave. For an incident plane wave with an arbitrary angle θ_i form the z-axis, (2.5) can be modified to take the general

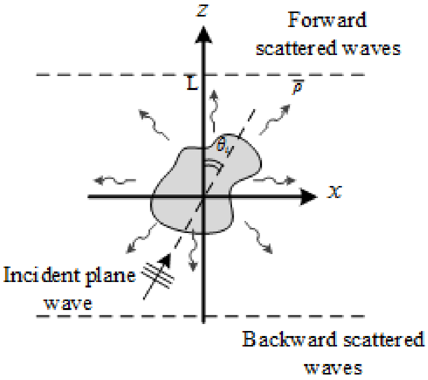

Figure 2.2: Scattering from a single scatterer under plane wave excitation.

form of:

$$\Psi_s\left(\vec{k_s},\vec{k_i}\right) \approx \sqrt{\frac{2\pi}{k_o}}\frac{e^{j\left(\frac{\pi}{4}+k_oL\cos(\theta_s)\right)}}{\cos\left(\theta_s\right)}T\left(\theta_s-\theta_i\right) \tag{2.6}$$

where $\overrightarrow{k_i} = k_x\hat{x} + k_z\hat{z}$ is the incident wave vector, and $\overrightarrow{k_s} = \grave{k}_x\hat{x} + \grave{k}_z\hat{z}$ is the scattered wave vector. Now, the bistatic scattering matrix of the thin slab can be calculated by summing the contribution from individual scatterers. This process is depicted in Fig.2.1 for calculating the sub-matrices $\left[S_{11}\left(\grave{k}_x,k_x\right)\right]$, and $\left[S_{21}\left(\grave{k}_x,k_x\right)\right]$. First, the plane waves at the input of the slab are propagated to the position of each scatterer through multiplication by $(e^{j\vec{k_i}\cdot\vec{\rho_n}})$, where $\vec{\rho_n}$ is the position vector of the n$^{\text{th}}$ scatterer inside the slab. Then, (2.6) is used to obtain the scattered plane wave in the $\vec{k_s}$ direction referred to plane $z = z_n + L$ for S_{21} calculations, and plane $z = z_n - L$ for S_{11} calculations. Finally, the scattered wave is propagated to the slab output for S_{21} calculations, and to the slab input for S_{11} calculations. Mathematically, this can be written as:

$$S_{11}\left(\grave{k}_x,k_x\right) = \sum_{m=1}^{M} e^{j\vec{k_i}\cdot\vec{\rho_m}}\cdot\Psi_s^m\left(\vec{k_s},\vec{k_i}\right)\cdot e^{-j\vec{k_s}\cdot(\vec{\rho_m}-L\hat{z})} \tag{2.7a}$$

$$S_{21}\left(\grave{k}_x, k_x\right) = e^{jk_z L_{slab}} + \sum_{m=1}^{M} e^{j\vec{k_i}\cdot\vec{\rho_m}} \cdot \Psi_s^m\left(\vec{k_s}, \vec{k_i}\right) \cdot e^{j\vec{k_s}\cdot\left(L_{slab}\hat{z}-\left(\vec{\rho_m}+L\hat{z}\right)\right)} \tag{2.7b}$$

where M is the total number of scatterers per slab, and the term $e^{jk_z L_{slab}}$ represents the contribution of the incident field. The elements of $\left[S_{12}\left(\grave{k}_x, k_x\right)\right]$, and $\left[S_{22}\left(\grave{k}_x, k_x\right)\right]$ sub-matrices can be obtained similarly by reversing the excitation of the slab with respect to the previous case.

Once the scattering matrices of the individual slabs are obtained, they can be cascaded together as described in [67]. For two cascaded slabs, $[A]$ and $[B]$, the resulting scattering sub-matrices can be written as:

$$[C_{11}] = [A_{11}] + [A_{12}]\,[B_{11}]\,(I - [A_{22}]\,[B_{11}])^{-1}\,[A_{21}] \tag{2.8a}$$

$$[C_{12}] = [A_{12}]\,[B_{12}] + [A_{12}]\,[B_{11}]\,(I - [A_{22}]\,[B_{11}])^{-1}\,[A_{22}]\,[B_{12}] \tag{2.8b}$$

$$[C_{21}] = [B_{21}]\,(I - [A_{22}]\,[B_{11}])^{-1}\,[A_{21}] \tag{2.8c}$$

$$[C_{22}] = [B_{22}] + [B_{21}]\,(I - [A_{22}]\,[B_{11}])^{-1}\,[A_{22}]\,[B_{12}] \tag{2.8d}$$

At this point it is important to emphasize that this simulation technique is exact with the exception of ignoring multiple scattering within individual slabs. This is adequate for sparse random medium as the probability of multiple scattering within the same slab can be made very small by choosing the slab thickness appropriately. This point will be further discussed in the next section.

2.2.2 Numerical Implementation

In order to implement the previous algorithm, both the spatial and spectral domain variables (x and k_x, respectively) need to be discretized. In addition, the Fourier transform presented in (2.2) needs to be replaced by the discrete Fourier transform (DFT) as mentioned before. Since we are interested in propagating plane wave modes only, the maximum value for k_x to attain is equal to the free space wave number k_o.

In order to avoid aliasing in the spectral domain, according to Nyquist's sampling criteria, the sampling discretization step in the transverse direction (x direction) needs to satisfy the following condition:

$$\Delta x \leq \frac{\lambda}{2} \tag{2.9}$$

An important consequence of the discretization step is that the scattering problem becomes periodic as shown in Fig.2.3(a) and the truncation creates a spurious response. This numerical artifact is well known in Fourier based simulation techniques such as the Fast Fourier Transform Beam Propagation Method (FFT-BPM) commonly used in optics [68]. In order to compare the proposed method with the results of a full-wave simulation, either the field value must be truncated appropriately at the edges of the finite simulation domain, or the periodic 2D Green's function is used in the full-wave simulation. In this study we will truncate the field using a window function that is inspired by the FFT-BPM and described in [69]. The idea is simple in which the transmitted and reflected field from each slab is multiplied by a window function ($w(x)$) that tapers towards zero at the window's edges. The multiplication is performed in the spatial domain which is equivalent to convolution in the spectral domain. Thus, all we need to do is to perform a convolution between each column of the sub-matrices $[S_{11}]$, $[S_{12}]$, $[S_{21}]$, $[S_{22}]$ (without the contribution of the incident

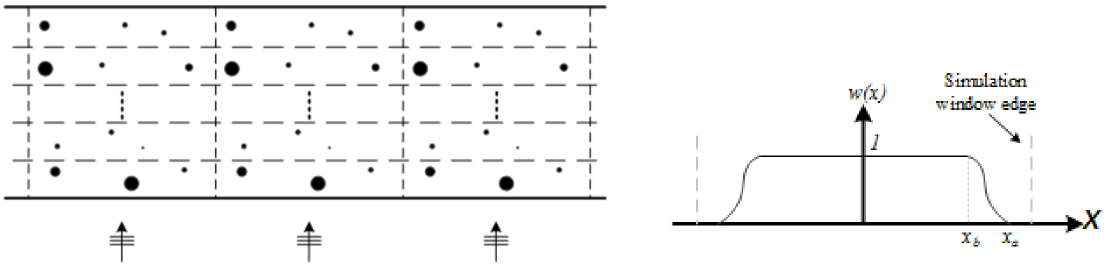

(a) (b)

Figure 2.3: (a) Periodicity effect due to discretization for the proposed simulation technique. (b) Raised cosine window function for mitigating the periodicity effect.

field $e^{jk_z L_{slab}}$ part) and the Fourier transform of the window function ($W(k_x)$) to obtain a new scattering matrix. This new scattering matrix has the window function inherently implemented inside it. A good window function that can be used is the raised cosine window (see Fig.2.3(b)) given by:

$$w(x) = \begin{cases} 0, \quad |x| > x_a \\ {}^1\!/_2 \left[1 + \cos^{\gamma}\left(\pi^{(x-x_a)}/_{(x-x_b)}\right)\right], \quad |x_b| < |x| < |x_a| \\ 0, \quad |x| < x_b \end{cases} \tag{2.10}$$

where x_a, x_b, and γ are parameters that need to be optimized for each window size.

Another consideration is how to choose the thickness of the individual slabs (L_{slab}). Obviously, by increasing the slab thickness, less number of layers will be needed for a fixed propagation distance in the medium. On the other hand, if the layer is chosen thick, the effects of multiple scattering, especially the shadowing, in the individual layer will be worse leading to larger errors. Thus, the thickness needs to be chosen as large as possible while maintain the accuracy of the solution. To achieve this condition, let us examine the scattering geometry shown in Fig.2.1. As mentioned before, a considerable error will occur when one of the scatterers is in the "shadow" region of another scatterer within the same slab (as in layer N). The notion of "shadowing" is discussed here because the scatterers we attempt to deal with are large compared to the wavelength. This error will be small if the two scatters are located in consecutive slabs or even in the same slab when one is not in the shadow region of the other. To elaborate more on this point, Fig.2.4 shows two scenarios: 1) two dielectric cylinders side-by-side, and 2) two cylinders in font of each other. The cylinders are chosen to have the same radius of 3λ and dielectric constant of $\varepsilon_r = 5 + j1$. For both cases, two simulations are performed assuming a TM polarized incident wave (electric field is parallel to the cylinders axis). The first one is a full wave 2D simulation (T-matrix method described in [70]), while the second one is based on the single scattering approximation presented in (2.7). The simulation window size is chosen to be $512\lambda \times 40\lambda$, the number of plane waves considered is 1024, and Δx is chosen to be $\lambda/2$ at 240 GHz. A normalized error for using single scattering approximation is defined as:

$$Error = \frac{\int_{-k_o}^{k_o} \left|\Psi_{s-(full\,wave)}\left(k_x\right) - \Psi_{s-(single\,scattering)}\left(k_x\right)\right| \mathrm{d}k_x}{\int_{-k_o}^{k_o} \left|\Psi_{s-(full\,wave)}\left(k_x\right)\right| \mathrm{d}k_x} \tag{2.11}$$

where $\Psi_{s-(full\,wave)}\left(k_x\right)$ is the spectrum of the scattered part of the solution based on the full-wave simulation evaluated at the plane $z = 40\lambda$, and $\Psi_{s-(single\,scattering)}\left(k_x\right)$ is the spectrum of the scattered part of the solution calculated from (2.7b) (without the incident field) also evaluated at the same plane. It is clear from Fig.2.4 that the single scattering approximation contains large error if a particle is in the shadow of another particle (the line connecting the two particles is parallel to the direction of the mean field). By making sure that the probability of finding one particle in the shadow region of another particle (with respect to the direction of propagation of the mean-field) within the same slab is arbitrary small, the error due to shadowing effect can be minimized. In other words, we want to determine

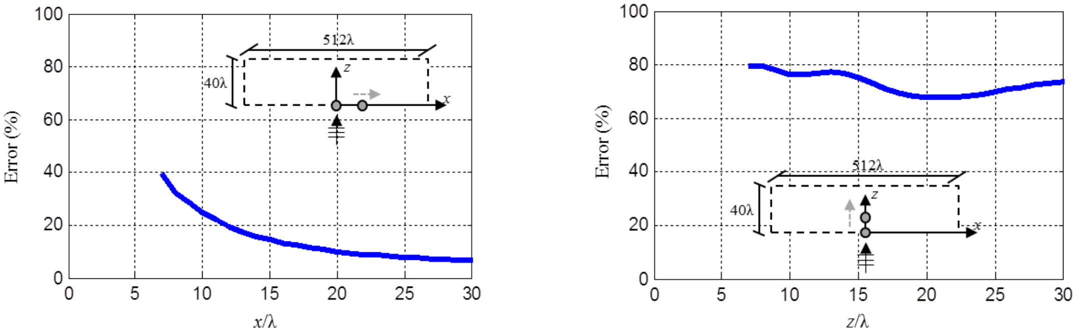

(a) (b)

Figure 2.4: Error, as defined in (2.11), due to shadowing effect between two scatterers. (a) Movement in the horizontal direction. (b) Movement in the vertical direction.

the maximum slab thickness that can be used for a given probability of shadowing. It is expected that this maximum thickness will depend on how the scatterers are distributed within the random medium. This can be determined using the so called "distance-to-the-nearest-neighbor" probability distribution function $f_\nu(r)$ because it is the nearest scatterer that will contribute significantly to shadowing in a sparse random medium. This probability density function describes the probability of finding a scatterer at a distance between r and $r + \Delta r$ from its nearest neighbor. Interestingly, it turns out that this probability function plays an important role in different scientific disciplines like gas dynamics and alloy metallography [71]. As a result, some analytical expressions are derived for random medium with specific particle distribution functions. For example, in a 2D sparse random medium consisting of uniformly distributed impenetrable identical cylinders of radius (ρ_s), this function takes the following form [71]:

$$f_\nu(\rho) = \frac{2\Phi}{\rho_s^2}\rho e^{4\Phi} e^{-\Phi\rho^2/\rho_s^2} \qquad (2\rho_s < \rho < \infty) \tag{2.12}$$

where $\Phi = \pi\rho_s^2 N_s$ is the surface fraction occupied by cylinders, and N_s is the number of cylinders per unit area. For other random media with more complicated particle distribution

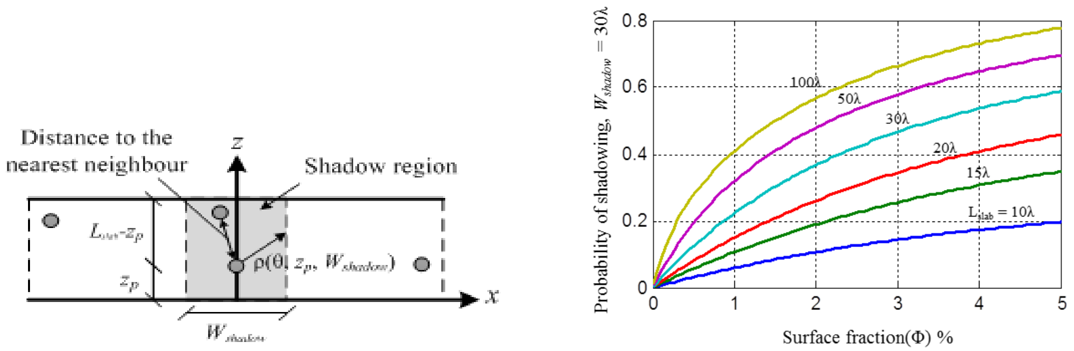

(a) (b)

Figure 2.5: (a) Calculation of the probability of shadowing. (b) Probability of shadowing for different values of L_{slab}.

functions, the distance to nearest neighbor probability distribution function can be determined using Monte Carlo simulation techniques [72]. The probability of shadowing to occur can be calculated by looking at Fig.2.5(a). Basically, for a given scatterer at position (0, z_p), shadowing will occur if the nearest scatterer is located within the shaded area. To calculate such probability, we make use of the cumulative distribution function defined as:

$$F_\nu(\rho) = \int_{-\infty}^{\rho} f_\nu(\rho)\,\mathrm{d}\rho = 1 - e^{4\Phi} e^{-\Phi\rho^2/\rho_s^2} \qquad (2\rho_s < \rho < \infty) \tag{2.13}$$

which represents the probability of finding the nearest neighbor scatterer within a disk of radius (ρ). Furthermore, the probability of finding the nearest scatterer within a circular sector of angle dθ is given by $F_\nu(\rho)\,{}^{\mathrm{d}\theta}/_{2\pi}$. The probability of shadowing can be calculated as:

$$P_{shadowing}(L_{slab}, W_{shadow}, \Phi) = \frac{1}{2\pi L_{slab}} \int_0^{L_{slab}} \int_0^{2\pi} F_\nu(\rho(\theta, z_p, W_{shadow}))\,\mathrm{d}\theta \mathrm{d}z_p \tag{2.14}$$

which can be evaluated numerically. In (2.14), W_{shadow} is a parameter that needs to be estimated based on the mutual scattering properties of two close scatterers. For example, by looking at the two identical cylinders case in Fig.2.4(a), we can estimate W_{shadow} to be around $2 \times 15\lambda$ to have an error that is on the order of 10%. It should be emphasized that (2.14) is based on the approximation that only the nearest neighbor scatterer within the same slab can cause shadowing. This is only true if the medium is sparse and the layer thickness (L_{slab}) is small. A plot of (2.14) is given in Fig.2.5(b) for different values of L_{slab}. The parameters used are $W_{shadow} = 30\lambda$, and $\rho_s = 3\lambda$. It is clear from the figure that the probability of shadowing will increase for larger slab thicknesses.

2.3 Model Verification

In this section the results based on SSWaP-SD algorithm is compared against a full wave simulation [70]. The case considered here is a TM plane wave incident on a uniformly distributed random medium consisting of identical dielectric cylinders with radius $\rho_s = 3\lambda$ and dielectric constant of $\varepsilon_r = 5 + j1$, as before. The reason for choosing this particular case is that the scattering matrix for a single cylinder is analytically available (Mie solution). Also, for identical cylinders, the scattering matrix can be calculated once for all directions as in (2.6), then stored and used for all other cylinders. This can save considerable memory and simulation time.

To generate the random medium, the surface fraction ($\varPhi$) of less than 1% is chosen. By referring to Fig.2.5(b), the value of L_{slab} is chosen to be around 16λ in order to limit the probability of shadowing to less than 10%. The width of the slab (W_{slab}) is given by the multiplication product between the discretization step Δx and the number of discretization points (N_p) which is the same as the number of plane wave modes (from the discrete Fourier transform properties). The value of N_p has a great impact on the simulation time as the scattering matrices in (2.7) scale in a quadratic manner with this value. For our case, Δx is chosen to be $\lambda/2$ and N_p to be 1024 resulting in a slab width of 512λ. The number of slab layers (N_{slab}) determines the total extent of the random medium ($L_t = N_{slab} \times L_{slab}$) in the propagation direction and is chosen to have a value of 30 layers. The frequency used in all of the following simulations is 240 GHz.

The parameters of the window function, introduced in Section 2.2.2, need be optimized for the specified window width (W_{slab}). By trial and error, it is found that values of 230λ, 205λ, and 3 for x_a, x_a, and γ, respectively, can give optimum results. This is demonstrated in Fig.2.6, where a directive source with a $sinc\,(\theta)$ like radiation pattern and inclined by angle of 45^o from the z-axis is used for excitation in free space. It is clear from Fig.2.6(b) that the introduced window function is able to completely suppress the truncation effects without any numerical artifacts. However, it was found that the performance of such window function deteriorates as the angle of incidence approaches 90^o (x-direction). It should be emphasized that this window function limits the usable region of the simulation window to about $2 \times x_b$ which is equivalent, for this case, to about 80% of W_{slab}. Next, the sequential addition method [73] is used to generate a random medium consisting of a total number of cylinders equals to ($N_{cylinder} = {}^{L_t \times 2x_b \times \Phi}/_{\pi\rho_s^2}$) inside a rectangular area of dimensions of ($L_t \times 2x_b$). Once the random medium is generated, it is partitioned into slabs of dimensions ($L_{slab} \times W_{slab}$) and each cylinder is assigned to a particular slab. Thus, the number of cylinders per slab is not necessarily a constant.

Starting from the first slab, the scattering matrix is calculated according to (2.7), and then the columns of each sub-matrix are convolved with the Fourier transform of the raised cosine

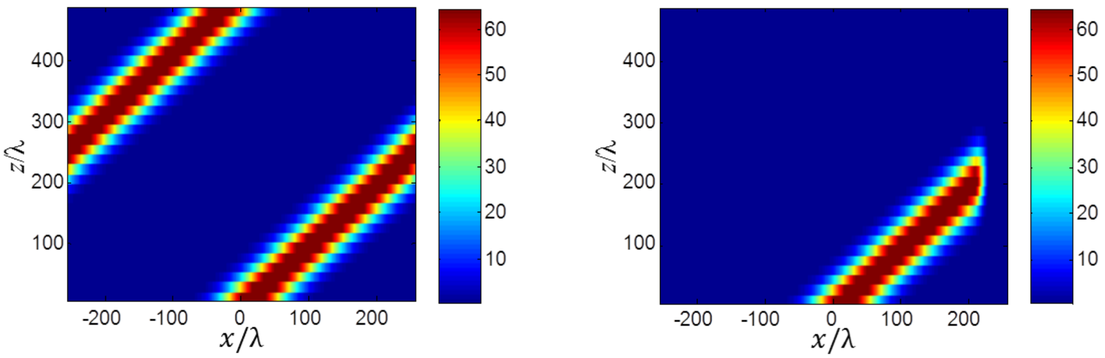

(a)

(b)

Figure 2.6: (a) Periodicity effect due to discretization for the proposed simulation technique. (b) Raised cosine window function for mitigating the periodicity effect.

window function defined in (2.10). Next, the spectrum of the field at the output of first slab is calculated by multiplying $[S_{21}^{1}]$ by the spectrum of the input field which is just a plane wave propagating in the z-direction. The spectrum of the back scattered wave can be calculated similarly by using $[S_{11}^{1}]$ instead. For the second slab, the same procedure is repeated except that the cascaded scattering matrices for the first and second slabs are also calculated using (2.8). The process continues for the rest of the following slabs. Using this procedure, the spectrum of the backward and forward scattered waves from a random medium consisting of n-slabs ($n = 1, 2, 3, \cdots, 30$) can be obtained by multiplying the resultant cascaded sub-matrices $[S_{11}]$ and $[S_{21}]$ of the previous slabs by the spectrum of the incident field.

One hundred Monte Carlo simulations are performed for different surface fraction values (Φ) of 0.5%, 1%, and 1.5%. For each iteration, both full-wave simulation and our simulation algorithm are calculated. The following error terms are defined based on averaged energy spectrum of the scattered wave in both the forward and backward direction for an n-slab medium:

$$Forwared\,Error_n = \frac{\int_{-k_o}^{k_o} \left\langle \left| \Psi^n_{f-(full\,wave)}\left(k_x\right) - \Psi^n_{f-(SSWaP-SD)}\left(k_x\right) \right|^2 \right\rangle \mathrm{d}k_x}{\int_{-k_o}^{k_o} \left\langle \left| \Psi^n_{f-(full\,wave)}\left(k_x\right) \right|^2 \right\rangle \mathrm{d}k_x} \tag{2.15a}$$

$$Backward\,Error_n = \frac{\int_{-k_o}^{k_o} \left\langle \left| \Psi^n_{b-(full\,wave)}\left(k_x\right) - \Psi^n_{b-(SSWaP-SD)}\left(k_x\right) \right|^2 \right\rangle \mathrm{d}k_x}{\int_{-k_o}^{k_o} \left\langle \left| \Psi^n_{b-(full\,wave)}\left(k_x\right) \right|^2 \right\rangle \mathrm{d}k_x} \tag{2.15b}$$

where $\left\langle \left| \Psi^n_{f-(full\,wave)}\left(k_x\right) \right|^2 \right\rangle$ is the energy spectrum of the forward scattered field at the output of the n^{th} slab averaged over all realizations and calculated using full wave simulation. Similarly, $\left\langle \left| \Psi^n_{b-(full\,wave)}\left(k_x\right) \right|^2 \right\rangle$ is the energy spectrum of the backward scattered wave at the input of the first slab for an n-slab medium. The error definitions given by (2.15a) and (2.15b) take into account both the magnitude and phase discrepancies of the scattered wave. Fig.2.7 shows these error terms as a function of the cascaded slab numbers where we can see that the error is bounded below 5% for surface fraction values less than 1%. In Fig.2.8, the averaged energy spectrum for the case of a 30-slab medium with surface fraction of 1% is presented. Good agreements are shown for both the forward and backward directions. It should be emphasized that the error is due to two factors: 1) single scattering assumption within an individual slab, and 2) non-ideal suppression of the truncation effect. The simulation error can also be lowered by reducing the slab thickness according to Fig.2.5(b), at the expense of higher computation time for a fixed propagation distance in the random medium. An approach to further reduce the error is to account for multiple scattering within a slab, but the required computation time is exorbitant. The SSWaP-SD algorithm can also be used with arbitrary source excitation. This is demonstrated in Fig.2.9, where a source with

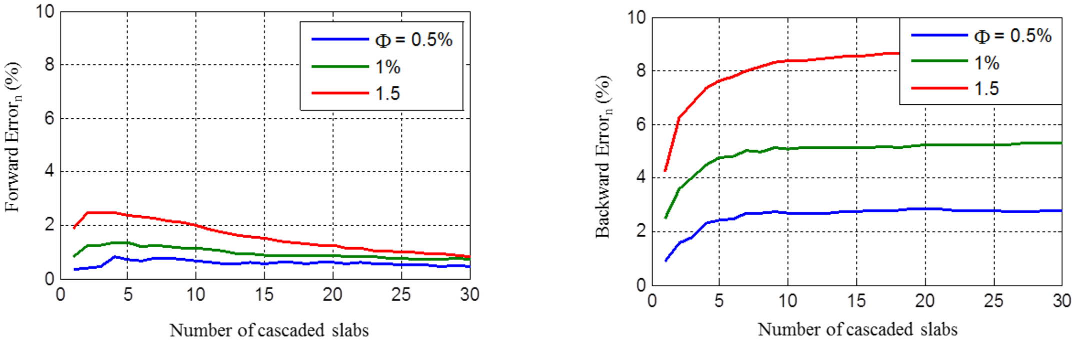

(a) (b)

Figure 2.7: (a) Forward error as defined by (2.15a) and backward error as defined by (2.15b). The number of Monte Carlo iterations is one hundred.

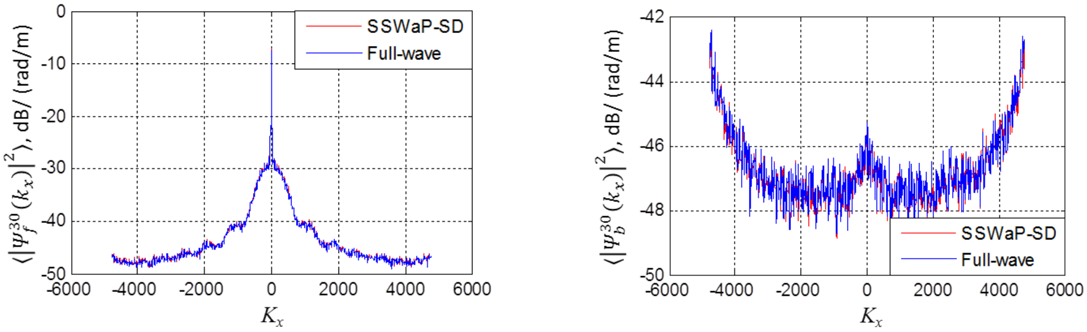

(a) (b)

Figure 2.8: Averaged energy spectrum of the scattered wave for $\mathit{\Phi} = 1\%$. (a) Forward direction. (b) Backward direction.

Gaussian like radiation pattern is used. To realize this image, the output of each slab is first calculated in the spectral domain using our algorithm, then transformed to the spatial domain using the inverse Fourier transform. It is clear from Fig.2.9(b) how the cylindrical scatterers interact with the incident field causing reflection, shadowing, and pattern dispersion effects. The average total power using one hundred Monte Carlo realizations of the medium is plotted in Fig.2.9(c). The figure shows the spatial dispersion and attenuation caused by the particles in the random medium. It is worth mentioning that SSWaP-SD is much faster than the full wave simulation because the simulation time in this case scales linearly with the number of scatters, while for the full wave case, it scales with the square of the number of scatterers. For example, it takes less than 10 minutes to simulate a random medium composed of 100 layers (1600λ) composed of 230 particles on average with surface fraction of 1% on a regular PC. Thus, SSWaP-SD can be used efficiently with Monte Carlo technique to calculate the field fluctuation statistics.

2.4 Long-Distance Path-Loss and Backward Scattered Power Calculations

With confidence in the accuracy of the scattering matrix model for random media, the forward and backward scattered power for a wave propagating in sparse random media over a long propagation distance can be studied. In this case, no raised cosine window function is required. This will result in a periodic medium in the transverse direction which can be considered as a representative of the infinite random medium if the results are independent of the period (W_{slab}). Specifically, we are interested in calculating the power spectral density (PSD) of the scattered wave both in the forward and backward directions. The PSD of a stationary random process can be defined as [74]:

$$S_x\left(f\right) = \lim_{T\to\infty} \frac{1}{2T} \left\langle \left| \int_{-T}^{T} x\left(t\right) e^{-j2\pi f t} \mathrm{dt} \right|^2 \right\rangle \tag{2.16}$$

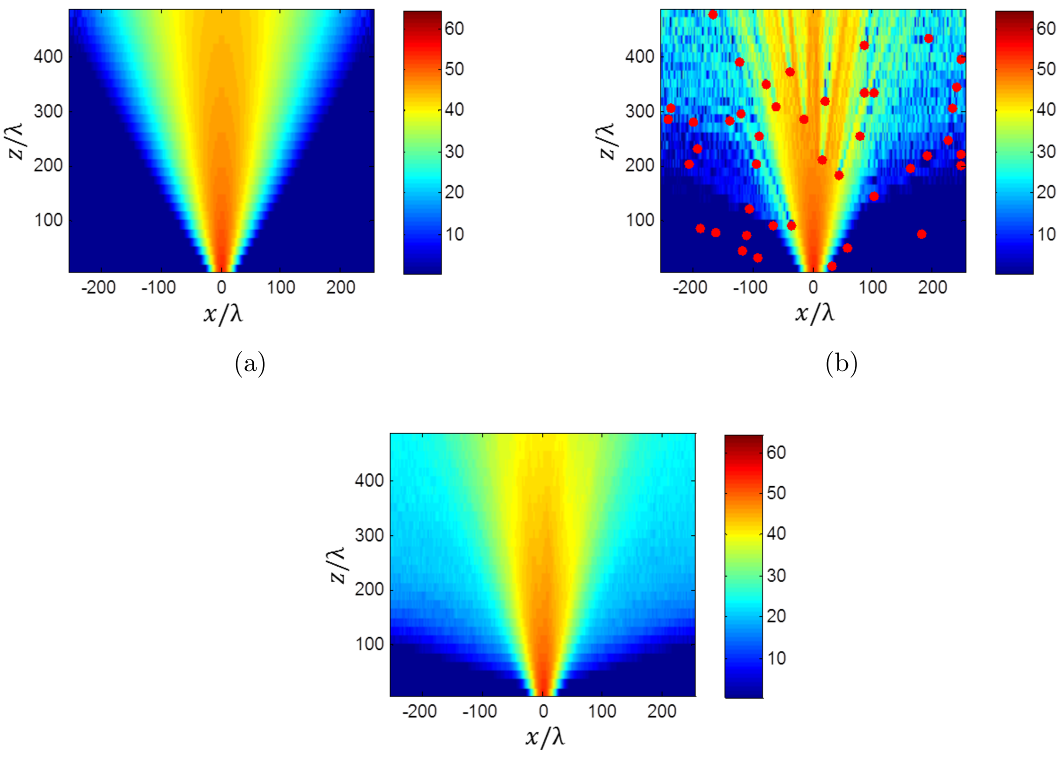

(a)

(b)

(c)

Figure 2.9: Demonstration of the SSWaP-SD algorithm with a source having a Gaussian like radiation pattern. (a) Propagation in free space. (b) Propagation inside a sample medium with surface fraction (Φ) of 0.5% (the cylindrical scatterers are drawn in red color with exaggerated size for better visualization). (c) Propagation in a random medium with surface fraction (Φ) of 0.5% averaged over one hundred Monte Carlo realizations. The three images are drawn in decibel scale.

which is independent of the period (T) for large values of T. Using (2.16) for our case, the PSD of the scattered wave can be evaluated as:

$$S_{\Psi}\left(k_x\right) = \lim_{W_{slab}\to\infty} \frac{1}{W_{slab}} \left\langle \left|\Psi\left(k_x\right)\right|^2 \right\rangle \tag{2.17}$$

Before presenting the numerical results, it is useful to derive an analytical expression for the wave PSD both in the forward and backward directions. The expressions are derived for the case of a statistically invariant, sparse random medium. By statistically invariant we mean that the statistical properties of the medium do not change from one position inside the random medium to the other. An example of such medium is the uniformly distributed discrete random medium with identical scatters, which we will focus on. The results will be compared against Monte Carlo simulation, based on the SSWaP-SD algorithm, for a very long medium consisting of 500 slabs with surface fraction Φ equals to 1% to verify its validity. In the following sections, all power calculated and derived quantities are normalized with respect to the incident power.

2.4.1 Approximate Analytical Expression

In this section analytical expressions for forward and backward scattered power are obtained from SSWaP-SD by invoking two approximations: 1) by enforcing lack of correlation among waves propagating in different directions, and 2) neglecting higher order reflections between individual layers. This model will henceforth be referred to as analytical SSWaP-SD or simply ASSWaP-SD. It can accurately and quickly predict the wave statistics in both forward and backward directions at the expense of losing the phase information. In the following analysis, both the coherent and incoherent component of the scattered wave is treated within the same matrix frame work. Since we are looking for the power spectral density of the scattered wave in the forward and backward directions, the scattering matrices in (2.7) need to be redefined in order to take into account both the coherent and incoherent contributions in a statistical fashion. By referring to Fig.2.10(a), an incident plane wave in direction ($\hat{k}_i$) can only contribute coherently to the scattered wave in the forward direction as well

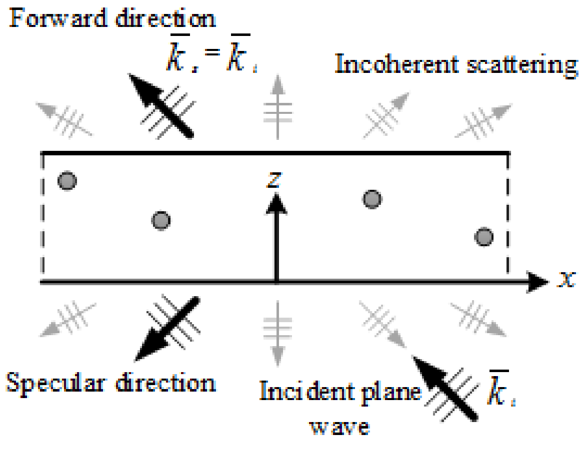

(a) (b)

Figure 2.10: (a) Coherent and incoherent contributions of the scattered wave from one slab in different directions. (b) Approximation of the cascading of multiple slabs.

as the specular direction [56]. In the forward direction, the contribution can be calculated analytically using Foldy's approximation, or equivalently from (2.7b) as:

$$P\left(\hat{k}_s,\hat{k}_i\right)_{\hat{k}_s=\hat{k}_i} = \left| e^{j\overrightarrow{k_i}\cdot L_{slab}\hat{z}} + \frac{N_{cyl/slab}}{W_{slab}}\Psi_s\left(\hat{k}_s,\hat{k}_i\right) e^{j\overrightarrow{k_s}\cdot\left(L_{slab}-L\right)\hat{z}} \right|^2 = \left| 1 + N_s L_{slab}\Psi_s\left(\hat{k}_s,\hat{k}_i\right) e^{-j\overrightarrow{k_s}\cdot L\hat{z}} \right|^2 \tag{2.18}$$

where $N_{cyl/slab}$ is the number of cylinders per slab, and N_s is the number of cylinders per unit area. In the above expression, a normalization by the slab width is carried out to ensure the results are independent of the slab width (W_{slab}). For the specular direction, both coherent and incoherent contribution exist. Following similar steps to [56], the total power of the scattered wave in the specular direction can be written as:

$$P\left(\hat{k}_s,\hat{k}_i\right)_{\hat{k}_s=\hat{k}_{specular}} = \left| \frac{1}{W_{slab}}\Psi_s\left(\hat{k}_s,\hat{k}_i\right) \right|^2 \left\{ N_{cyl/slab} + N_{cyl/slab}\left(N_{cyl/slab}-1\right) sinc^2\left(\frac{k_{iz}L_{slab}}{\pi}\right) \right\} \tag{2.19}$$

where the first term in the brackets represent the incoherent contribution, while the second term represents coherent contribution. For a slab thickness (L_{slab}) that is large compared to the wavelength ($> 10\lambda$) it is safe to neglect the second term as it is much smaller than the incoherent contribution. For other scattering directions, the contribution of the scattered wave will be added *incoherently* and can be written as:

$$P\left(\hat{k_s}, \hat{k_i}\right)_{\hat{k_s}\neq\hat{k_i}} = \sum_{m=1}^{N_{cyl/slab}} \left|\frac{1}{W_{slab}} \Psi_s\left(\hat{k_s}, \hat{k_i}\right)\right|^2 = \frac{N_s L_{slab}}{W_{slab}} \left|\frac{1}{W_{slab}} \Psi_s\left(\hat{k_s}, \hat{k_i}\right)\right|^2 \tag{2.20}$$

Now, for a given scattering direction ($\hat{k_s}$), we need to treat the scattered field from two different incident directions ($\hat{k_{i1}}$, and $\hat{k_{i2}}$). If the contributions from these two incident directions are completely uncorrelated, then their power contributions can be simply added. On the other hand, if there is some degree of correlation, then the treatment becomes more complicated. For this we need to know the "Angular Correlation Function (ACF)" of the random medium [56]. This function describes the correlation of scattered fields in two different directions and is given by:

$$ACF\left(\hat{k_{i1}}, \hat{k_{i2}}, \hat{k_{s1}}, \hat{k_{s2}}\right) = \left\langle \psi_s\left(\hat{k_{s1}}, \hat{k_{i1}}\right) \psi_s^*\left(\hat{k_{s1}}, \hat{k_{i1}}\right)\right\rangle \tag{2.21}$$

This function is directly related to the distribution of scatterers inside the random medium. Translationally invariant random media, exhibit an interesting property known as the "memory effect" [56]. This effect can be written mathematically as:

$$\left\langle \psi_s\left(\hat{k_{s1}}, \hat{k_{i1}}\right) \psi_s^*\left(\hat{k_{s2}}, \hat{k_{i2}}\right)\right\rangle - \left\langle \psi_s\left(\hat{k_{s1}}, \hat{k_{i1}}\right)\right\rangle \left\langle \psi_s^*\left(\hat{k_{s2}}, \hat{k_{i2}}\right)\right\rangle \sim \delta\left(\left(\hat{k_{i1\perp}} - \hat{k_{s1\perp}}\right) - \left(\hat{k_{i2\perp}} - \hat{k_{s2\perp}}\right)\right) \tag{2.22}$$

where δ is the Dirac delta function, and $\hat{k}_{i\perp}$ is the transverse component of the wave vector. Thus, (2.22) has a non-zero value only for directions satisfying the condition:

$$\hat{k}_{i1\perp} - \hat{k}_{s1\perp} = \hat{k}_{i2\perp} - \hat{k}_{s2\perp} \tag{2.23}$$

By applying the above equation to our case for which $\hat{k}_{s1} = \hat{k}_{s2} = \hat{k}_s$, it is easy to show that $\left\langle \psi_s \left(\hat{k}_s, \hat{k}_{i1}\right) \psi_s^* \left(\hat{k}_s, \hat{k}_{i2}\right)\right\rangle \sim \delta \left(\hat{k}_{i1\perp} - \hat{k}_{i2\perp}\right)$, or in other words, there is no correlation between the scatted waves in a given direction $\left(\hat{k}_s\right)$ due to two different incident wave directions $\left(\hat{k}_{i1\perp} \neq \hat{k}_{i2\perp}\right)$. This statement was verified numerically using the full wave simulation applied to a thin slab of the random medium.

To compute the PSD, all we need to do is to replace the previously defined scattering matrices with the new power scattering matrices defined by (2.18), (2.19) and (2.20). Specifically, we have:

$$P_{11}\left(\grave{k}_x, k_x\right) = \frac{N_s L_{slab}}{W_{slab}} \left|\varPsi_s\left(\hat{k}_s, \hat{k}_i\right)\right|^2 \tag{2.24a}$$

$$P_{21}\left(\grave{k}_x, k_x\right) = \begin{cases} \frac{N_s L_{slab}}{W_{slab}} \left|\varPsi_s\left(\hat{k}_s, \hat{k}_i\right)\right|^2, & \hat{k}_s \neq \hat{k}_i \, (non-diagonal\, elements) \\ \left|1 + N_s L_{slab} \varPsi_s\left(\hat{k}_s, \hat{k}_i\right) e^{-j\vec{k}_s \cdot L\hat{z}}\right| & \hat{k}_s = \hat{k}_i \, (diagonal\, elements) \end{cases} \tag{2.24b}$$

For diffuse boundaries, the coherent contribution in the specular direction can be neglected as is in (2.24a). Similarly, we can define the $\left[P_{12}\left(\grave{k}_x, k_x\right)\right]$ and $\left[P_{22}\left(\grave{k}_x, k_x\right)\right]$ sub-matrices.

After obtaining the statistical power scattering matrices for a representative slab, another approximation can be invoked for further simplification. By examining (2.8), it is clear that a considerable computation time is devoted to the calculation of the matrix inversion term

$(I - [A_{22}] [B_{11}])^{-1}$. By making the approximation

$$(I - [A_{22}] [B_{11}])^{-1} \approx I$$

in (2.8), the resulting expressions for cascaded two layers can be simplified to

$$[C_{11}] \approx [A_{11}] + [A_{12}] [B_{11}] [A_{21}] \tag{2.25a}$$

$$[C_{12}] \approx [A_{12}] [B_{12}] \tag{2.25b}$$

$$[C_{21}] \approx [B_{21}] [A_{21}] \tag{2.25c}$$

$$[C_{22}] \approx [B_{22}] + [B_{21}] [A_{22}] [B_{12}] \tag{2.25d}$$

Interestingly, this approximation resembles the small-reflections approximation made when designing multi-section matching networks [75]. Now, since the medium is statistically invariant, we expect all the slabs to have the same power scattering matrices. Thus, for a medium consisting of N_{slab} slabs, the following equations can be written:

$$\begin{aligned}\left[P_{11}^{cascaded}\right] &\approx \left[P_{11}^{slab}\right] + \left[P_{12}^{slab}\right] \left[P_{11}^{slab}\right] \left[P_{21}^{slab}\right] + \left[P_{12}^{slab}\right]^2 \left[P_{11}^{slab}\right] \left[P_{21}^{slab}\right]^2 + \cdots \\ &= \sum_{n=0}^{N_{slab}-1} \left[P_{12}^{slab}\right]^n \left[P_{11}^{slab}\right] \left[P_{21}^{slab}\right]^n \end{aligned} \tag{2.26a}$$

$$\left[P_{21}^{cascaded}\right] \approx \left[P_{21}^{slab}\right]^{N_{slab}} \tag{2.26b}$$

The two equations, (2.26a) and (2.26b), are conceptually depicted in Fig.2.10(b). After calculating (2.26), the forward propagating power through a random medium consisting of

N-slabs can be calculated from:

$$Forward\,Propagatig\,Power \approx W_{slab} P_{21}^{cascaded}\left(\hat{k_s} = \hat{k_i} = k_o\hat{z}\right) \tag{2.27}$$

while the backscattered power can be calculated from

$$Back\,Scattered\,Power \approx W_{slab} P_{11}^{cascaded}\left(\hat{k_s} = -\hat{k_i} = -k_o\hat{z}\right) \tag{2.28}$$

It is interesting to note that there are two ways to implement the matrix multiplication in (2.26). The first way is to cascade one layer at a time, i.e. we will calculate the cascaded power scattering matrices for one layer, two layers, three layers and so on. In this case, the simulation time will be proportional to the propagation distance inside the random medium. The other way is to use the already calculated cascaded power scattering matrices in order to cascade double the number of layers, i.e. we will calculate the cascaded power scattering matrices for one layer, two layers, four layers, eight layers and so on. This will result in a simulation time that is proportional to ($\log_2$) of the propagation distance which is a huge advantage. Also, it is easy to see that the previous analytical expression can be extended to the case of non identical scatterers with arbitrary particle distribution function by replacing the function $\Psi_s\left(\hat{k_s}, \hat{k_i}\right)$ in (2.18), (2.19), and (2.20) by the appropriate ensemble average $\left\langle \Psi_s\left(\hat{k_s}, \hat{k_i}\right)\right\rangle$. Statistical inhomogeneity in the propagation direction can also be easily incorporated in the analytical formulation by cascading layers with different statistical properties.

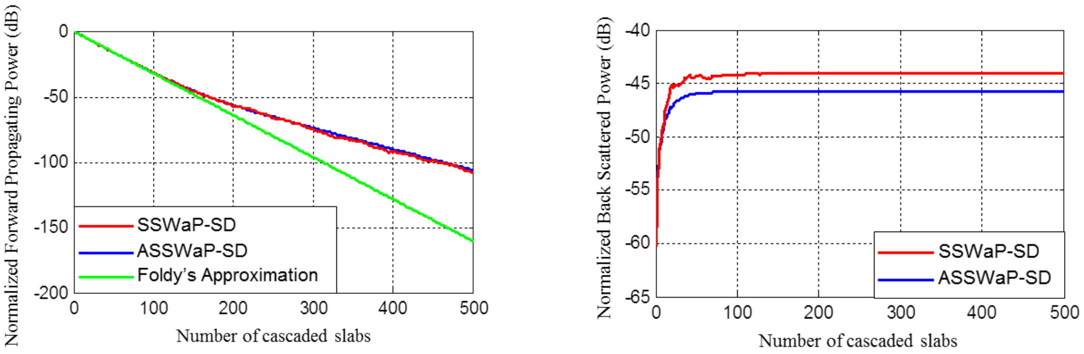

(a)

(b)

Figure 2.11: Normalized forward and backward scattered power through a random medium consisting of 500 slabs with surface fraction of 1%.

2.4.2 Numerical Simulation and Validation

To verify the expressions (2.27) and (2.28), thirty Monte Carlo simulations of a random medium consisting of 500 slabs with surface fraction of 1% are performed (based on the SSWaP-SD algorithm). Other simulation parameters are the same as in Section 2.3. The resulting forward propagating power as well as backscattered power curves are shown in Fig.2.11 and compared with the analytical expressions derived before. A good agreement is observed in the forward direction, while about 2dB discrepancy is observed in the backward direction. Such discrepancy can be attributed to the enhanced backscattering property of the random medium in the backward direction [76], [77]. This is demonstrated in Fig.2.12(a) in which constructive interference occurs between reciprocal wave paths. Fig.2.12(b) shows a comparison of the PSD of the backward scattered wave calculated from the Monte Carlo simulation and from the analytical expression. Good agreement is obtained in general except around the backward direction. This is because the analytical expression does not account for the coherence effect of multiple scattered waves in the backward direction. The dual

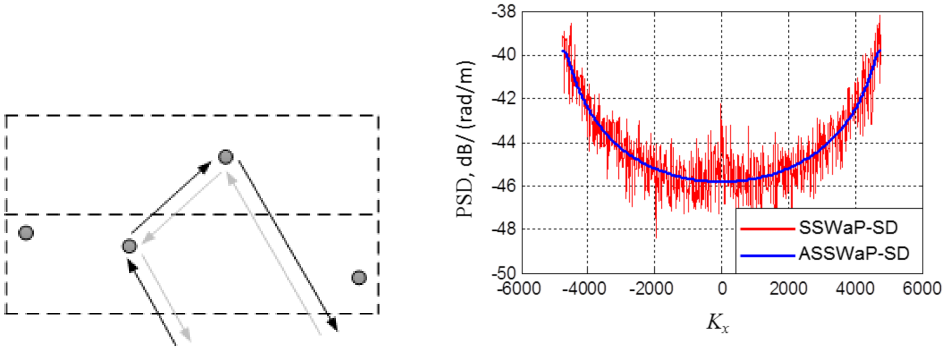

(a) (b)

Figure 2.12: (a) Coherence in the backward direction due to reciprocal wave paths. (b) Power spectral density of the backward scattered wave for a medium composed of 500 slabs and surface fraction of 1%.

slope attenuation curve can be clearly noticed in Fig.2.11(a), where after a critical range of about 3000λ (˜180 slabs) the forward propagating power is mostly dominated by the incoherent component. It is also interesting to note that most of the back scattered power is coming nearly from the first 1200λ (˜80 slabs). The remaining afterward slabs do not contribute to the backscattered power.

It is important to evaluate (2.27), and (2.28) for different slab parameters. This is demonstrated in Fig.2.13 for slab widths (W_{slab}) of 128λ, 256λ, and 512λ. As expected, the results are nearly independent of the value of the slab width. Another verification is shown in Fig.2.14, where the slab width is fixed to 256λ and the slab thickness (L_{slab}) is varied between 4λ, 8λ, and 16λ. The number of slabs in each simulation is adjusted appropriately such that the total length of the medium in the z-direction is constant.

Finally, it is instructive to observe how the attenuation curves and back scattered power curves can vary with the surface fraction (Φ). This is demonstrated in Fig.2.15 where the results are based on the analytical expression. As expected, the "knee point" for the forward

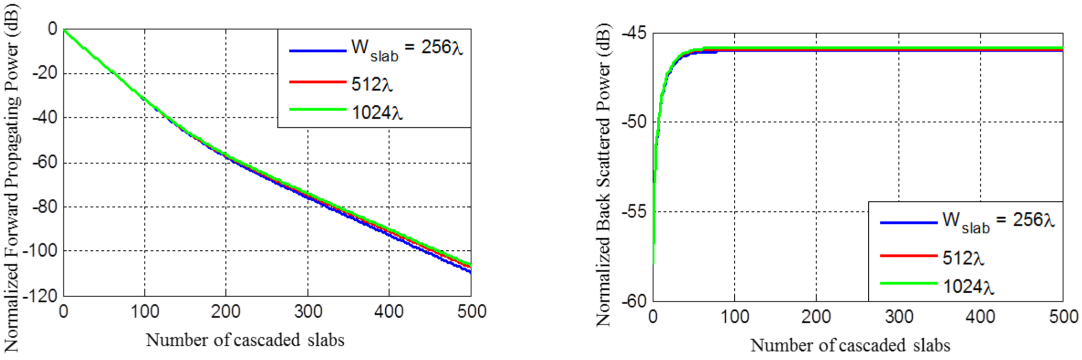

(a) (b)

Figure 2.13: Effect of the slab width on the forward and backward normalized scattered power through a random medium consisting of 500 slabs with surface fraction of 1%. Calculations are based on the analytical expression.

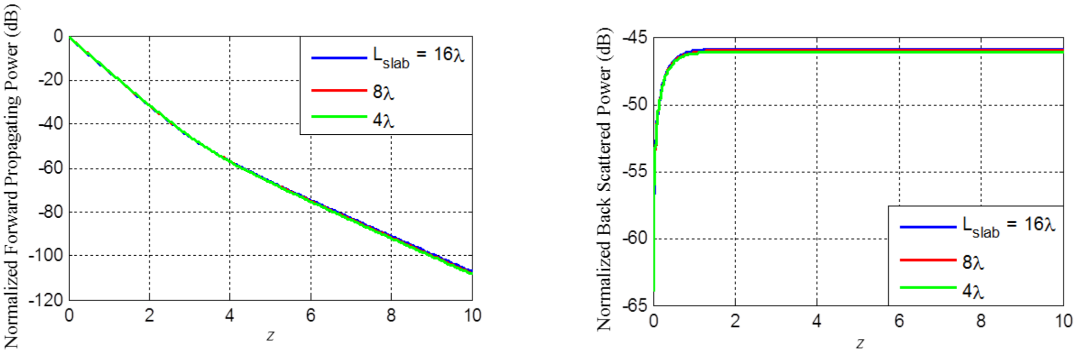

(a) (b)

Figure 2.14: Effect of the slab length on the forward and backward normalized scattered power through a random medium consisting of 500 slabs with surface fraction of 1%. Calculations are based on the analytical expression.

propagating power and the "saturation point" for the backward scattered power are shifted toward lower distances as the surface fraction increases. Another interesting observation is that the saturation level of the back scattered power is nearly constant irrespective of the surface fraction value.

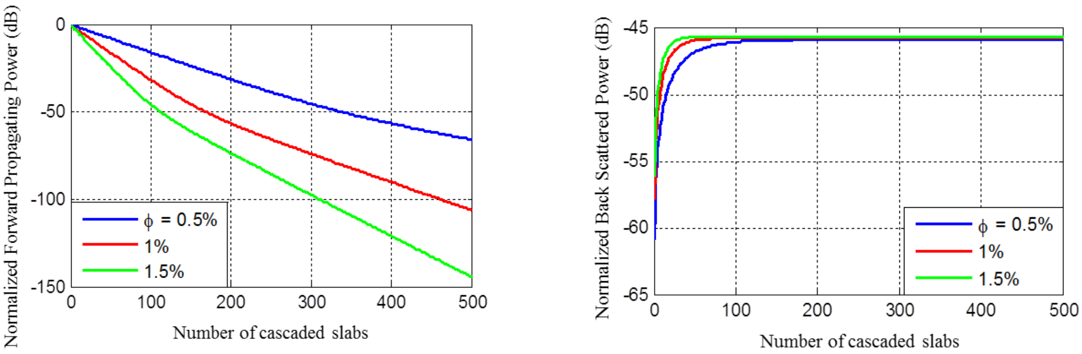

(a) (b)

Figure 2.15: Effect of the surface fraction on the forward and backward normalized scattered power. Calculations are based on the analytical expression.

2.5 Extending the ASSWaP-SD Model to Synthetic Aperture Radar Coherent Imaging Scenarios

Synthetic Aperture Radar system is a high resolution coherent imaging technique in which an effective very large antenna array is constructed by the motion of radar platform and signal-processing means rather than by use of large physical antennas. Basically, the SAR system sends electromagnetic pulses from an antenna mounted on a moving platform to a specific area of interest and records the returned signals. High cross-range resolution is obtained by coherently adding the data collected from the multiple observation points after correcting for the propagation phase, while the range resolution is related to the bandwidth of the system [78]. Due to their high resolution capabilities as well as large coverage area, SAR systems are used in many applications including target detection and identification [79], aircraft traffic control and landing guidance [80], soil moisture retrieval from satellite images [81], and through the wall imaging [82].

In an ideal situation, a focused SAR system can have a cross-range resolution that is independent of range and of the order of $\sim L/2$, where L is the length of the antenna's aperture used [78]. Fine range resolution is achieved using linear chirp pulse compression techniques. In practice, there are a number of factors that can degrade SAR resolution. Some of these factors are related to the system itself such as accuracy in motion compensation, while other factors are related to the propagation environment such as the ionospheric and atmospheric effects (rain, ice, clouds…), or the presence of unwanted objects (clutter) around the target of interest. The study in this section is motivated by the need for better understanding of focusing capabilities of SAR systems through random media at sub-THz frequencies. Specifically, we extend the capabilities of the ASSWaP-SD technique to calculate certain correlation functions that measure the signal coherence due to different source locations, or same source location with different operating frequencies as the electromagnetic wave propagates through the random medium. These correlation functions are directly related to the cross-range and range resolution of the SAR system as will be shown later. Based on the derived correlation functions, a simple method is proposed to reduce the speckle level of the SAR image without sacrificing the resolution.

For the case of a general incident field that is more complicated than just a single plane wave (as in the case of the previous sections), extra care needs to be taken as the problem does not become translational invariant anymore with respect to the source (the medium is still translational invariant but the excitation is not). Consider, for example, a transmitter antenna having the following far field equation:

$$\psi_{Tx}\left(\vec{\rho}\right) = \frac{e^{jk_o\rho}}{\sqrt{\rho}} T_{src}\left(\theta\right) \tag{2.29}$$

where $T_{src}\left(\theta\right)$ is the angular radiation pattern of the source. To obtain the equivalent plane wave spectrum of the radiation pattern, Fourier Transform is applied to (2.29). Using the stationary phase approximation, we have:

$$\Psi_{Gaussian}\left(k_x\right) \approx \sqrt{\frac{2\pi}{k_o}}\frac{e^{j\left(\frac{\pi}{4}+k_oL_{source}\cos(\theta_k)\right)}}{\cos\left(\theta_k\right)}T_{src}\left(\theta_k\right) \tag{2.30}$$

where $\theta_k = \sin^{-1}\left(k_x/k_o\right)$, and L_{source} is the reference z-plane to which the spectrum is referred to. It can be easily seen from (2.30) that there is a coherent phase relation between different plane waves going in different directions. Thus, the approximation used in the previous section (namely, the lack of correlation between plane waves propagating in different directions) is not valid anymore, and we need to keep track of the coherence relation between these plane waves as they propagate inside the random medium from one slab to the next. In this manner, the field statistics at any arbitrary position can be obtained from the superposition of individual plane waves. This was not important for the original ASSWaP-SD as the incident field was just a single plane wave. However, this is not the case here as the excitation is the radiation pattern of the source antenna.

The simulation environment adapted for this study is shown in Fig.2.16. The SAR system is assumed to operate in the strip-map mode in which the radar antenna radiates in a fixed direction pointing to the side of the moving platform (the platform moves in steps of $h = \lambda/2$ from $-a$ to $+a$). Similar to the previous sections, the random medium is composed of uniformly distributed, identical, impenetrable, dielectric cylinders with radii $r_s = 3\lambda$ and dielectric constant of $\epsilon_r = 5+j1$. The radiation pattern of the source antenna is modeled with an angular Gaussian function having the following spatial and spectral domain representations:

$$\psi_{Gaussian}\left(\vec{\rho}\right) = \frac{e^{jk_o\rho}}{\sqrt{\rho}}e^{-\left(\frac{\theta}{\sqrt{2}\sigma}\right)^2} \tag{2.31a}$$

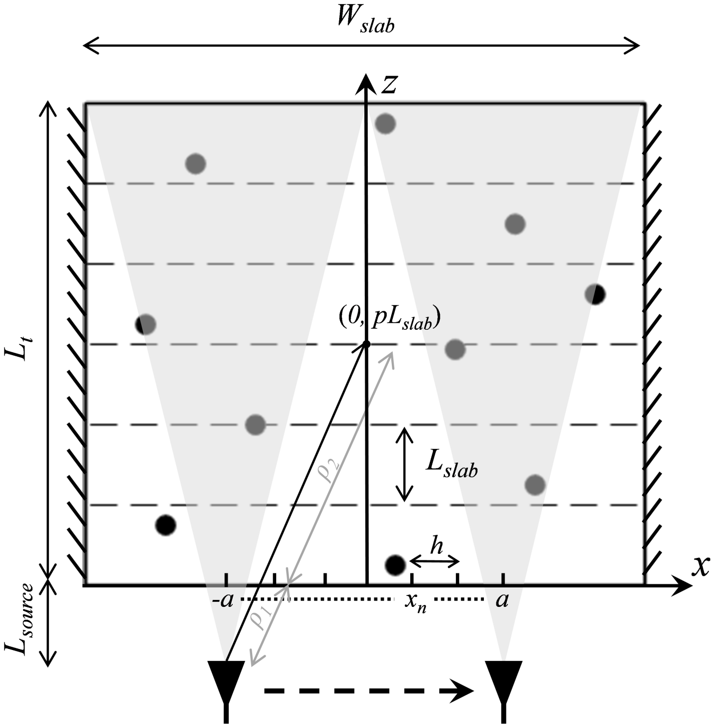

Figure 2.16: 2D SAR system working in strip-map mode in the presence of sparse random medium.

$$\Psi_{Gaussian}(k_x) \approx \sqrt{\frac{2\pi}{k_o}} \frac{e^{j\left(\frac{\pi}{4}+k_o L_{source}\cos(\theta_k)\right)}}{\cos(\theta_k)} e^{-\left(\frac{\theta_k}{\sqrt{2}\sigma}\right)^2} \tag{2.31b}$$

here σ is a parameter proportional to the source beamwidth and its value is adjusted based on the parameters L_{source} and W_{slab} so that the radiation pattern is contained within the simulation window. The aperture length of the source antenna is inversely proportional to σ. As mentioned before, cross-range resolution is related to the radar's aperture antenna length and, consequently, the distance traveled by the radar in the x-direction. Optimum resolution can be achieved if there is no clutter (cylinders in our case) between the transmitting antenna as it moves, and the target under consideration. In addition, the target should not decorrelate as a function of the looking angle. In this case, the field reflected from the target at each source position is nearly the same except for a phase factor that is compensated for when forming the SAR image. In the presence of clutter, and due to the multiple reflections, two main effects can be identified: 1) the wave reaching the target can be highly distorted, and 2) the received field by each antenna is not just due to the target, but also due to the clutter present. Both of these factors will have a negative impact on the resolution of the SAR system depending on the characteristics of the clutter itself. In what follows, we will define a correlation function that measures the degree of coherency of the electromagnetic wave at a specific range position inside the random media due to different transmitter positions. It turns out that this function has a direct impact on the 'effective' aperture length of the SAR system. If this function is very narrow, then only a few number of transmitter locations close to each other can coherently focus on a given target leading to poor cross-range resolution. On the other hand, if this function is very wide, then all of the transmitter locations will contribute to the SAR image leading to the theoretical SAR resolution. In a similar manner, we will define a correlation function that measures the degree of coherency of the wave at a specific range position due to a single transmitter position operating at different frequencies. This function will determine the range resolution of the SAR system.

2.5.1 Cross-Range Resolution

For the cross-range scenario, as shown in Fig.2.16, the source antenna locations are given by the sequence $x_n \in [-a, -a + \lambda/2, \cdots, +a]$. The distance $(2a)$ is chosen to be half of the width of the simulation domain (W_{slab}), while the source radiation pattern parameters(σ) is adjusted such that the wave $(\psi_{x_n}(x, z))$ is small at $(x = \pm W_{slab}/2, z = L_t)$ when the source is located at $(x_n = \pm a)$, respectively. For each source position $(x_n, -L_{source})$, the field value at the center of the output of the p^{th} slab (i.e. $\psi_{x_n}(x = 0, z = pL_{slab})$) is first calculated. To achieve cross-range focusing, propagation phase compensation must be carried using:

$$\tau\left(x_n, pL_{slab}\right) = \psi_{x_n}\left(0, pL_{slab}\right) e^{-j\left[k_o\rho_1(x_n)+k_{eff}\rho_2(x_n)\right]} \tag{2.32}$$

where k_{eff} is the effective wavenumber of the random medium calculated using Foldy's approximation [55], ρ_1 and ρ_2 are as defined in Fig.2.16. This function represents the phase compensated wave value at position $(0, pL_{slab})$ due to a source located at $(x_n, -L_{source})$. After calculating (2.32) at the output of a certain p-slab for all source locations, the following normalized correlation function is defined:

$$R_{\tau\tau}\left(n, p\right) = \left\langle \frac{\frac{1}{N-|n|}\sum_m \tau\left(x_m, pL_{slab}\right)\tau^*\left(x_{m-n}, pL_{slab}\right)}{\frac{1}{N}\sum_m \left|\tau\left(x_m, pL_{slab}\right)\right|^2} \right\rangle \tag{2.33}$$

where (N) is the number of transmitter locations. In the previous expression, normalization by $(N-|n|)$ is introduced to have an unbiased estimation of the correlation function since we have a finite length sequence. Equation (2.33) will be used as a measure to quantify the degree of coherency of the electromagnetic wave at a certain range inside the random media due to different source positions. For the case of free space propagation and if we neglect the source radiation pattern effect together with the propagation effect ($1/\sqrt{\rho}$ effect), then (2.32) should be equal to $1\angle 0$ for any value of (p) and (n), while (2.33) should be equal to a constant of one. If the radiation pattern and propagation effects are taken into consideration, then the correlation function (2.33) maintains its maximum value at $n = 0$, and decays for $|n| > 0$. In the presence of clutter, this function is expected to decay faster.

To derive an analytical expression for (2.33), we basically need to evaluate terms of the form $\left\langle\tau\left(x_n, pL_{slab}\right)\tau^*\left(x_m, pL_{slab}\right)\right\rangle$ for different transmitter locations (x_n and x_m). From the definition of the inverse discrete Fourier transform, we can write:

$$\tau\left(x_n, pL_{slab}\right) = \frac{e^{-j\left[k_o\rho_1(x_n)+k_{eff}\rho_2(x_n)\right]}}{K} \sum_{\grave{k}_x=-k_o}^{+k_o} b_{p,x_n}\left(\grave{k}_x\right) \tag{2.34}$$

where K is the number of plane wave modes considered in the spectral decomposition, and $b_{p,x_n}\left(k_x\right)$ is amplitude vector at the output of the p^{th} slab due to a transmitter location x_n. Consequently, we can write:

$$\begin{aligned}\left\langle \tau\left(x_n, pL_{slab}\right)\tau^*\left(x_m, pL_{slab}\right)\right\rangle &= \frac{e^{-j\left[k_o(\rho_1(x_n)-\rho_1(x_m))+k_{eff}(\rho_2(x_n)-\rho_2(x_m))\right]}}{K^2}\cdot \\ &\sum_{\grave{k}_{1x}=-k_o}^{+k_o}\ \sum_{\grave{k}_{2x}=-k_o}^{+k_o} \left\langle b_{p,x_n}\left(\grave{k}_{1x}\right) b^*_{p,x_m}\left(\grave{k}_{2x}\right)\right\rangle\end{aligned} \tag{2.35}$$

and now the problem reduces to evaluating terms of the from $\left\langle b_{p,x_n}\left(\grave{k}_{1x}\right) b^*_{p,x_m}\left(\grave{k}_{2x}\right)\right\rangle$ which can be done using a variant of ASSWaP-SD.

Consider, as shown in Fig.2.16, an arbitrary slab 'p' inside the random medium with the source antenna at x_n. The amplitude vector of the incident plane wave to such a slab will be referred to as $\left[a_{p-1,x_n}\left(k_x\right)\right]$. Using (2.3) and (2.7) with $L=0$, we can write:

$$\begin{aligned} b_{p,x_n}\left(\grave{k}_x\right) &= \sum_{k_x=-k_o}^{+k_o} S_{21}\left(\grave{k}_x, k_x\right) a_{p-1,x_n}\left(k_x\right) \\ &= e^{j\grave{k}_z L_{slab}}\Big\{ \sum_{k_x=-k_o, k_x\neq\grave{k}_x}^{+k_o} a_{p-1,x_n}\left(k_x\right) \sum_{m=1}^{M} \Psi_s\left(\vec{k_s}, \vec{k_i}\right) e^{j\left(\vec{k_i}-\vec{k_s}\right)\cdot\vec{\rho_m}} \\ &+ a_{p-1,x_n}\left(\grave{k}_x\right)\left(M\Psi_s\left(\vec{k_s}, \vec{k_s}\right)+1\right)\Big\} \end{aligned} \tag{2.36}$$

which has an ensemble average of:

$$\left\langle b_{p,x_n}\left(\grave{k}_x\right)\right\rangle = e^{j\grave{k}_z L_{slab}} \cdot \left\langle a_{p-1,x_n}\left(\grave{k}_x\right)\right\rangle \cdot \left(M\Psi_s\left(\vec{k_s}, \vec{k_s}\right) + 1\right) \tag{2.37}$$

since $\left\langle e^{j\left(\vec{k_i}-\vec{k_s}\right)\cdot\vec{\rho_m}}\right\rangle$ is equal to zero for all $k_x \neq \grave{k}_x$ [73]. For two source locations, it is straight forward to show:

$$\begin{aligned}\left\langle b_{p,x_n}\left(\grave{k}_{1x}\right) b^*_{p,x_m}\left(\grave{k}_{2x}\right)\right\rangle - \left\langle b_{p,x_n}\left(\grave{k}_{1x}\right)\right\rangle \left\langle b^*_{p,x_m}\left(\grave{k}_{2x}\right)\right\rangle &= e^{j\left(\grave{k}_{1z}-\grave{k}_{2z}\right)L_{slab}} \\ \cdot \sum_{k_{1x}=-k_o, k_{1x}\neq\grave{k}_{1x}}^{+k_o} \sum_{k_{2x}=-k_o, k_{2x}\neq\grave{k}_{2x}}^{+k_o} \left\langle a_{p-1,x_n}\left(k_{1x}\right) a^*_{p-1,x_m}\left(k_{2x}\right)\right\rangle \cdot \Psi_s\left(\vec{k_{1s}}, \vec{k_{1i}}\right) \Psi^*_s\left(\vec{k_{2s}}, \vec{k_{2i}}\right) \\ \cdot \left\langle \sum_{m=1}^{M}\sum_{n=1}^{M} e^{j\left(\vec{k_{1i}}-\vec{k_{1s}}\right)\cdot\vec{\rho_m}} e^{-j\left(\vec{k_{2i}}-\vec{k_{2s}}\right)\cdot\vec{\rho_n}}\right\rangle \end{aligned} \tag{2.38}$$

At first glance, (2.38) seems to be very difficult to evaluate as it involves four summations. However, by exploiting the memory effect property of translational invariant random media, (2.38) can be significantly simplified. The last term of (2.38) can be written as:

$$\begin{aligned}\left\langle \sum_{m=1}^{M}\sum_{n=1}^{M} e^{j\left(\vec{k_{1i}}-\vec{k_{1s}}\right)\cdot\vec{\rho_m}} e^{-j\left(\vec{k_{2i}}-\vec{k_{2s}}\right)\cdot\vec{\rho_n}}\right\rangle &= \left\langle \sum_{m=1}^{M} e^{j\left(\vec{k_{1i}}-\vec{k_{1s}}-\vec{k_{2i}}+\vec{k_{2s}}\right)\cdot\vec{\rho_m}}\right\rangle \\ &+ \sum_{m=1}^{M}\sum_{n=1, n\neq m}^{M} e^{j\left(\vec{k_{1i}}-\vec{k_{1s}}\right)\cdot\vec{\rho_m}} e^{-j\left(\vec{k_{2i}}-\vec{k_{2s}}\right)\cdot\vec{\rho_n}}\end{aligned} \tag{2.39}$$

The second term of (2.39) is a function of the pair distribution function of the random medium which describes the distance between pairs of particles contained inside the random medium. For the case of a random medium composed of identical impenetrable cylinders or spheres, this function is known as Percus-Yevick distribution function [73]. For the cases considered here, the position of one cylinder inside the random medium is assumed to be independent of all other cylinders. Such assumption is valid for sparse media (surface fraction values around 1%). As a result, the second term in (2.39) can be shown to be proportional to $\sim \delta\left(k_{1x} - \grave{k}_{1x}\right)\delta\left(k_{2x} - \grave{k}_{2x}\right)$. Such directions are excluded from the sum in (2.38) and, hence, the second term in (2.39) does not contribute to the sum in (2.38). On the other hand, the first term in (2.39) can be evaluated to be:

$$\left\langle \sum_{m=1}^{M} e^{j\left(\vec{k_{1i}} - \vec{k_{1s}} - \vec{k_{2i}} + \vec{k_{2s}}\right)\cdot\vec{\rho_m}} \right\rangle = M e^{j\frac{q_z L_{slab}}{2}} \operatorname{sinc}\left(\frac{q_z L_{slab}}{2\pi}\right)\delta\left(q_x\right) \tag{2.40}$$

where $\vec{q} = \vec{k_{1i}} - \vec{k_{1s}} - \vec{k_{2i}} + \vec{k_{2s}}$. Equation (2.40) is the mathematical statement of the memory effect for translational invariant random medium. It basically says that the angular correlation function for a translational invariant random medium is non-zero only in directions satisfying the general phase matching condition [73]:

$$q_x = 0, \quad or \quad \hat{k_{1i\perp}} - \hat{k_{1s\perp}} = \hat{k_{2i\perp}} - \hat{k_{2s\perp}} \tag{2.41}$$

By substituting (2.39) and (2.40) into (2.38), a simplified explicit equation can be obtained:

$$\begin{gathered}\left\langle b_{p,x_n}\left(\grave{k}_{1x}\right) b^*_{p,x_m}\left(\grave{k}_{2x}\right)\right\rangle = e^{j\left(\grave{k}_{1z} - \grave{k}_{2z}\right)L_{slab}} \\ \cdot\left\{\left\langle\left(M\Psi_s\left(\vec{k_{1s}},\vec{k_{1s}}\right)+1\right)\left(M\Psi_s^*\left(\vec{k_{2s}},\vec{k_{2s}}\right)+1\right)\right\rangle\left\langle a_{p-1,x_n}\left(\grave{k}_{1x}\right)a^*_{p-1,x_m}\left(\grave{k}_{2x}\right)\right\rangle\right. \\ \left.+\sum_{k_{1x}=-k_o,k_{1x}\neq\grave{k}_{1x}}^{+k_o}\sum_{k_{2x}=-k_o,k_{2x}\neq\grave{k}_{2x}}^{+k_o}\left\langle a_{p-1,x_n}(k_{1x})a^*_{p-1,x_m}(k_{2x})\right\rangle\cdot\Psi_s\left(\vec{k_{1s}},\vec{k_{1i}}\right)\Psi_s^*\left(\vec{k_{2s}},\vec{k_{2i}}\right)Me^{j\frac{q_z L_{slab}}{2}}\operatorname{sinc}\left(\frac{q_z L_{slab}}{2\pi}\right)\delta(q_x)\right\}\end{gathered} \tag{2.42}$$

The double summation term in (2.42) is actually a single summation due to the presence of $\delta\left(q_x\right)$. To efficiently evaluate (2.42) for certain $\vec{k_{1s}} = \grave{k}_{1x}\hat{x} + \grave{k}_{1z}\hat{z}$ and $\vec{k_{2s}} = \grave{k}_{2x}\hat{x} + \grave{k}_{2z}\hat{z}$ directions, let us consider the graph in Fig.2.17. Here $\left\langle a_{p-1,x_n}\left(k_{1x}\right)a^*_{p-1,x_m}\left(k_{2x}\right)\right\rangle$ and

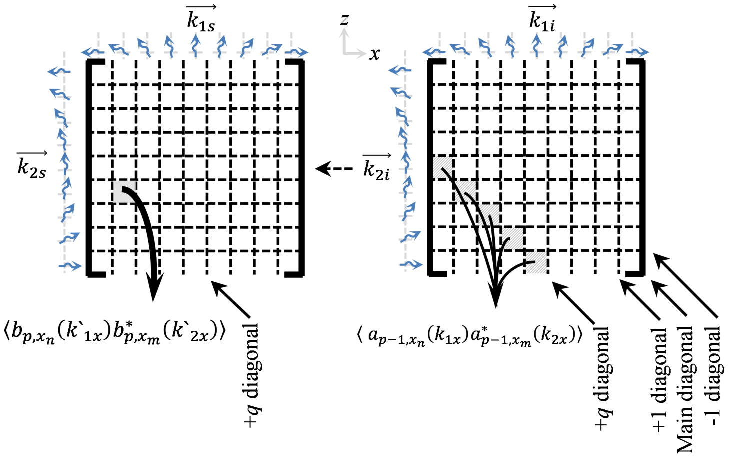

Figure 2.17: A visualization of an efficient method to calculate (2.42). For an arbitrary element $\left\langle b_{p,x_n}\left(\grave{k}_{1x}\right) b^*_{p,x_m}\left(\grave{k}_{2x}\right)\right\rangle$ in the $+q$ diagonal of the left matrix, the summation needs to be carried over all elements $\left\langle a_{p-1,x_n}\left(k_{1x}\right) a^*_{p-1,x_m}\left(k_{2x}\right)\right\rangle$ in the same $+q$ diagonal of the right matrix.

$\left\langle b_{p,x_n}\left(\grave{k}_{1x}\right) b^*_{p,x_m}\left(\grave{k}_{2x}\right)\right\rangle$ at the input and output of the p^{th} slab, are represented by two $K \times K$ matrices. Basically, we seek a method to determine the matrix on the left from the one on the right. Using (2.42), we can immediately see that the summation needs to be carried only on the elements of the $+q$ diagonal in $\left\langle a_{p-1,x_n}\left(k_{1x}\right) a^*_{p-1,x_m}\left(k_{2x}\right)\right\rangle$ matrix in order to evaluate any term in the $+q$ diagonal of the $\left\langle b_{p,x_n}\left(\grave{k}_{1x}\right) b^*_{p,x_m}\left(\grave{k}_{2x}\right)\right\rangle$ matrix. In fact, we can mathematically relate the $+q$ diagonal of the $\left\langle b_{p,x_n}\left(\grave{k}_{1x}\right) b^*_{p,x_m}\left(\grave{k}_{2x}\right)\right\rangle$ matrix to the $+q$ diagonal of the $\left\langle a_{p-1,x_n}\left(k_{1x}\right) a^*_{p-1,x_m}\left(k_{2x}\right)\right\rangle$ matrix through the following matrix multiplication

$$\left[\left\langle b_{p,x_n}\left(\grave{k}_{1x}\right) b^*_{p,x_m}\left(\grave{k}_{2x}\right)\right\rangle\right]_{+q\ diag.} = \left[H_q\right]\left[\left\langle a_{p-1,x_n}\left(k_{1x}\right) a^*_{p-1,x_m}\left(k_{2x}\right)\right\rangle\right]_{+q\ diag.} \tag{2.43}$$

where $[H_q]$ can be written explicitly as:

$$[H_q] = e^{j\left(\grave{k}_{1z}-\grave{k}_{2z}\right)L_{slab}}.$$
$$\begin{cases} \left(M\Psi_s\left(\vec{k}_{1s},\vec{k}_{1s}\right)+1\right)\left(M\Psi_s^*\left(\vec{k}_{2s},\vec{k}_{2s}\right)+1\right), & \vec{k}_{1s}=\vec{k}_{1i},\vec{k}_{2s}=\vec{k}_{2i} \text{ (diagonal elements)} \\ Me^{j\frac{q_zL_{slab}}{2}}\operatorname{sinc}\left(\frac{q_zL_{slab}}{2\pi}\right)\Psi_s\left(\vec{k}_{1s},\vec{k}_{1i}\right)\Psi_s^*\left(\vec{k}_{2s},\vec{k}_{2i}\right), & \text{else (non-diagonal elements)} \end{cases} \tag{2.44}$$

The previous result is important because it says that only plane waves in certain directions (corresponding to the diagonal elements of the matrices in Fig.2.17) interact with each other as they propagate inside the random medium. This simplification is a result of the memory effect property of the random medium (2.41). A similar approximation to the one used in (2.26a) can be used to cascade the previously introduced $[H_q]$ matrices. Thus, we can relate $\left\langle a_{1,x_n}\left(k_{1x}\right)a_{1,x_m}^*\left(k_{2x}\right)\right\rangle$ at the input of the random medium (corresponding to the source spectral radiation pattern), to $\left\langle b_{N_{slab},x_n}\left(\grave{k}_{1x}\right)b_{N_{slab},x_m}^*\left(\grave{k}_{2x}\right)\right\rangle$ at the end of the random medium through the simple matrix equation:

$$\left[\left\langle b_{N_{slab},x_n}\left(\grave{k}_{1x}\right)b_{p,x_m}^*\left(\grave{k}_{2x}\right)\right\rangle\right]_{+q\ diag.} = [H_q]^{N_{slab}}\left[\left\langle a_{1,x_n}\left(k_{1x}\right)a_{1,x_m}^*\left(k_{2x}\right)\right\rangle\right]_{+q\ diag.} \tag{2.45}$$

Equation (2.45) should be evaluated for all $+K$ diagonals and all $-K$ diagonals in order to evaluate (2.35). The same must be repeated for different x_n and x_m source positions in order to evaluate (2.33). Notice that $[H_q]$ in (2.44) is independent of the source position variables (x_n and x_m) which means that it needs to be calculated only once and reused for different x_n and x_m values.

2.5.2 Range Resolution

To estimate range resolution degradation in the random medium, frequency correlation function of the signal at the target location is needed. The phase compensated wave value at position $(0, pL_{slab})$ due to a source located at $(0, -L_{source})$ at frequency (f_n) is given by

$$\zeta\left(f_n, pL_{slab}\right) = \psi_{f_n}\left(0, pL_{slab}\right) e^{-j\left[k_o(f_n)\rho_1 + k_{eff}(f_n)\rho_2\right]} \tag{2.46}$$

from which the following normalized correlation function can be obtained:

$$R_{\zeta\zeta}\left(n, p\right) = \left\langle \frac{\frac{1}{N-|n|}\sum_m \zeta\left(f_m, pL_{slab}\right)\zeta^*\left(f_{m-n}, pL_{slab}\right)}{\frac{1}{N}\sum_m \left|\zeta\left(f_m, pL_{slab}\right)\right|^2} \right\rangle \tag{2.47}$$

To derive an analytical expression for (2.47), we follow exactly the same steps as in the previous section. A key observation here is to choose the plane wave directions considered in the spectral decomposition to have the same k_x values ($k_x : -k_o\left(f_{max}\right), -k_o\left(f_{max}\right) + 2k_o\left(f_{max}\right)/K, -k_o\left(f_{max}\right) + 4k_o\left(f_{max}\right)/K, \cdots, -k_o\left(f_{max}\right) + 2k_o\left(f_{max}\right)\left(K-1\right)/K$, and f_{max} is the maximum frequency considered) irrespective of the actual source frequency (f_n). For this choice of k_x, the corresponding k_z values are obtained from $k_z\left(f_n\right) = \sqrt{k_o^2\left(f_n\right) - k_x^2}$. Using this observation, the memory effect property in (2.41) can be used to efficiently calculate (2.42) with the same process depicted in Fig.2.17. Specifically, we can re-write (2.44) in this case to be:

$$[H_q] = e^{j\left(\grave{k_{1z}}(f_n)-\grave{k_{2z}}(f_m)\right)L_{slab}}.$$
$$\begin{cases} \left(M\Psi_s\left(f_n,\vec{k_{1s}},\vec{k_{1s}}\right)+1\right)\left(M\Psi_s^*\left(f_m,\vec{k_{2s}},\vec{k_{2s}}\right)+1\right), & \vec{k_{1s}}=\vec{k_{1i}},\vec{k_{2s}}=\vec{k_{2i}} \text{ (diagonal elements)} \\ Me^{j\frac{q_zL_{slab}}{2}}\text{sinc}\left(\frac{q_zL_{slab}}{2\pi}\right)\Psi_s\left(f_n,\vec{k_{1s}},\vec{k_{1i}}\right)\Psi_s^*\left(f_m,\vec{k_{2s}},\vec{k_{2i}}\right), & \text{else (non-diagonal elements)} \end{cases} \tag{2.48}$$

where $\vec{k_{1s}}$, $\vec{k_{1i}}$ are evaluated at source frequency f_n, while $\vec{k_{2s}}$, $\vec{k_{2i}}$ are evaluated at source frequency f_m. It is evident from (2.48) that $[H_q]$ now depends on the source frequencies (f_n and f_m) in contrast to (2.44) which did not depend on the sources positions (x_n and x_m). This means that (2.48) needs to be re-evaluated for every choice of f_n and f_m leading to longer evaluation time. This is to be expected since the presented model is a frequency domain one.

2.5.3 Comparison with Full-Wave Simulation

In order to validate the analytical expressions for the correlation functions defined in (2.33) and (2.47), a full-wave model combined with Monte Carlo simulations is employed. Again, the full-wave simulation technique adapted here is based on the T-matrix method presented in [70] for the case of an incident single plane wave. For the case of sources with complicated radiation pattern, the method needs to be modified. The Generalized Lorenz-Mie theory which deals with the scattering of electromagnetic waves from spheres or cylinders under an arbitrary shaped beam excitation can be used [83]. In the antenna far-filed region, (2.31a) can be expressed in terms of the Hankel functions of the first kind as:

$$\psi_{Gaussian}\left(\vec{\rho}\right) = \sum_{n=-\infty}^{+\infty} A_n H_n^{(1)}\left(k_o\rho\right) e^{jn\theta} \sim \frac{e^{jk_o\rho}}{\sqrt{\rho}} \sum_{n=-\infty}^{+\infty} \left(\sqrt{\frac{2}{\pi k_o}} e^{-j\frac{(2n+1)\pi}{4}} A_n\right) e^{jn\theta} \tag{2.49}$$

which has the same functional dependence on (ρ) as (2.31a). Thus, using the orthogonality relation for $(e^{jn\theta})$, it is straight forward to write down:

$$A_n = \frac{\sigma}{2}\sqrt{\frac{\pi}{k_o}} e^{j\frac{(2n+1)\pi}{4}} e^{\frac{-\sigma^2 n^2}{2}} \left[\operatorname{erf}\left(\frac{\pi + j\sigma^2 n}{\sqrt{2}\sigma}\right) - \operatorname{erf}\left(\frac{-\pi + j\sigma^2 n}{\sqrt{2}\sigma}\right)\right] \tag{2.50}$$

where erf() is the complex error function.

The correlation function defined in (2.33) is evaluated in Fig.2.18 for three cases: (a) free space propagation, (b) full wave simulation averaged over 50 Monte Carlo realizations, and (c) analytically. Similar to the previous sections, the random medium is generated using the sequential addition method [73] with a surface fraction value of $\Phi = 1\%$ and it is composed of identical cylinders with radii $r_s = 3\lambda$ and dielectric constant of $\epsilon_r = 5 + j1$. Other simulation parameters used are: frequency = 240 GHz, number of plane wave modes (K) = 1024, number of slabs = 100, $L_{slab} = 16\lambda$, $L_{source} = 500\lambda$, and $W_{slab} = 512\lambda$. For the case of free space propagation (no scatterers), as expected the correlation function tapers slowly towards the edges as n increases. A numerical artifact is observed as the correlation function is larger than one due to the normalization factor $(1/N - |n|)$ introduced in (2.33). Good agreement is observed between Fig.2.18(b) and (c) pointing at the validity of the analytical expression. Both of these figures show that the correlation function tapers progressively as a function of the propagation distance inside the random medium. Thus, only over a limited lateral range a synthetic array can be formed that can effectively focus inside the random medium. This lateral range is inversely proportional to the depth of focus in the medium.

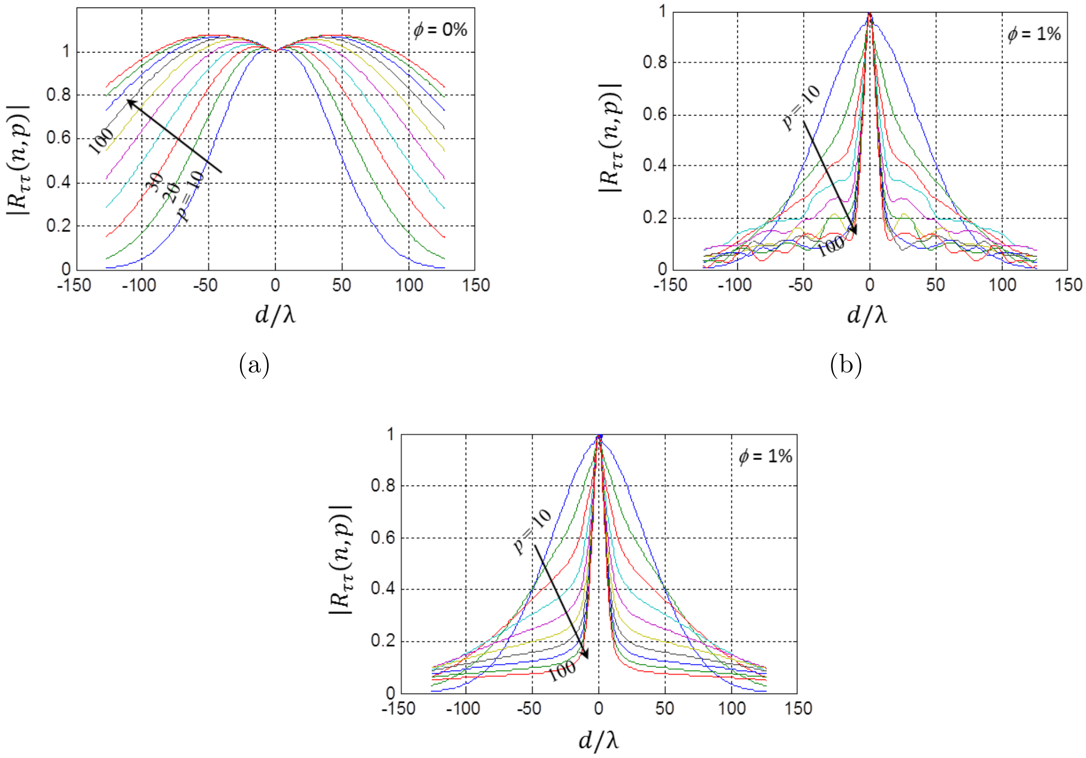

(a)

(b)

(c)

Figure 2.18: Normalized correlation function as defined in (2.33) evaluated at the output of the p-slab, $p = 10, 20, \cdots, 100$ for three cases: (a) Free space propagation. (b) Numerically for a random medium with surface fraction (Φ) of 1% averaged over 50 Monte Carlo realizations. (c) Analytically, for the same random medium parameters.

Also, we can notice that the correlation function gets narrower and narrower until it saturates at a fixed width after certain propagation distance inside the random medium (around 50 slabs or 800λ). This effect is counter intuitive as one may expect the correlation function to get narrower monotonically as function of the propagation distance. The reason for the saturation behavior can be explained by examining the so called "average center-to-center distance between a scatterer and its nearest scatterer $\langle R \rangle$" of the random medium. For a random medium consisting of uniformly distributed identical cylinders, this function can be written as [71]:

$$\langle R\rangle = \frac{r_s e^{4\Phi}}{\sqrt{\Phi}} \int_{4\Phi}^{\infty} x^{1/2} e^{-x} \mathrm{dx} = \frac{r_s e^{4\Phi}}{\sqrt{\Phi}} \Gamma\left(\frac{3}{2}, 4\Phi\right) \tag{2.51}$$

where $\Gamma(\cdots,\cdots)$ is the upper incomplete gamma function. By evaluating (2.51) for our simulation parameters, namely $r_s = 3\lambda = 3.7\,mm$ and $\Phi = 1\%$, the average distance $\langle R\rangle$ is computed to be 34.3 millimeter or 27.5λ. This value is much larger than source movement step ($\lambda/2$). Thus, the source will basically "see" the same medium as long as it moves on a scale that is much smaller than $\langle R\rangle$. In fact, from Fig.2.18(c) it is clear that the minimum aperture coherence length is about 12λ corresponding to the full width at half maximum of the correlation function. This value is around $1/2\,\langle R\rangle$. The same basic behavior can be observed in Fig.2.19(a) and (b) for surface fraction values of $\Phi = 0.5\%$ and 1.5%, respectively. It is also observed that correlation function becomes narrower for higher surface fraction values. The full width at half maximum for both cases are 19λ, and 10λ, respectively, while $\langle R\rangle$ is 38.3λ, and 22.8λ. It is interesting to mention at this point that if we set the non-diagonal elements to zero in (2.44), then we will end up with the same free-space normalized curve as in Fig.2.18(a). Basically, the signal will be attenuated according to Foldy's approximation without losing its coherency. Next, (2.47) is evaluated to assess the coherence as a function of the source frequency. The simulation parameters are the same as before but here the source position is fixed and the frequency is varied from 220 GHz to 260 GHz. Figure 2.20(a) shows the full-wave simulation result averaged over 50 Monte Carlo realizations, while Fig.2.20(b) shows the analytical counterpart. Again, good agreement is observed indicating the validity of the analytical expression. Some discrepancies are observed for the far way slabs due to the limited number of Monte Carlo iterations performed. It is interesting to note that the correlation function is rather smooth even for a very large bandwidth ($\sim$ 40 GHz). This can be attributed to the fact that both the transmitter and

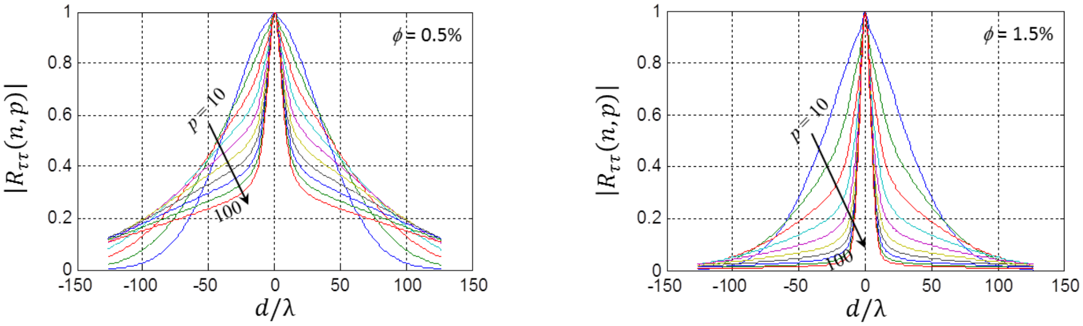

(a) (b)

Figure 2.19: Normalized correlation function as defined in (2.33) evaluated analytically for two surface fraction values. (a) $\Phi = 0.5\%$. (b) $\Phi = 1.5\%$.

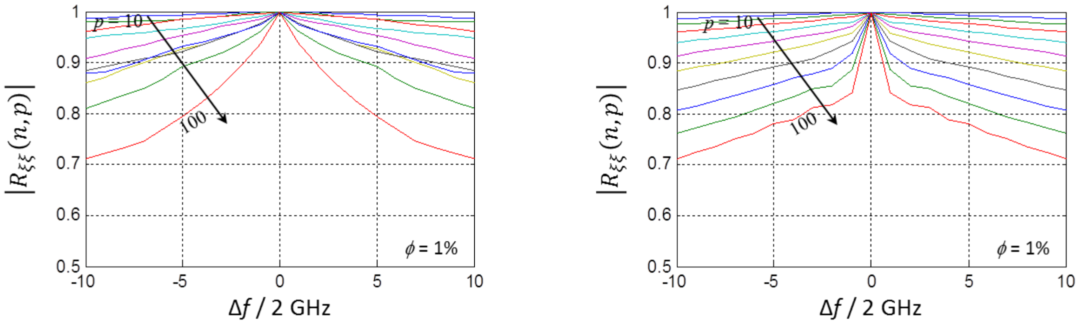

(a) (b)

Figure 2.20: Normalized frequency correlation function as defined in (2.47) evaluated at the output of the p-slab, $p = 10, 20, \cdots, 100$ for: (a) numerically for a random medium with surface fraction $\Phi = 1\%$ averaged over 50 Monte Carlo realizations, and (b) analytically for the same random medium parameters.

random medium are stationary in this scenario which means that the same multiple scattering will take place at every frequency but with different phases. This was not the case for the cross-range resolution scenario discussed before.

Next, a full wave simulation of SAR imaging the random medium is considered. Again the source is moved from $-W_{slab}/4$ to $+W_{slab}/4$ in steps of $\lambda/2$. The source bandwidth is determined from the required range resolution ($\sim 5\lambda$), while the number of frequency points is determined from the free spectral range calculations ($100 \times 16\lambda$). In this simulation, the frequency is varied from 225.6 GHz to 254.4 GHz with a step of 62.5 MHz leading to 462 frequency points. To draw the SAR image, standard SAR signal processing algorithm is used. Specifically, the image function at a specific point (x, z) is calculated from:

$$\begin{aligned} g_{image}(x,z) &= \rho \left| \sum_{x_n} \sum_{f_s} \psi_{x_n,f_s}(0, -L_{source})\, e^{-2j\left[k_o(f_s)\rho_1(x_n,x,z)+k_{eff}(f_s)\rho_2(x_n,x,z)\right]} \right| \\ &= \rho \left(\sum_{x_n} \sum_{f_s} \sum_{x_m} \sum_{f_p} \chi_{x_n,f_s}(x,z)\, \chi^*_{x_m,f_p}(x,z) \right)^{1/2} \end{aligned} \tag{2.52}$$

where $\chi_{x_n,f_s}(x,z)$ is the phase compensated signal received by the source while it is transmitting at location (x_n) with frequency (f_s), and the (ρ) factor is introduced to compensate for the two-way free-space propagation path-loss. The resulting image for a random medium with surface fraction value of 1% is shown in Fig.2.21(a). Here, we do not have an actual target but rather use the cylinders themselves to examine the point spread function. For the first few cylinders, the resolution is very good and it is easy to distinguish nearby cylinders from each other. As the propagation distance inside the random medium increases, the cross resolution degrades rapidly and adjacent cylinders at the same range cannot be distinguished from each other. However, the range resolution does not degrade as much. Both of these observations agree with correlation functions shown in Fig.2.18(c) and Fig.2.20(b). Fig.2.21(a) also shows that the speckle level is very high due to the multiple scattering. Furthermore, some of the cylinders are not actually imaged due to the shadowing effect.

At this point, it is important to ask whether it is possible to enhance the quality of the SAR image through a random medium. Using coherent imaging, the cross-range resolution

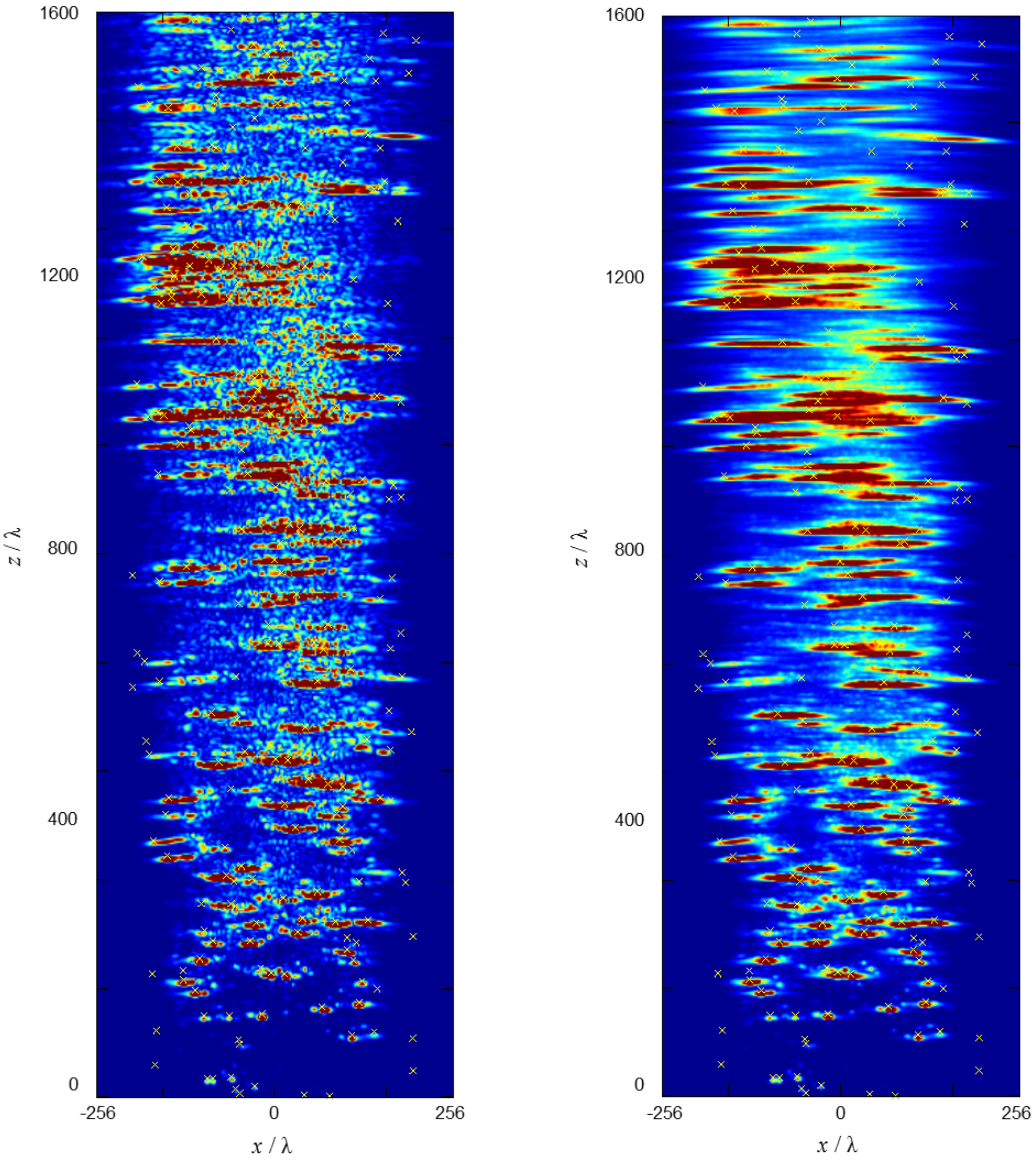

(a) (b)

Figure 2.21: Complete 2D SAR imaging scenario. The cylinders are indicated with (×) mark. (a) SAR image formed by standard processing according to (2.52). (b) Enhanced SAR image formed by (32).

of the image degrades as discussed before. However, by properly combining the values of $\chi_{x_n,f_s}(x,z)$, the speckle level can be reduced. This can be done by examining (2.52) and noting that the summation over the source locations is the main factor affecting the cross-range resolution. The double sum $\left(\sum_{x_n}\sum_{x_m}\chi_{x_n,f_s}(x,z)\,\chi^*_{x_m,f_p}(x,z)\right)^{1/2}$ can be visualized again as summing the elements of the matrix shown in Fig.2.22. Without any clutter, all the elements in the shown matrix contribute to the SAR image at a certain point (x,z) giving rise to the theoretical cross resolution of the SAR system ($\sim L/2$). In fact, at distant points from the source, it is the off-diagonal elements of the shown matrix that contribute the most to the SAR cross-resolution. In the presence of clutter, Fig.2.18 tells us that only few source locations close to each other can focus coherently on the target. This corresponds to the near diagonal elements shown in gray in Fig.2.22. Furthermore, as the target range increases, the Grey region decreases progressively until it saturates at a fixed value. Thus, by realizing that at a given range, the source locations far away from each other do not actually enhance the image cross-resolution but rather contribute noise, we can modify (2.52) to be:

$$g_{image}(x,z)=\rho\left(\sum_{x_n}\sum_{x_m}R_{\tau\tau}\left(|n-m|\,,p(z)\right)\cdot\chi_{x_n,\overline{f}}(x,z)\,\chi^*_{x_m,\overline{f}}(x,z)\right)^{1/2} \tag{2.53}$$

here $\chi_{x_n,\overline{f}}(x,z)$ is the phase compensated signal at source position (x_n) averaged over all source frequencies, and $p(z)$ refers to the slab number (p) at which the search point (x,z) is located. The previous equation basically scales the contribution of every term $\left(\chi_{x_n,\overline{f}}(x,z)\,\chi^*_{x_m,\overline{f}}(x,z)\right)$ according to the correlation function defined in (2.33). The resulting SAR image is shown in Fig.2.21(b). By comparison with Fig.2.21(a), it can be seen that both range and cross-range resolutions are basically the same, however, the speckle level is highly reduced.

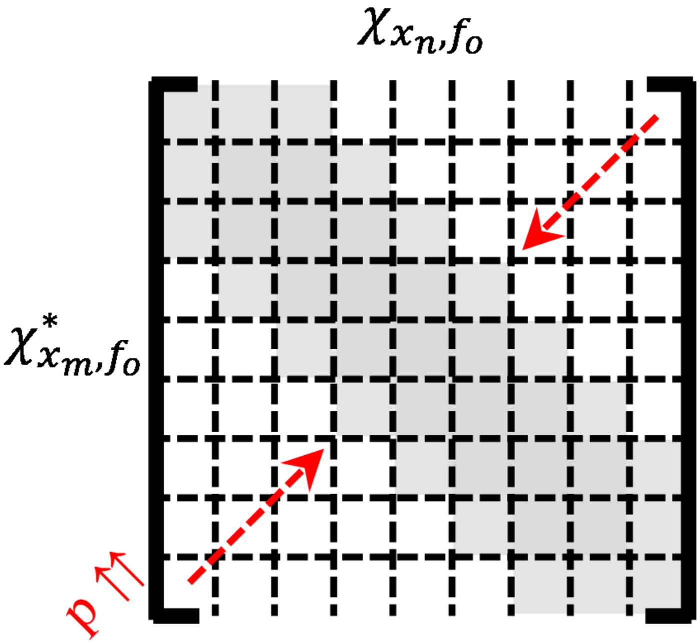

Figure 2.22: Visualization of (2.53) showing the true source locations contributing to forming the SAR Image. 'P' indicates the slab number which is proportional to the propagation distance.

Finally, two issues are important to mention here. First, the introduced correlation functions in (2.33) and (2.47) actually deal with only the forward propagation direction which is half of the imaging problem. They are more suited to source localization kinds of problems. A more useful function would be the point spread function that is usually used to characterize the resolution of imaging systems. Although it is possible to analytically derive such function using similar framework for calculating backward scattered power, we did not do it here. This is mainly because the ASSWaP-SD is not highly accurate in the forward/backward directions as it does not account for the enhanced back scattering due to reciprocal wave paths as mentioned before (look at Fig.2.12). A possible solution is to combine the numerical

SSWaP-SD with Monte Carlo technique to numerically evaluate the point spread function. This can save large simulation time compared to full-wave simulation. Second, it might be possible to enhance the cross range resolution by augmenting the image algorithm with incoherent imaging. Thus, instead of minimizing the contribution of two source positions when they are far apart, we can somehow combine them incoherently to enhance the overall cross-resolution. However, this method is not further pursuit here.

2.6 Conclusion

A rigorous wave propagation model capable of predicting path-loss over long distances and backscattered power is developed. Compared to other models, it has the advantage of tracking both the magnitude and phase of the wave as it propagates inside the random medium. Thus, it can be used to assess the performance degradation of coherent imaging systems working in random media. The approach is based on a Statistical Scattering- matrix for Wave Propagation in Spectral Domain, or SSWaP-SD, which is applicable for random media composed of sparse collection of discrete scatterers. In this approach the random medium is discretized into slabs with appropriate thickness, and each slab is represented by a high order bistatic scattering matrix. By cascading the scattering matrices of the individual slabs, the scattering matrix of the entire medium is calculated very efficiently. An analytical expression is also developed for the special case of translationally invariant, discrete, sparse, random medium. It is shown that Foldy's approximation can be used to predict the path-loss accurately as long as the wave is dominated by the mean field. This is not the case for long distance propagation for which the wave is dominated by the incoherent component. In this case, Foldy's approximation will predict higher attenuation rate because it does not account for the ability of the medium to redirect some of the scattered energy through multiple scattering to the forward direction. The proposed numerical algorithm (SSWaP-SD) and the analytical counterpart (ASSWaP-SD) are validated using full-wave simulation and shown to predict the "knee point" of the dual-slope attenuation curve, as well as the back scattered power accurately. The proposed algorithm can be also be adapted to other scenarios such as random media with non-identical scatterers with a known particle distribution function, or even random media with inhomogeneous distribution in the propagation direction.

The ASSWaP-SD analytical model is then expanded and used to study the SAR resolution degradation in 2D sparse random medium in both cross-range and range directions. To quantify the resolution degradation, appropriate correlation functions are defined. It was found that the degradation in the cross-range direction is severe and it gets worse as the imaging range increases until it saturates at a constant value. This value is related to the average center-to-center distance between a scatterer and its nearest neighbor which characterizes the scale at which the random medium can be considered translational invariant. Furthermore, the cross-range degradation increases with the surface fraction of the random medium. For the range resolution, however, it is found that the degradation is small even for a very large bandwidth. A complete SAR imaging scenario is presented and the degradation in resolution was found to comply with the predicted correlation functions. A novel method is proposed to reduce the speckle level of the SAR image without sacrificing the resolution.

CHAPTER III

Sub-Terahertz Dielectric Measurement and Its Application to Concealed Object Detection

3.1 Introduction

The study of electrical properties of different materials has always been of great importance in material science, electrical and electronic engineering, bio-engineering, solid-state physics, and optics. In electromagnetics, the most important electrical properties are dielectric permittivity, magnetic permeability, and electric conductivity. This is because the behavior of any material exposed to electromagnetic radiation can be completely characterized from these properties. In this chapter, we focus on the dielectric property as most materials, and especially the materials we are interested in, are non-magnetic.

In the past fifty years, many dielectric measurement techniques have been proposed [84]. Depending on the frequency of interest, bandwidth, and the sample properties (size, shape, phase, etc.), a particular measurement technique may be more appropriate than the others. Generally speaking, dielectric measurement techniques can be divided into two categories:

1) resonant methods, and 2) non-resonant methods [84]. Resonant methods rely on putting the sample under test in an appropriate resonator (cavity, transmission line, Fabry-Perot etalon, etc.) and through measuring the shift in the resonant frequency and change in the quality factor, the complex permittivity near the resonance is determined. The advantage of such method is the high accuracy of the results, while the disadvantages include the inherent narrow bandwidth as well as the difficulty in sample preparation. On the other hand, non-resonant methods rely on measuring the transmission and/or reflection of the electromagnetic wave from the sample after putting it in free space or within a transmission line. It has the advantage of broadband characterization and ease in sample preparation at the expense of lower accuracy results. Thus, resonant methods are usually used when the dielectric permittivity at a specific frequency is required with high accuracy, while non-resonant methods are used for broadband characterization.

As the frequency of operation increases, the sample preparation becomes a major hindrance due to small size of both the sample and the resonator rendering the resonant methods impractical. For example, at 300 GHz, the free-space wavelength is about 1mm, and a regular $\lambda/2$ resonator will be only 0.5 mm. Thus, the machining precision needs to be at least better than 50 μm. This is why non-resonant methods are more popular in the sub-THz frequency band (0.1$\sim$10 THz) [85]–[90].

A key point in THz spectroscopy is the generation and coherent detection of the THz signal with large enough power level. Conventionally, the THz radiation is generated through photoconductive techniques. Basically, a semiconductor material with appropriate bandgap energy level is excited by a femto-second laser, generating currents through the excitation of electron-hole pairs. To optimize the radiation process, a metal pattern is typically applied to the semiconductor surface in the form of an antenna structure. With this metallization, a large DC bias can be applied to the illuminated region of the semiconductor, which enhances the generated photocurrent. The antenna structure also helps to couple the THz radiation into free space. Such THz spectroscopy system is commonly known in the literature as Terahertz Time-Domain Spectroscopy (THz-TDS) system and is described in many publications [85]–[90]. This system can potentially provide a huge bandwidth. Typical operating frequency ranges in the literature span from sub-THz to about 5 THz with the output power decreasing exponentially as the frequency increases leading to lower dynamic range at the far end of the spectrum. Primary challenges for these systems include: low output power, low efficiency, and the requirement of a high sensitivity detectors as well as femto-second laser sources which can be quiet expensive.

With the recent advances in solid state devices, it has become possible to extend the capabilities of Vector Network Analyzers (VNA) to the lower THz region through the use of frequency extenders. At the time of writing this thesis, frequency extenders covering the band (0.75 – 1.1 THz) are commercially available from Virginia Diodes, Inc. The advantage of using a VNA-based system is the possibility to perform calibrated magnitude and phase transmission and reflection measurements with a very large dynamic range, while the disadvantage is the limitation in high frequency ($f < 1.1$ THz).

In this chapter, a network-analyzer-based dielectric measurement system working in the frequency band (220 – 325 GHz) is presented. The purpose of this study is to use such system for characterizing the dielectric constant of different materials that are important for the problem of radar-based concealed object detection. Most results found in the literature reports only the transmittance spectra of different clothes materials in the THz frequency region [91]–[93]. In this study, we take the extra step of retrieving the dielectric constant of such materials with different moisture content which is important for modeling purposes. In a recent study, it has been shown that polarimetric J-band radars can be used for stand-off detection of concealed objects on human body [94]. To make such radars portable as a hand-held device, the frequency of the radar must be increased. An important phenomenological aspect of concealed object detection using sub-THz radar is the effect of the clothing on the backscattered from the individual under radar illumination. For this purpose, the dielectric constant of different fabric materials as well as that of the human skin is needed.

This chapter is organized as follows: first, a general description of the measurement setup is presented in Section 3.2. Then, the measurement procedure as well as the dielectric retrieval algorithm for the fabrics are discussed in Section 3.3. Measurement uncertainty quantification is also discussed in Section 3.3. Finally, the dielectric measurement method and results for the human skin are reported in Section 3.4. The material in this chapter can be found in [37], [95]

3.2 Network-Analyzer-Based Dielectric Setup Measurement Description

The setup used in the first part of this study is depicted in Fig.3.1. Basically, it is a modified version of the one presented in [96] which operated in the frequency band (75 – 95 GHz). It consists of Agilent N5245A Network Analyzer (10 MHz - 50 GHz) connected to two J-band OML frequency extender modules (220 – 325 GHz). The two frequency extenders are mounted on two separate xyz manual precision stages. Each frequency extender is terminated with a standard gain horn antenna operating in the entire J-band. Each antenna has a gain of about 24.5 dBi, and HPBW of 8.8^o and 9.2^o in elevation and azimuthal directions, re-

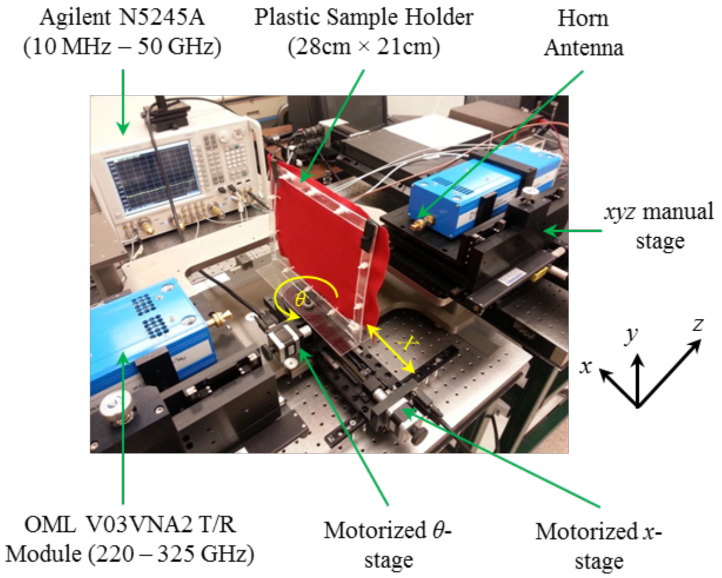

Figure 3.1: Picture of the measurement setup along with major components.

spectively. To satisfy the far-field criteria, the distance between the transmitter and receiver antennas are adjusted to be around 32 cm, and the sample is centered in between. Thus, the spot size on the sample can be estimated from the HPBW to be around 2.46 cm × 2.57 cm. The sample holder consists of a plastic frame of size 28cm × 21cm with plastic screws. Such dimensions are chosen to be much larger than the radius of the first Fresnel zone (about 1 cm at the center of the band) in order to minimize the diffraction from the frame edges. The plastic frame is mounted over a motorized rotational stage, which is also mounted over a motorized translational stage. This configuration allows for measuring the sample at different translational positions as well as different azimuthal angles. The translational stage has a resolution of 2.5 μm, while the rotational stage has a resolution of 0.005^o. The network analyzer and the two translational stages are connected to a PC computer and controlled through MATLAB software.

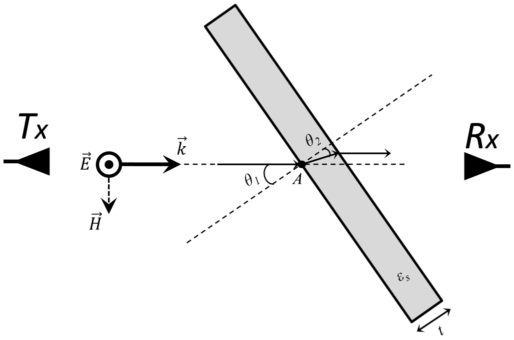

Figure 3.2: Transmission through a uniform dielectric slab for the case of TE (perpendicular) polarization.

3.3 Measurement of Fabric Materials

Since the fabric materials considered are in the form of thin sheets, we use the standard retrieval algorithm presented in [96]. The basic idea is to measure the transmission coefficient through the sample under test, and normalize it by the measured free space transmission coefficient (in the absence of the sample). By comparing the calibrated measured transmission coefficient with the theoretical one for a homogeneous dielectric slab, the value of the dielectric constant can be obtained. Mathematically, the transmission coefficient through a homogeneous dielectric slab (see Fig.3.2) of thickness (t) and relative dielectric constant (ε_s) can be written as:

$$T_{th}\left(t,\varepsilon_s,f,\theta_1\right)=\left[\frac{1}{1-R^2e^{j2k_2t\cos(\theta_2)}}\right]\cdot\left[\left(1-R^2\right)e^{j(k_2t\cos(\theta_2)-k_1t\cos(\theta_1))}\right] \tag{3.1}$$

where θ_1 is the incidence angle, θ_2 is the refracted angle obtained from Snell's law, k_1 is the free space wavenumber, k_2 is the wavenumber inside the dielectric slab, and R is the Fresnel reflection coefficient from a dielectric half space which depends on the wave polarization. The transmission coefficient in (3.1) is referred to point (A) in Fig.3.2 so that in can be compared directly with the measured normalized quantity. The first bracket in (3.1) represents the Fabry-Perot effect of the dielectric slab, while the second bracket represents the direct transmission contribution. At this point, it is important to emphasize that while it is possible to use both the transmission and reflection measurement data to retrieve the dielectric constant as presented in [97], here we rely only on the transmission information as such quantity is independent of the exact position of the sample between the transmitter and receiver antennas. Using the reflection data requires special calibration procedure which becomes very difficult to perform at the considered frequency range. In addition, any ripples over the sample surface will highly affect the reflection coefficient, but such ripples do not affect the transmission coefficient significantly as we will show later.

It is well known that (3.1) is not a one-to-one function between the complex dielectric constant and the complex transmission coefficient (assuming the thickness is given). Thus, the transmission coefficient is usually measured over huge bandwidth at one angle of incidence as in THz-TDS systems [85]–[89], or over moderate bandwidth at multiple angles of incidence as in [96], [98]. However, it should be noted that the expected variation in the complex permittivity over the bandwidth used must be small. The goal for using the wide bandwidth and multiple angles of incidence is to form an over determined system of equations that can be solved for the unknown dielectric constant of the material.

It is imperative to take a look on the nature of the material considered as it will have a direct impact on the choice of the retrieval algorithm. Nearly all fabrics show variation in their thickness across the sample. In other words, the material has some thickness undulations that are function of fabrication as well as local stretching or pulling forces during the measurement. These undulations are in addition to the small scale periodic surface roughness of most fabrics. Our approach to mitigate the thickness undulations includes three steps. First, we allow for a relatively large beam spot on the measurement sample which tends to average the surface roughness and thickness fluctuations. Second, many independent measurements for the same sample are carried out by moving the sample laterally (in the $\pm x$ direction) using the translational stage. Finally, the retrieval algorithm is implemented in such a way to allow for retrieving both the complex dielectric constant as well as the effective sample thickness. The last step is already implemented in THz-TDS systems as presented in [86]. Specifically, it was shown that if the wrong sample thickness is used in the retrieval algorithm, then the retrieved complex dielectric constant will exhibit artificial oscillations over the frequency. The frequency of such oscillations is given by:

$$F_{osc} = \frac{c}{2\sqrt{\varepsilon_s}t} \tag{3.2}$$

where c is the speed of light in free space. The problem with this approach is that such oscillations can only be observed over a very large bandwidth for which there may be natural variations of the dielectric constant. For example, a typical material with thickness of $500\mu m$ and dielectric constant of 4, will lead to an oscillation frequency of 150 GHz which is higher than the available bandwidth for our system. To circumvent this problem, we measure the complex transmission coefficient not only over frequency, but also across multiple incident angles. Thus, by combining the information from the available frequency bandwidth with the information from multiple angles of incidence, both the complex dielectric constant and effective sample thickness can be obtained. In addition to the thickness undulations, the presence of small scale periodic roughness may lead to coupling of some of the incident energy to Bragg modes. The energy coupled to the Bragg modes is not captured by the receiving antenna through the forward transmission coefficient measurements. Such energy loss will be interpreted as additional dielectric loss factor. From the samples we used, only wool and jeans fabrics have a discernible periodic pattern. The periods are of the order of 1mm $\sim$ 2mm. Thus, we should expect the presence of at least the -1, 0, +1 Bragg modes in the rage of incident angles we used ($10^o \leq \theta_{inc} \leq 40^o$). However, it should be mentioned here that the diffraction is mostly coming from the surface undulation of the fabrics and not significantly from the volume scattering (dielectric contrast between the fabric material and air). Basically, the fabrics are so tightly woven that the air gaps are extremely small and in some cases do not exist. Thus, we can argue that although the Bragg modes can appear in principle, the power coupled to such modes are very small since the surface roughness of the fabric materials is much smaller than the wavelength.

Now, we describe the measurement procedure used in this part. The basic idea is to measure the transmission coefficient through the sample at 13 different x-positions that are separated by 3 mm. For each sample position, the transmission coefficient is measured at five azimuthal angles ($0^o,10^o, \cdots, 40^o$). The upper limit of 40^o incident angle is chosen in order to avoid signal contamination from the sample holder edge diffraction. In order to mitigate the drift in the network analyzer parameters, a fresh free-space transmission measurement is made before each of the 13 measurements. This is done be moving the sample to the maximum x-position, then rotating it to 90^o in order to clear the line of sight between the transmitter and receiver antennas. For all cases, the transmission coefficient (S_{21}) is measured using the network analyzer over the 220 – 325 GHz frequency band in two steps. The first step is from 220 GHz to 242.44379 GHz with 172 frequency points, averaging number of 2, and IF bandwidth of 500 Hz. The second step is from 243.7526 GHz to 325 GHz with 620 frequency points, averaging number of 5, and IF bandwidth of 500 Hz. These settings are used to reduce the repeatability error in the network analyzer measurements as will be described later. The time to finish one measurement is about 150 seconds. For all transmission coefficient measurements, standard time domain gating procedure is used to eliminate any reflection from nearby objects.

Next, the retrieval algorithm is described. The major assumption made is that the complex relative permittivity of the sample is constant over the entire frequency band. Such assumption is justified by the relatively low bandwidth of the measurement system, and by the comparison between the measured normalized transmission coefficient and the theoretical one based on the retrieved dielectric constant and thickness values. If more accurate results are required, then a causal regression model for the dielectric constant can be assumed [99]. We start by calculating a rough estimate of the range of material thickness and the corresponding range of real part of the sample's dielectric constant. Initially the sample thickness is measured using a standard vernier with resolution of 1 mill. During this thickness measurement, the sample is squeezed as much as possible with the vernier. Many thickness measurements from different points on the sample are taken and averaged in order to obtain a nominal value for the thickness t_{nom}. We allow for some variation in the thickness for the retrieval algorithm. Thus, the algorithm will search for the effective sample thickness within a range around t_{nom}. Next, the previous thickness range is divided into appropriate number of points (t_k, $k = 1, 2, \cdots, K$), and for each thickness, the real part of the sample dielectric constant is estimated from the phase information of the measured transmission coefficient. As in [89], most of the phase variation of the transmission coefficient over frequency comes from the exponential term in (3.1), while the contributions from other terms are of secondary nature. To find the real part of the complex permittivity that corresponds to certain thickness value (t_k), the following objective function is defined:

$$OF_1\left(t_k, \mathrm{Re}\left(\varepsilon_s\right)\right) = \sum_{f_m=220\mathrm{GHz}}^{325\mathrm{GHz}} \sum_{\theta_{n1}=0^o}^{40^o} \left[\angle T_{meas}\left(f_m, \theta_{n1}\right) - \left(\frac{2\pi f_m}{c} t_k \left(\sqrt{\mathrm{Re}\left(\varepsilon_s\right)} \cos\left(\theta_{n2}\right) - \cos\left(\theta_{n1}\right)\right)\right)\right]^2 \tag{3.3}$$

where $T_{meas}\left(f_m, \theta_n\right)$ is the measured transmission coefficient through the slab at frequency f_m and angle θ_n after normalization by the free-space transmission coefficient. Many numerical algorithms exist in the literature to solve the non-linear least square fitting problem given by (3.3). Here we adapt a brute-force method in which we evaluate (3.3) over a very fine grid of $\mathrm{Re}\left(\varepsilon_s\right)$ values and pick up the value that minimizes (3.3). This is done to avoid the common problem of choosing an initial search point that might result in reaching a local minimum rather than a global one. After this step, we end up with a range of thickness values, and the corresponding range of '$\mathrm{Re}\left(\varepsilon_s\right)$' values. Next, the following objective function is defined:

$$\begin{aligned} OF_2\left(t_k, \mathrm{Re}\left(\varepsilon_s\right), \mathrm{Im}\left(\varepsilon_s\right)\right) = \sum_{f_m=220\mathrm{GHz}}^{325\mathrm{GHz}} \sum_{\theta_{n1}=0^o}^{40^o} & \left[\ln\left|T_{meas}\left(f_m, \theta_{n1}\right)\right| - \ln\left|T_{th}\left(t, \varepsilon_s, f_m, \theta_{n1}\right)\right|\right]^2 \\ & + \left[\angle T_{meas}\left(f_m, \theta_{n1}\right) - \angle T_{meas}\left(t, \varepsilon_s, f_m, \theta_{n1}\right)\right]^2 \end{aligned} \tag{3.4}$$

This objective function relies on comparing the magnitude and phase of the measured and theoretical transmission coefficients. The objective function has fewer number of local minima compared to an objective function constructed from the real and imaginary parts of the transmission coefficient [85]. We resort to brute force minimization technique by evaluating (3.4) over a fine 3D mesh for 't_k', '$\mathrm{Re}\left(\varepsilon_s\right)$', and '$\mathrm{Im}\left(\varepsilon_s\right)$' variables to identify the value that minimizes the objective function. This retrieval algorithm can find the global minimum at the expense of taking more time, but considering the simplicity of the function this penalty is not that important. This computation takes less than few seconds over a personal computer

(3.4GHz, quad core processor and 16 GB of RAM).

An important factor in any measurement approach is error analysis and error quantification. Errors in this measurement can be categorized into two groups: 1) errors associated with the measurement system and related calibration issues, and 2) sample preparation and positioning such as sample thickness variations and orientation errors. As a first step, the network analyzer was calibrated using the standard 2-port waveguide calibration method with short, offset shorts, load, and through measurements. This method is necessary to remove the response of the frequency extenders from the measurements. The next step is to characterize the repeatability of the transmission measurement. For this purpose, fifty traces are collected without samples attached to the plastic frame according to the previously described procedure. The resulting normalized transmission coefficient curves for $\theta = 20^o$ is shown in Fig.3.3. The maximum magnitude fluctuation is about ±0.15 dB. For the phase fluctuation, a systematic error is observed specially in the 220 – 242.5 GHz band of about -3.5^o, while it was about 0.8^o for the 242.5 – 325 GHz band. This systematic error is observed for all other angles. Figure 3.4 shows the measured normalized transmission coefficient averaged over the fifty traces. From the phase fluctuation curve, we can immediately notice the systematic drift in the measurement phase with time. This drift is worst for larger angles because they are measured later in time. The initial systematic phase jump at $\theta = 0^o$ is due to the time taken to move the translational stage and rotational stage from their respective zero positions (at which free-space measurements are performed) to the measurement position which is about 12 seconds. We can also see that the drift is worst for the band 220 – 242.5 GHz which is why we averaged only twice instead of five times for this band. If five times averaging is used for this band, the phase fluctuation will be much worst. The reason for this phase fluctuation is not completely understood but we found after long investigations that it is

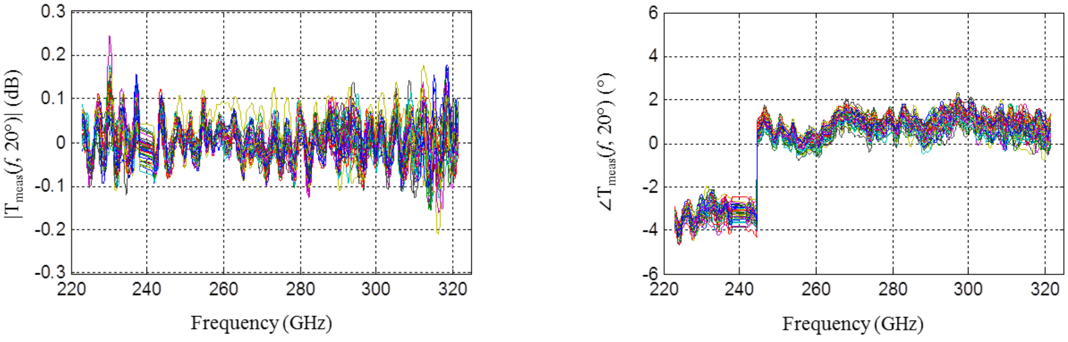

(a) (b)

Figure 3.3: Repeatability error for the network analyzer measurements (after the application of time domain gating) for the case of plastic frame without any sample at $\theta = 20^o$.

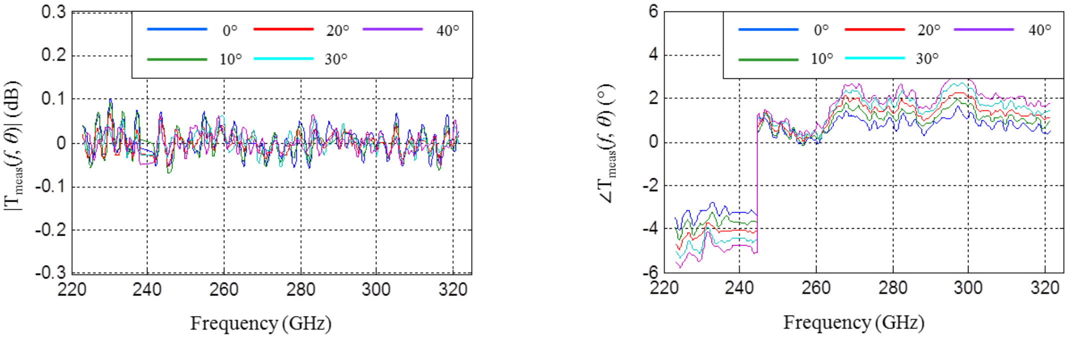

(a) (b)

Figure 3.4: Repeatability error for the network analyzer measurements (after the application of time domain gating) averaged over fifty measurements.

related to the direct connection between the network analyzer and frequency extenders used in our setup (Fig.3.1). If Agilent millimeter-wave controller set is used, then the systematic phase fluctuation can be avoided. Unfortunately, such equipment was not available during the time of the experiment. Since the phase error is dominated by the systematic part, it is possible to take it into consideration by subtracting such systematic error from further measurements. However, this was not implemented because this phase error was observed to vary on the scale of few hours. Instead, the objective functions defined in (3.3) and (3.4) are modified to be:

$$OF_1\left(t_k, \mathrm{Re}\left(\varepsilon_s\right)\right) = \sum_{f_m=247\mathrm{GHz}}^{325\mathrm{GHz}} \sum_{\theta_{n1}=0^o}^{40^o} \left[\angle T_{meas}\left(f_m, \theta_{n1}\right) - \left(\frac{2\pi f_m}{c} t_k \left(\sqrt{\mathrm{Re}\left(\varepsilon_s\right)}\cos\left(\theta_{n2}\right) - \cos\left(\theta_{n1}\right)\right)\right)\right]^2 \tag{3.5a}$$

$$\begin{aligned} OF_2\left(t_k, \mathrm{Re}\left(\varepsilon_s\right), \mathrm{Im}\left(\varepsilon_s\right)\right) = & \sum_{f_m=220\mathrm{GHz}}^{325\mathrm{GHz}} \sum_{\theta_{n1}=0^o}^{40^o} \left[\ln\left|T_{meas}\left(f_m, \theta_{n1}\right)\right| - \ln\left|T_{th}\left(t, \varepsilon_s, f_m, \theta_{n1}\right)\right|\right]^2 \\ & + \sum_{f_m=247\mathrm{GHz}}^{325\mathrm{GHz}} \sum_{\theta_{n1}=0^o}^{40^o} \left[\angle T_{meas}\left(f_m, \theta_{n1}\right) - \angle T_{meas}\left(t, \varepsilon_s, f_m, \theta_{n1}\right)\right]^2 \end{aligned} \tag{3.5b}$$

in order to avoid the systematic phase error in the first band. To see how the repeatability error in the network analyzer measurements propagate through the nonlinear retrieval algorithm, we consider a uniform dielectric slab of thickness 457.2μm (18 mil) and dielectric constant of $2 + j0.05$. Next, we calculate the theoretical transmission coefficient according to (3.1), and multiply the results with the traces in Fig.3.3. Then, we feed the results to our retrieval algorithm. The obtained complex dielectric constant together with the obtained thickness are shown on the 3D plot in Fig.3.5(a), while Fig.3.5(b) shows the projection on the complex dielectric constant plane. The mean value for the retrieved dielectric constant is $2.11 + j0.059$, and that for the thickness is 422.9μm. Again, there is a biased shift in all retrieved values which is consistent with the positive phase shift observed in (247 – 325 GHz) band in Fig.3.4(b). Now, we turn our attention to the other sources of errors which are the sample roughness and inhomogeneous thickness profile. In order to understand the effect of these errors on the retrieved dielectric constant, we resort to numerical simulations. Basically, a 2D random rough layer is generated according to given correlation functions.

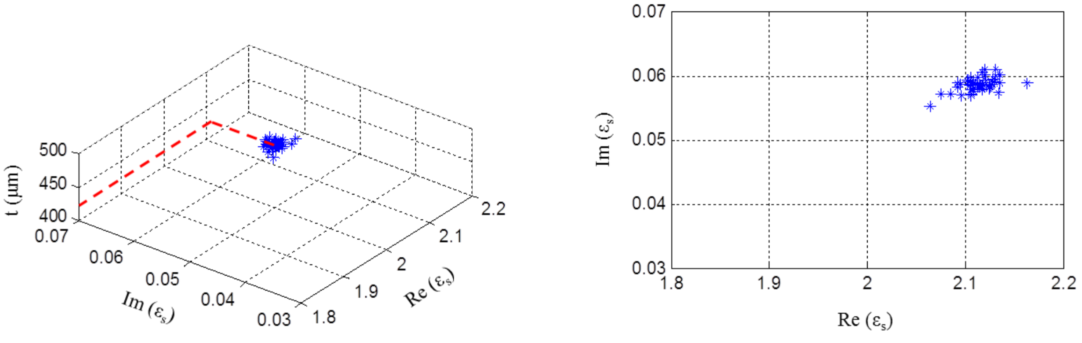

(a) (b)

Figure 3.5: Effect of network analyzer repeatability error on the retrieved complex dielectric constant and thickness. (a) 3D plot. (b) Projection on the complex dielectric constant value plot. The mean value of the dielectric constant is $2.11 + j0.059$, while the mean value for the thickness is $422.9\ \mu m$.

Then, the transmission coefficient through the rough slab is calculated using the Method of Moment (MoM) and fed back to our retrieval algorithm. For this simulation, the dielectric slab is assumed to have a nominal thickness of $t_{nom} = 457.2\mu$m and dielectric constant of $2 + j0.05$. The upper rough surface profile is generated according to a Gaussian probability density function (PDF) with zero mean and standard deviation of σ_{z1}. The surface correlation function is also assumed to be Gaussian with correlation length l_{c1}. The thickness profile is generated similarly with parameters σ_{z2}, l_{c2}, and mean value of $-t_{nom}$. We use the 2D MoM formulation presented in [100]. The random rough layers are adjusted to have a finite lateral extent of $80\lambda_m$ (λ_m is the free-space wavelength at the maximum frequency, 325 GHz), while the excitation is assumed to be Thoros wave with appropriate parameters [100]. Figure 3.6 shows the retrieved dielectric constant for three cases: (a) only surface roughness considered ($\sigma_{z1} = 5\%\, t_{nom}$, $\sigma_{z2} = 0$), (b) only thickness inhomogeneity considered ($\sigma_{z1} = 0\, t_{nom}$,$\sigma_{z1} = 10\%\, t_{nom}$), and (c) both considered ($\sigma_{z1} = 5\%\, t_{nom}$, $\sigma_{z1} = 10\%\, t_{nom}$). For all three cases, the correlation lengths are assumed to be: $l_{c1} = 5\lambda_m$ and $l_{c2} = 15\lambda_m$. We can immediately see that the surface roughness effect has minor effects compared to the thickness inhomogeneity. The effect on the real part of the relative dielectric constant is of the order of ±0.1, while the effect on imaginary part is ±0.05. Also, it can be inferred from case (b) that the retrieved complex values follow a symmetric straight line in the complex plane and, hence, simple averaging can help to predict the correct dielectric constant value. It should be mentioned here that although the height standard deviation values and correlation lengths used in the previous numerical simulations are not based on sample profile measurements, they are presented for two reasons. First, it is to examine the effects of surface roughness and thickness inhomogeneity of the sample, and second, to justify using simple averaging as an unbiased estimator of the true dielectric constant value. Other sources of measurement errors like sample misalignment have lower effect on the retrieved dielectric constant as explained in [89]. After identifying the main sources of errors in the measurements, we are ready to measure the desired samples. We start with a low resistivity 6-inch silicon wafer that is commonly used in microfabrication of sub-terahertz passive devices. The nominal thickness of the sample is $675 \pm 25\mu m$, while the resistivity is 20Ω-cm. The reason for this choice is because of the uniformity of the sample thickness. Furthermore, the dielectric constant for silicon wafer is already known [88], [101]. Using the proposed approach, the complex permittivity of thirteen independent sample positions (separated by 3mm as before) is measured. The nominal thickness of 500μm instead of 675μm is assumed initially in order to examine the ability of the algorithm to retrieve the correct sample thickness. Figure 3.7(a) shows retrieved complex dielectric constant, while Fig.3.7(b) shows the corresponding sample thickness. The measured average dielectric constant and the average thickness are found to be $11.41 + j0.34$, and 683.1μm respectively. The retrieved sample thickness agrees very well with the nominal thickness value. A comparison between the measured transmission

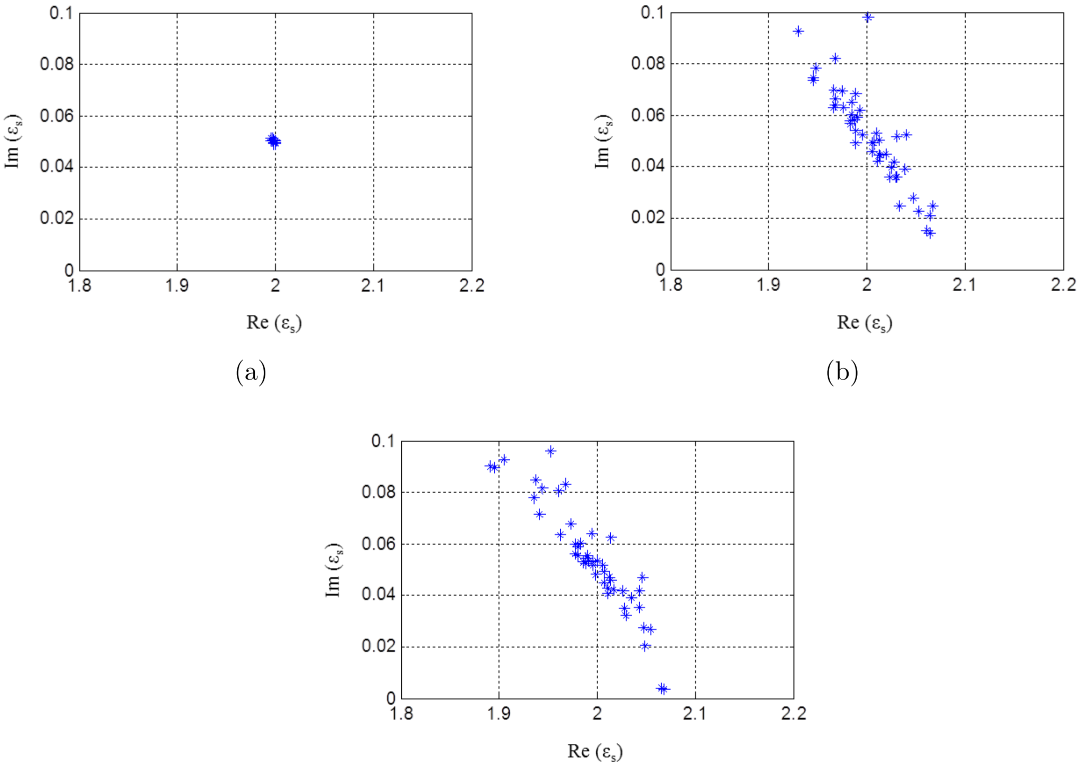

(a) (b)

(c)

Figure 3.6: Effect of surface roughness and thickness inhomogeneity of the sample on the retrieved dielectric constant. (a) Only surface roughness considered. (b) Only surface inhomogeneity considered, and (c) both effects considered.

coefficient and the theoretical one based on the values obtained from the retrieval algorithm is shown in Fig.3.8. Good agreements are observed for both the magnitude and phase except for some discrepancies at the (220 – 242.5 GHz) band which can be attributed to the network analyzer repeatability problem mentioned earlier. This figure also corroborates the assumption that the dielectric constant of the sample is almost independent of frequency across the entire frequency band of VNA operation. With confident in the measurement setup and the retrieval algorithm, dielectric measurements of different fabric samples are presented next. For each fabric material, three samples are prepared and for each sample, thirteen

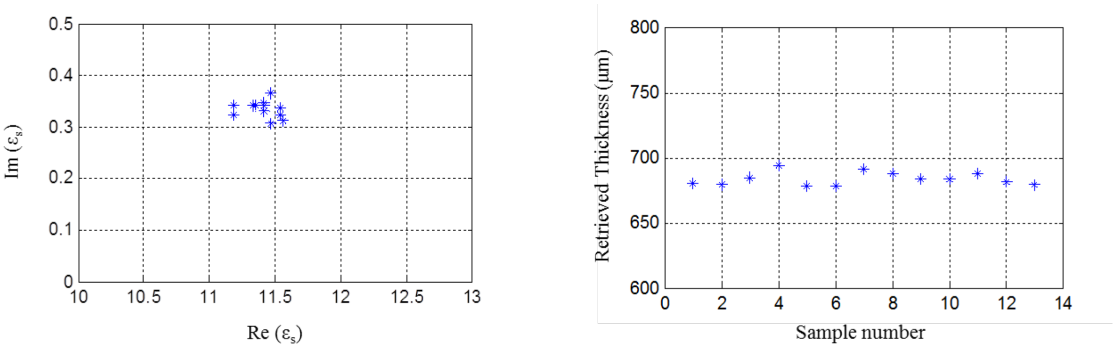

(a) (b)

Figure 3.7: (a) Retrieved dielectric constant values from 13 independent measurements of a 6-inch low-resistivity silicon wafer. (b) Retrieved sample thickness.

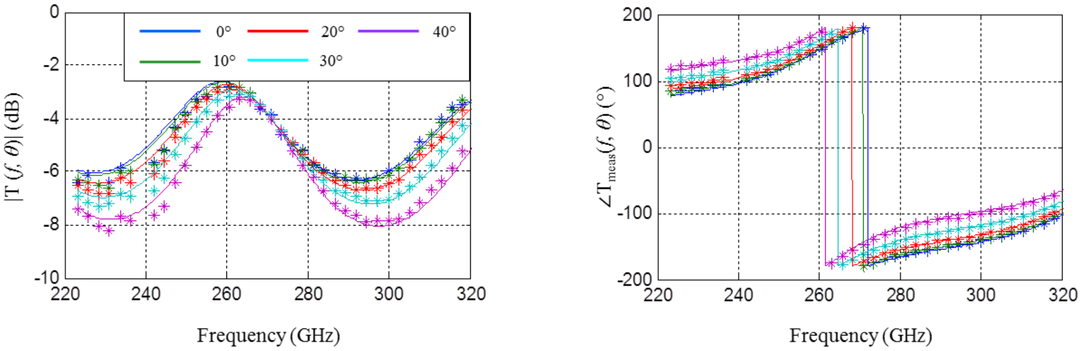

(a) (b)

Figure 3.8: Comparison of the measured transmission coefficient (indicated with * marks) and the theoretical one based on the values obtained from the retrieval algorithm (indicated with solid line) for one position of the 6-inch low-resistivity silicon wafer. (a) Magnitude. (b) Phase.

measurements are performed. As mentioned before, the initial guess for sample thickness is done by using a vernier while squeezing the sample as much as possible with hand. The fabric samples (wool, polyester, acrylic, and jeans) are also measured under wet conditions. This is done by soaking the material in water for some time and draining the sample before the measurement. Two issues are encountered in these measurements: 1) non-uniform moisture across the cloths due to the effect of gravitational force, and 2) moisture reduction as a function of time due to evaporation during the measurements (the measurement time is about 150 seconds per sample position). To alleviate these problems to some extent, the wet samples are prepared by letting the samples to dry for some period of time after soaking it in water and then ironing them to dry out unbounded portion of water. This created a more stable condition for the wet cloths. Since it was difficult to control the water content inside the sample, only one sample (instead of three) is considered in this case. Furthermore, five different measurements per sample, instead of thirteen, are taken in order to speed up the measurement process. Independent transmission measurements through the samples are obtained by 6 mm lateral movement of the sample (instead of 3 mm). Estimation of the water content inside the sample is done by comparing the sample weight before and after the measurements, with that of the dry sample. Upon performing the measurements, the transmission coefficient obtained for the acrylic and polyester samples were found to vary a lot from one point to the other, indicating highly inhomogeneous dielectric profile. Thus, these results are not reported here. Table 3.1 shows the measured dielectric constants of the dry and wet samples. Generally speaking, the dielectric constants of different dry fabrics are similar and around $2 + j0.05$; however, both wool and cow leather show higher losses. Also, the leather materials have lower variability (standard deviation) for the retrieved parameters which can be attributed to their uniform thickness profile. This is also observed for wool and jeans, but not for acrylic and polyester. It is also noticed that the dielectric loss tangent is substantially higher for the wet jeans and wet wool as the water is rather lossy material at these frequencies (the relative dielectric constant of pure water at 240 GHz is around $5.28 + j5.35$ [1]).

Table 3.1: Retrieved thickness and dielectric constant of fabric materials.

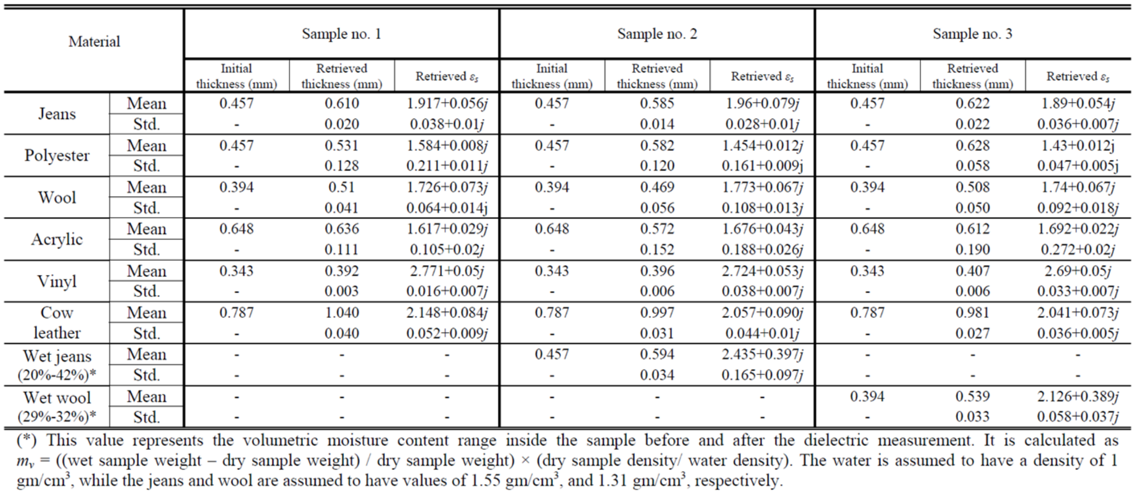

Material		Sample no. 1			Sample no. 2			Sample no. 3		
		Initial thickness (mm)	Retrieved thickness (mm)	Retrieved ε_s	Initial thickness (mm)	Retrieved thickness (mm)	Retrieved ε_s	Initial thickness (mm)	Retrieved thickness (mm)	Retrieved ε_s
Jeans	Mean	0.457	0.610	1.917+0.056*j*	0.457	0.585	1.96+0.079*j*	0.457	0.622	1.89+0.054*j*
	Std.	-	0.020	0.038+0.01*j*	-	0.014	0.028+0.01*j*	-	0.022	0.036+0.007*j*
Polyester	Mean	0.457	0.531	1.584+0.008*j*	0.457	0.582	1.454+0.012*j*	0.457	0.628	1.43+0.012j
	Std.	-	0.128	0.211+0.011*j*	-	0.120	0.161+0.009j	-	0.058	0.047+0.005j
Wool	Mean	0.394	0.51	1.726+0.073*j*	0.394	0.469	1.773+0.067*j*	0.394	0.508	1.74+0.067*j*
	Std.	-	0.041	0.064+0.014j	-	0.056	0.108+0.013*j*	-	0.050	0.092+0.018*j*
Acrylic	Mean	0.648	0.636	1.617+0.029*j*	0.648	0.572	1.676+0.043*j*	0.648	0.612	1.692+0.022*j*
	Std.	-	0.111	0.105+0.02*j*	-	0.152	0.188+0.026*j*	-	0.190	0.272+0.02*j*
Vinyl	Mean	0.343	0.392	2.771+0.05*j*	0.343	0.396	2.724+0.053*j*	0.343	0.407	2.69+0.05*j*
	Std.	-	0.003	0.016+0.007*j*	-	0.006	0.038+0.007*j*	-	0.006	0.033+0.007*j*
Cow leather	Mean	0.787	1.040	2.148+0.084*j*	0.787	0.997	2.057+0.090*j*	0.787	0.981	2.041+0.073*j*
	Std.	-	0.040	0.052+0.009*j*	-	0.031	0.044+0.01*j*	-	0.027	0.036+0.005*j*
Wet jeans (20%-42%)*	Mean	-	-	-	0.457	0.594	2.435+0.397*j*	-	-	-
	Std.	-	-	-	-	0.034	0.165+0.097*j*	-	-	-
Wet wool (29%-32%)*	Mean	-	-	-	-	-	-	0.394	0.539	2.126+0.389*j*
	Std.	-	-	-	-	-	-	-	0.033	0.058+0.037*j*

(*) This value represents the volumetric moisture content range inside the sample before and after the dielectric measurement. It is calculated as m_v = ((wet sample weight – dry sample weight) / dry sample weight) × (dry sample density/ water density). The water is assumed to have a density of 1 gm/cm^3, while the jeans and wool are assumed to have values of 1.55 gm/cm^3, and 1.31 gm/cm^3, respectively.

3.4 Measurement of Human Skin Dielectric Constant

Obviously in vivo dielectric constant of human skin cannot be measured using the procedure described before. For this purpose, another method based on reflection measurements is used. Simply, open ended waveguide at the output of one of the frequency extenders is used to measure the reflection coefficient from an exposed portion human body (fingers, hands, etc.). Such a procedure, however, requires very accurate 1-port calibration. This happens to be a major issue at this frequency band due to the repeatability problems associated with flange misalignment when different calibration standards are connected to the port [102], [103]. To solve this problem, we rely on the 1-port calibration procedure presented in [104]. It utilizes four standards: a flush short, two delay shorts with unspecified but different lengths (phases), and the open ended waveguide itself. This procedure, to a great deal, is immune to the errors associated with flange misalignment and load reflection uncertainty. Such procedure was demonstrated for (75 – 110 GHz) frequency band in [104] with the use of a modified W-band waveguide with large flange. The large flange was needed in order to

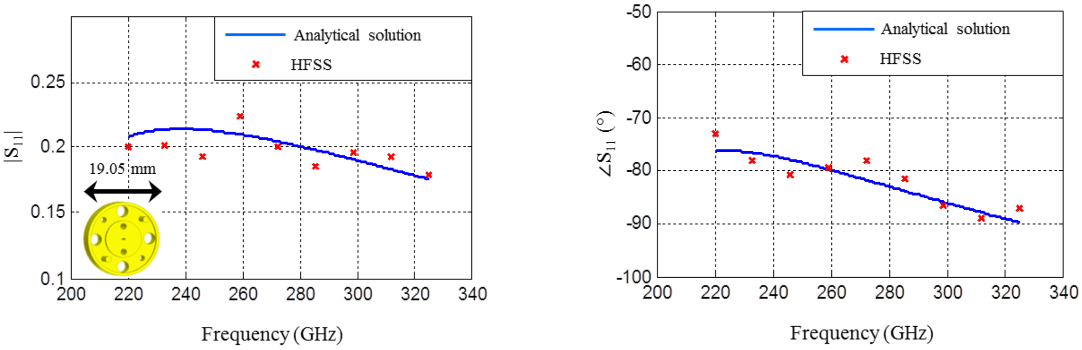

(a)

(b)

Figure 3.9: Comparison between theoretical reflection coefficient from a WR-3 waveguide radiating in an infinite dielectric half space (vaccum), and HFSS numerical solution for the actual flange: (a) Magnitude. (b) Phase.

compare the open-ended waveguide measurements with the theoretical solution of an open ended waveguide with an infinite metallic flange [105], [106]. For our case, the standard J-band flange is large enough for our purposes. This is justified in Fig.3.9 by comparing the analytical solution for the infinite metallic flange and HFSS simulation of the actual flange. It can be inferred from this figure that the J-band flange is large enough to be approximated by infinite metallic plane in so far as the open-ended waveguide is concerned. The small fluctuations of HFSS results can be attributed to the finite numerical accuracy of HFSS simulation as the simulation domain is electrically very large ($23.8\lambda \times 23.8\lambda \times 15\lambda$, at 325 GHz). It is worth mentioning that this simulation took several days to complete on a 15-node computer cluster. In summary, to perform the 1-port calibration, we used a flush short, two delay shorts of lengths 2.544mm, and 2.916mm available from OML V03CAL calibration kit and an open ended waveguide. We relied on the theoretical solution [106] of an open ended waveguide with an infinite flange to calculate the reflection coefficient of the open ended waveguide with finite size flange. Once the calibrated S_{11} measurements is accomplished , the dielectric constant of the sample under test can be obtained by comparing the measured reflection results with the theoretical reflection coefficient from an open ended waveguide terminated with infinite metallic flange in contact with a half-space dielectric material. Since the inverse problem is complex, the forward problem is solved for a fine grid of $\mathrm{Re}\left(\varepsilon_s\right)$ and $\mathrm{Im}\left(\varepsilon_s\right)$. The retrieved dielectric constant value will be the one that minimizes the following objective function:

$$OF_3\left(Re\left(\varepsilon_s\right), \mathrm{Im}\left(\varepsilon_s\right)\right) = \sum_{f_m=220\mathrm{GHz}}^{325\mathrm{GHz}} \left[\ln\left|R_{meas}\left(f_m\right)\right| - \ln\left|R_{th}\left(f_m\right)\right|\right]^2 + \left[\angle R_{meas}\left(f_m\right) - \angle R_{th}\left(f_m\right)\right]^2 \tag{3.6}$$

It should be mentioned here that the repeatability problem mentioned in Sec.3.3 for S_{21} measurements, is not observed for S_{11} measurements, hence, the sum in (3.6) can be carried over the entire frequency band.

A comparison between the measured calibrated reflection coefficient from the palm of a human hand and the theoretical one based the retrieved dielectric constant value of $\varepsilon_r = 3.94 + j2.82$ is shown in Fig.3.10. Some numerical artifacts can be observed in the calibrated response at certain discrete frequencies. This is attributed to the fact that the electrical length of one of the two offset shorts becomes equal to $\lambda/2$ at some frequencies. Such discrete frequencies can be eliminated from the sum in (3.6). None the less, the overall agreement between the measurement and the theoretical solution in Fig.3.10 is very good. To examine the range of variations of human dielectric skin, the dielectric measurement procedure is performed on three different individuals. For each individual, one measurement is taken from each of his fingers (total of ten samples) and three measurements are taken from the lower side of both hands near the wrist (total of six samples). The average retrieved

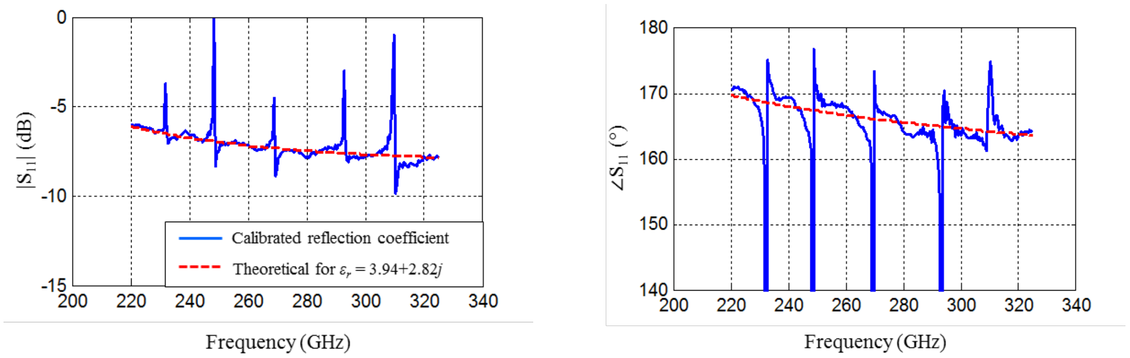

(a)

(b)

Figure 3.10: Comparison between calibrated reflection coefficient from a WR-3 waveguide terminated by the palm of a human hand, and the theoretical one based on the retrieved dielectric constant value of $\varepsilon_r = 3.94 + j2.82$.

dielectric constant values together with the standard deviation are given in Table 3.2. From the standard deviation of the measurements it is obvious that the dielectric constant can vary considerably from one spot to the other. Also, the dielectric constant can vary from one person to the other. However, an average number of about $2.8 + j2.4$ may be used for numerical simulation purposes at this frequency range. In [107], a four-term Cole-Cole expression was used to fit measured dielectric constant data up to 20 GHz for different human tissues and organs including wet and dry skin. If such expressions are used to extrapolate the data to 270 GHz, the resulting dielectric constant values will be $4.27+j2.76$, and $4.94+j3.7$, for dry and wet skin, respectively. This discrepancy suggests that such expressions should be revised for better accuracy at higher frequencies. It is worth mentioning here that skin depth at 270 GHz for a dielectric material with $\varepsilon_r = 2.8+j2.4$ can be calculated to be about 265μm. Thus, the electromagnetic wave will mostly “see” the human skin layer and not the underlying tissue. It is important at this point to mention that the reflection measurement procedure mentioned here is not highly sensitive for samples with high dielectric constant

Table 3.2: Retrieved dielectric constant of human skin.

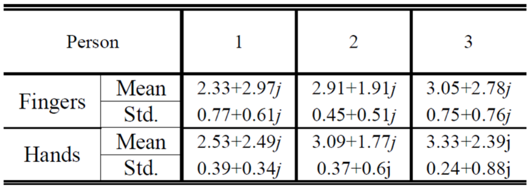

Person		1	2	3
Fingers	Mean	2.33+2.97j	2.91+1.91j	3.05+2.78j
	Std.	0.77+0.61j	0.45+0.51j	0.75+0.76j
Hands	Mean	2.53+2.49j	3.09+1.77j	3.33+2.39j
	Std.	0.39+0.34j	0.37+0.6j	0.24+0.88j

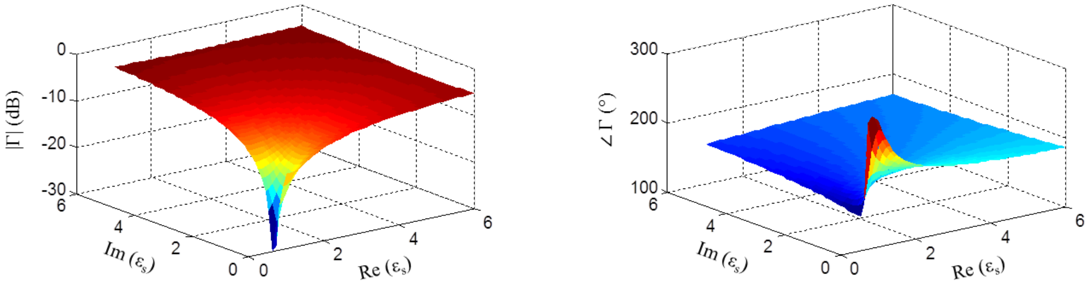

(a) (b)

Figure 3.11: Reflection coefficient from a WR-3 waveguide radiating in a semi-infinite dielectric half space versus the complex dielectric constant of the half space at 240 GHz

values. Figure 3.11 shows the theoretical magnitude and phase of the reflection coefficient from a WR-3 waveguide radiating in a semi-infinite half space dielectric medium versus the dielectric constant of the half space at 240 GHz. It can be observed that the reflection coefficient does not change much after $5 + j5$ rendering this method not useful for materials with dielectric constant outside such range. Finally, in order to appreciate the effect of clothing on the reflection coefficient from the human skin, we consider the simple case shown in Fig.3.12 where a comparison is made between the reflection coefficient from bare human skin and skin covered with a layer of jeans. It can easily be inferred from the figure that jeans layer can alter the “apparent” reflection coefficient of the skin layer significantly both in magnitude and phase.

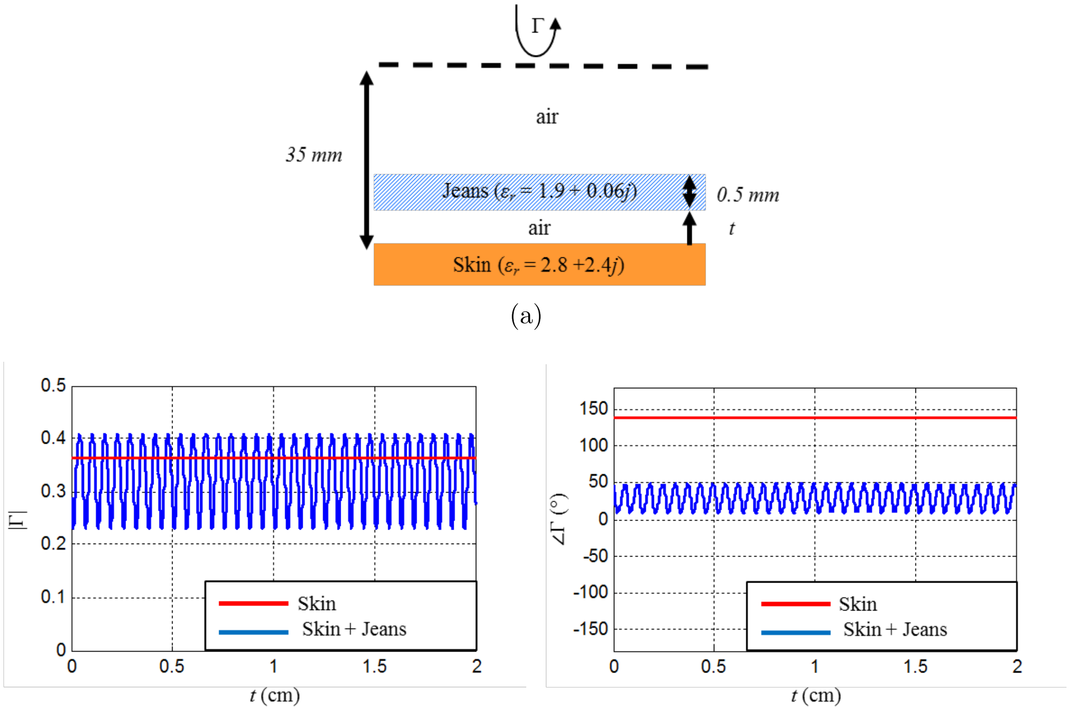

(a)

(b)

(c)

Figure 3.12: Reflection coefficient comparison as a function of the gap thickness (t) between the bare skin case, and a skin covered with a jeans layer of 0.5mm thickness.

3.5 Conclusion

A network-analyzer-based dielectric measurement system working at J-band is introduced. The main objective is to report accurate measurements of the dielectric permittivity of different materials important for concealed object detection scenarios. For this purpose, different fabric materials under dry and wet conditions as well as human skin are reported. For the fabric materials, a free-space transmission only measurement procedure is used. The developed retrieval algorithm has the advantage of estimating both the complex dielectric constant as well as the sample thickness. This is important for the fabric materials because they do not have a well-defined thickness. The main sources of the measurements uncertainty are identified to be the inhomogeneity of the sample thickness and the repeatability error of the network analyzer itself. It is shown that the dielectric constants of all the fabric materials considered are nearly the same under dry condition at the considered frequency band with relatively higher losses for the cow leather material. For moist fabrics, the imaginary part of the complex permittivity increases significantly since it is dominated by the losses of the contained water. For in vivo human skin dielectric measurement, a reflection measurement technique is used. A non-standard one-port calibration procedure is adapted to avoid issues associated with waveguide flange misalignment during calibration.

CHAPTER IV

Experimental Characterization of Polarimetric Radar Backscatter Response of Distributed Targets at Sub-THz Frequencies

4.1 Introduction

The phenomenology of radar return from manmade and natural targets is important for many sensing applications concerned beyond detection and ranging. In addition, the ability to model radar scenes is valuable when the performance of radars with different parameters for remote sensing is to be determined in a simulation environment. Unfortunately, the literature concerning the radar backscatter behavior of natural terrain at high MMW frequencies in general, and the 210-240 GHz frequency window in particular, are rather scarce. Previous efforts included wave attenuation and reflection studies through precipitation [48], [49], radar backscatter measurements of tree canopies and surfaces [50], [51] and snow covers [52]. Nevertheless, these studies were limited in terms of target types, angular ranges, and polarizations.

In this chapter, we report on an outdoor measurement campaign of different types of bare-surfaces and vegetation-covered surfaces conducted at 222 GHz. In Section 4.2, details of the newly constructed fully polarimetric instrumentation radar, operating at 222 GHz, and the calibration technique employed to correct for systematic errors in the system are described. This radar was used during the measurement campaign. In Section 4.3, details of the outdoor experimental setup, measurement procedure, and radar data processing are discussed. Both the ground truth and the measured polarimetric backscatter responses of the different surfaces are presented in Section 4.4. In Section 4.5, empirical models of the backscattering coefficients for both bare surfaces and vegetation-covered surfaces are presented. The material in this chapter can be found in [108]–[110].

4.2 Description of the Radar System and Calibration Procedure

Here, the newly constructed instrumentation radar operating at center frequency of 222 GHz is described. In addition, details of the calibration procedure used to correct for systematic errors in the radar system are presented. The radar system is bulit by Dr. Adib Nashashibi.

4.2.1 Newly Constructed Instrumentation Radar

The new instrumentation radar is a vector network analyzer (VNA)-based system that is also portable, wideband, and fully polarimetric. It is capable of transmitting 2-GHz wideband signal centered at 222 GHz. This radar system consists of an RF front-end unit, an HP8720D

VNA, and a polarization control switch box. The VNA generates an intermediate frequency (IF) at discrete frequency steps spanning the desired bandwidth. The RF front-end unit upconverts the IF signal to RF and transmits the signal using a dedicated transmit antenna. It also receives the reflected radar signal using a dedicated receive antenna, downconverts it to IF, and sends it back to the VNA for detection. The system can be operated manually or remotely via a computer. VNA-based instrumentation radars have been used for over two decades, and the principle of operation is well documented. Additional details on the stepped-frequency continuous-wave mode of operation of VNA-based instrumentation radars can be found in [1].

The block diagram of the newly constructed RF front-end unit is shown in Fig.4.1. It consists of two gaussian optics antennas by Millitech, Inc. The transmit antenna has 7.62 cm diameter lens, and its 3-dB beamwidth is 1.1^o. The receive antenna has 3.81 cm diameter lens, and its 3-dB beamwidth is 2.2^o. Using antennas with different beamwidths simplifies the alignment procedure. Both antennas enjoy side lobes that are at least 24 dB below the main lobe. Each antenna is equipped with two cascaded quarter-wave corrugated dielectric plates. The two plates are mechanically rotated around their axes to generate either vertical (V) or horizontal (H) polarizations [111], [112]. In effect, all four polarization combinations needed to measure the complex scattering matrix (VV, VH, HV, HH) can be generated. The two antennas are placed together and aligned to have parallel beams. At a distance 7m away from the antennas, the two corresponding beams completely merge, resulting in an effective system beamwidth of 1.1^o. Furthermore, the effective cross-polarization isolation of the system was measured to be 25 dB. The primary function of the RF front end is to upconvert/downconvert the modulated IF signals to/from RFs. It should be noted that, typically, the IFs f_{IF} used in the upconversion/downconversion steps are much lower than the desired RFs f_{RF}. The

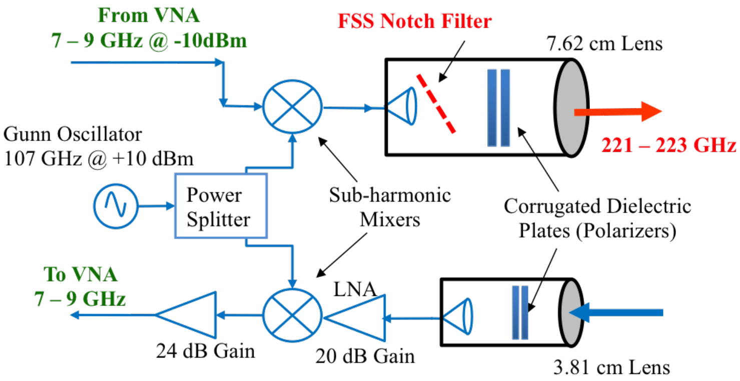

Figure 4.1: Block diagram of the RF-frontend of the 222 GHz instrumentation radar.

conventional approach in constructing the RF front end for systems operating below 100 GHz is to use fundamental mixers in both the upconversion and downconversion steps along with a local oscillator (LO) responsible for providing the mixers with the proper LO frequency, f_{LO}. The LO frequency in this case is usually selected to be close in value to that of the RF ($f_{RF} = f_{LO} + f_{IF}$). Fundamental mixers require substantial LO power and enjoy good conversion loss. In addition, substantial transmitted RF power is readily available by these mixers when used as upconverters. Typically, MMW LO units, whether they are stand-alone or phase-locked units, are Gunn-diode- based oscillators. At frequencies beyond 110 GHz, Gunn diodes with sufficient LO power generation capabilities do not exist. To date, both fundamental mixers and stand-alone LO sources are not commercially available for frequencies beyond 110 GHz. Subharmonic mixers present a reasonable alternative to fundamental mixers at frequencies beyond 110 GHz [113]. The input to the subharmonic mixer is an LO signal whose frequency is 1/2 the desired LO signal. In the subharmonic mixer, the second harmonic of the input LO signal is generated and mixed with the RF signal when the mixer is used as a downconverter (or the IF signal when the mixer is used as an upconverter). Recent advances in solid-state technologies have enabled the construction of a special type of subharmonic mixers based on antiparallel diodes architecture [113] on a single chip, thus ensuring minimal mismatch between the antiparallel diodes and excellent overall performance [114]. The advantage of the antiparallel design is that the second harmonic of the input LO signal is completely suppressed at both the LO and RF ports, allowing only for the mixed signal and its image to propagate. Proper built-in filters inside the LO and RF mixer ports ensure that RF signals do not leak into the LO path and the LO signal does not leak into the RF path [114]. This relatively old mixing concept has been perfected by a number of MMW manufacturers and is a viable tool for mixing at submillimeter frequencies.

The RF front end of the instrumentation radar uses subharmonic mixers for upconversion/downconversion, as shown in Fig.4.1. Virginia Diodes manufactured the two subharmonic mixers used in the system. The mixers are broadband mixers, each with a conversion loss of 8.5 dB single side band (SSB) and a noise temperature double side band (DSB) of 550K measured at room temperature. The LO signal is generated using a tunable Gunn diode source from Spacek Labs. Its frequency f_{LO} is set to 107 GHz, and it produced sufficient LO power of +10 dBm to drive the two subharmonic mixers. In addition, a 222-GHz LNA with 20 dB gain, 6-dB noise figure, and 0-dBm output 1-dB compression point donated by Northrop Grumman, is integrated in the receiver path. The IF f_{IF} is set between 7 and 9 GHz. As a result, the subharmonic mixer in the transmit path upconverts the IF signal to RF and generates the desired frequency band f_{RF1} ($f_{RF1} = 2f_{LO} + f_{IF}$) spanning between 221 and 223 GHz and its image band f_{RF2} ($f_{RF2} = 2f_{LO} - f_{IF}$) spanning between 205 and 207 GHz. Overall, the radar's receiver dynamic range is over 110 dB, and its transmit power is -13.5 dBm.

For proper radar operation, only f_{RF1} (221–223 GHz) should be allowed to transmit. Otherwise, the reflected signals due to f_{RF1} and f_{RF2} will be downconverted to the same IF, added

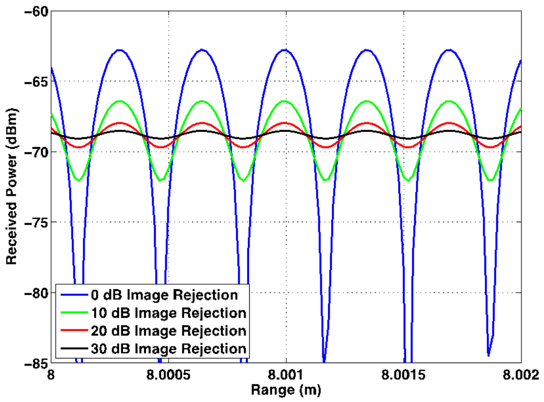

Figure 4.2: Numerically simulated range-induced interference effect of the received radar signal for different levels of rejection of the image signal f_{RF2}.

together coherently, and then detected by the VNA. In this case, the received signals, due to f_{RF1} and f_{RF1}, will have comparable amplitudes, but their phases, which are proportional to $(4\pi f_{RF1} \cdot r)$ and $(4\pi f_{RF2} \cdot r)$, respectively, will be different. The two signals may add constructively or destructively depending on the range to the target (r). Power level swings on the order of 20 dB can be observed from point targets due to slight changes (on the order of a fraction of a millimeter) in the target's range. System simulations of the RF front end in Fig.4.1 are performed, and the received power by the VNA is plotted as a function of range, as shown in Fig.4.2, for different suppression levels of the image signal f_{RF2}. These simulations demonstrate that, by suppressing the image signal by 25–30 dB, the interference pattern observed in the received power as a function of range can be eliminated. To suppress the image signal, a notch filter should be placed in the path of the RF signal. The standard approach is to place a waveguide-based filter right after the upconverting mixer. At frequencies beyond 200 GHz, waveguide-based filters become difficult to fabricate, and their insertion loss becomes prohibitively high. The alternative approach is to place a spatial filter inside the transmit antenna between the feed horn and the antenna lens, as depicted in

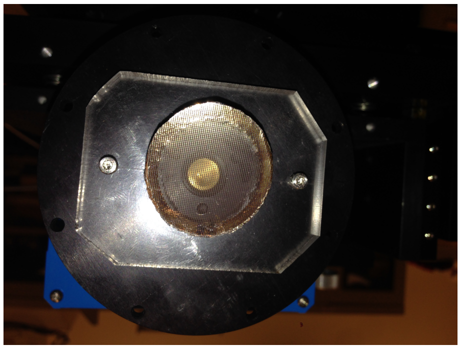

Figure 4.3: Photograph of the MEFSS notch filter [115] mounted in front of the feed horn of the transmit antenna.

Fig.4.1. A custom spatial notch filter was inserted in front of the transmit antenna feed to filter out the undesired image signal. The notch filter is a single-face, membrane-supported, miniaturized-element frequency selective surface (MEFSS) [115] that was specifically designed for this radar system at the University of Michigan Lurie Nanofabrication Facility. It was mounted on a fixture and placed in front of the feed horn, as shown in Fig.4.3. A total of 30 dB in image rejection was achieved (25 dB in image rejection due to the notch filter and 5 dB in LNA gain drop at f_{RF2}) and a low insertion loss of 0.5 dB over passband frequencies f_{RF1}. To ensure that the radar is stable, the LO temperature was thermally controlled to within 2^{o}C. Repeated experiments under different environmental conditions shows that a very stable operation in terms of the received power and phase from stationary point targets over long time periods can be achieved. The stability and phase-coherence property of the system ensure that fully polarimetric measurements (and imaging) can be performed accurately. A laser was mounted atop the narrowbeam transmit antenna and aligned with the transmitter main lobe direction. The laser is used to facilitate pointing of the radar system toward different targets.

4.2.2 Calibration Procedure

To remove the systematic errors in the radar system, including VNA errors, IF cable loss, and imperfections in RF components, external radar calibration is performed. The isolated antenna calibration technique (IACT) [116] is selected to calibrate the 222-GHz radar. In this technique, the antennas are assumed to have good cross-polarization isolation, and imbalances between the v-and h-received channels within the radar system can be calculated from the measured backscatter responses of a metallic sphere and any depolarizing point target (knowledge of its theoretical radar cross section (RCS) is not necessary). The selection of IACT over a more advanced singletarget calibration technique [117] for this radar is justified by the fact that the antennas of the 222-GHz radar enjoy a high crosspolarization isolation ($>$ 25 dB) and that strong cross-polarized return is expected from most targets at sub-THz frequencies (typically the cross-polarized backscattering coefficients of natural target are -4 to -12 dB below the copolarized backscattering coefficients [118]). Hence, the need for a more accurate calibration technique to improve the cross-polarization isolation beyond 25 dB is deemed unnecessary.

A polished 5.1 cm diameter metallic sphere was used to calibrate the radar along with a small SMA-to-BNC coaxial cable adapter (3.5 cm long) used as the depolarizing target. To verify the quality of calibration, a small metallic dihedral reflector was used as a test target. The dihedral was selected since its RCS is large compared with a sphere of similar size, and when tilted at 22.5^o, its cross-polarized return is equal to its copolarized return [119]. Furthermore, high-frequency expressions for its RCS are readily available [119]. A diagram depicting the tilted dihedral is shown in Fig.4.4. The polarimetric radar response of the dihedral is measured and calibrated using IACT and then compared with its theoretical polarimetric

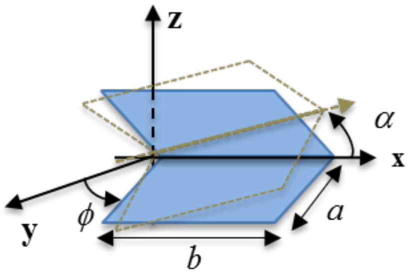

$$\bar{\bar{S}}(\phi=45^{\circ},\alpha)=\frac{\sqrt{2}ab}{\lambda}\begin{bmatrix} -\cos(2\alpha) & -\sin(2\alpha) \\ -\sin(2\alpha) & \cos(2\alpha) \end{bmatrix}$$

Figure 4.4: Rotated dihedral target and the corresponding scattering matrix [119]. Orientation angles ϕ (in $y-z$ plane) and α (in $x-z$ plane) are set to 45^o and 22.5^o respectively. Incident radar signal is along the y-axis. Dihedral dimensions were a = 0.974 cm and b = 1.943 cm.

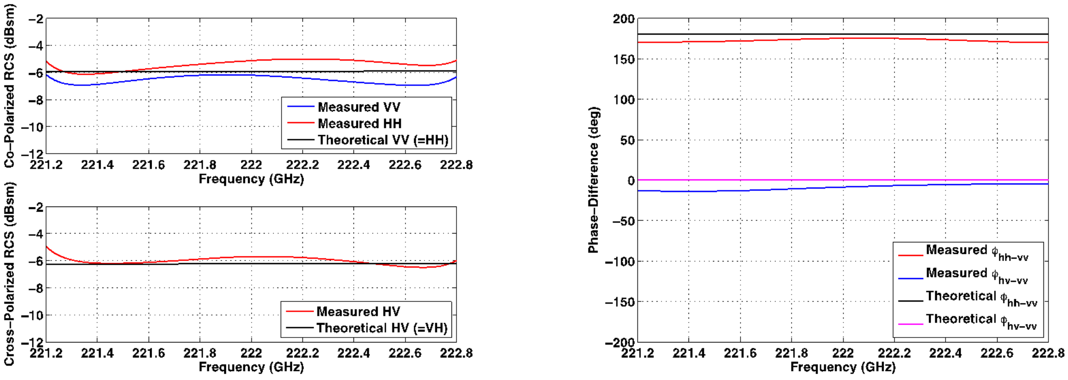

(a)

(b)

Figure 4.5: Comparison between calibrated radar response of tilted dihedral and theoretical calculations (a) RCS and (b) phase-difference.

RCS values. Excellent agreements between the theoretical RCS and the calibrated response are observed, as shown in Fig.4.5. Calibration accuracy, to within ±0.75 dB in magnitude and $\pm 10^o$ in phase, is achieved over the entire bandwidth.

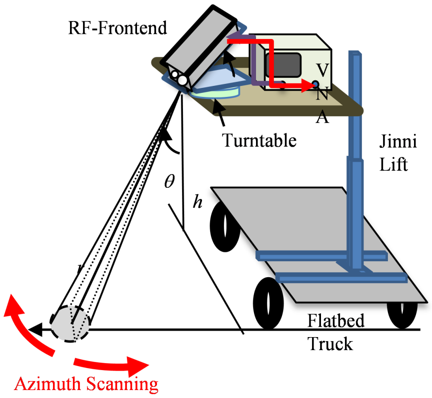

Figure 4.6: A sketch detailing the placement of the radar RF frontend, turntable, and vector network analyzer atop of a Jinni Lift which in turn is placed on a flatbed truck.

4.3 Outdoor Experimental Setup and Measurement Procedure

4.3.1 Experimental Setup

The radar RF front end is placed in an elevation-over-azimuth positioning system. Elevation positioning is manually adjusted to the desired incidence angle θ, whereas the azimuth positioning is accomplished using a computer controlled turntable. The entire data acquisition system, which includes the RF front end, the VNA, the polarization control switch box, and the elevation-over-azimuth positioning system, is mounted on a Jinni lift to allow for radar placement at the desired height above ground, as depicted in Fig.4.6. During outdoor measurements, the Jinni lift is placed on top of a flatbed truck to facilitate mobility between different natural targets.

4.3.2 Measurement Procedure

During outdoor radarmeasurements, the radar is oriented at a given incidence angle. Then, the computer-controlled turntable is used to move the radar spot at 1^o increments in azimuth (resulting in no spot overlaps) to generate statistically independent spatial samples. At least 100 spatial samples are collected for every incidence angle. The measured incidence angles θ spanned between 20^o and 75^0. The radar's height above ground is adjusted between measurements of different incidence angles in order to satisfy the far-field criteria of the radar system. For any given spot, the radar system cycles between the different polarizations combinations sequentially (VV, HH, VH).

4.3.3 Data Processing

As aforementioned, the new radar system is a coherent system. Hence, the complex scattering matrix of a target (including both magnitude and phase) can be accurately measured. However, in outdoor settings where the target and/or the radar platform may be moving under the influence of wind, the coherence between different polarizations cannot be assured. Note that the VNA frequency sweep takes about 200 ms to complete for each polarization (in addition to the time it takes to move the data from the VNA to the computer); thus, at 222 GHz, where the wavelength is only 1.35 mm, it takes only a fraction of a millimeter in movement during measurements to destroy the phase coherence between the different polarizations. Hence, during outdoor measurements, only the backscattering coefficients of different targets are considered. Software gating (used to range gate the data) is applied to the measured data to isolate the radar backscatter response of the target from other nearby targets. The radar data are processed by first performing external calibration on the gated

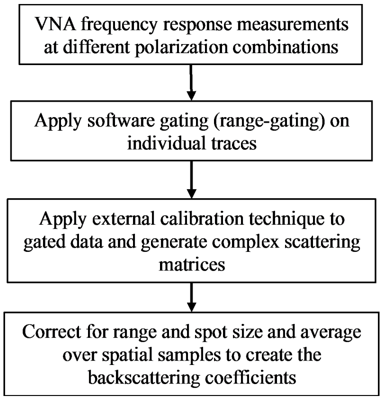

Figure 4.7: Flow chart describing the steps used in processing the radar data.

data to correct for losses in the radar system. Then, the backscattering coefficients σ^0_{pq} (with $p, q = v$ or h polarizations) of the target at any given incidence angle are calculated by averaging the calibrated received power at the center frequency (which are, in turn, derived from the magnitudes of the complex scattering matrices) over all spatial samples and accounting for the radar's spot size on the target [1], [120]. A simplified flowchart describing the data processing steps is shown in Fig.4.7.

4.4 Experimental Observations

The outdoor radar measurements were performed on a number of distributed targets, which can be categorized into two broad categories: bare surfaces and vegetation-covered surfaces. Each category is examined separately in the following.

4.4.1 Bare Surfaces

The bare surfaces that are considered in this study are all dry surfaces. They are as follows: 1) New Asphalt; 2) Weathered Asphalt; 3) Concrete; 4) Dirt; and 5) Brick Wall. A detailed description of these surfaces is provided first, followed by the discussion of the measured radar return.

Asphalt is a mixture of bitumen, air, and aggregates. Bitumen is the hydrocarbon material used to bind the aggregates together. The aggregates constitute between 75% and 85% of the asphalt surface by volume, and they are normally a mix of sand, gravel, and crushed stone, with the bulk of the aggregates size greater than 4.36 mm and smaller than 12.7 mm. Heavy rollers are used during the final construction step of a new asphalt surface to ensure that the new surface is flat. The high viscosity of bitumen and the heterogeneous nature of the aggregates (in size) result in the new asphalt surface with some aggregates flushed with the new surface, whereas others are slightly submerged under, as depicted in Fig.4.8. The impact is that the new asphalt surface may not be "electrically smooth" when compared with the radar's wavelength of 1.35 mm. Adverse environmental conditions over time cause cracks in asphalt and erosion of the topmost layer of aggregates. The result is a rougher air–asphalt interface. To measure the surface roughness of the new and weathered asphalt surfaces, a layer of Play-Doh was laid over the asphalt surface to create an imprint of the asphalt–air interface on the Play-Doh. The thin layer of Play-Doh was first dried using an oven before its surface roughness profile was measured in laboratory setting using the LEXT OLS4000 Laser Confocal Microscope. The surface was mapped in 2.5μm steps in azimuth and at 20μm vertical resolution. Roughness statistical parameters of the different surfaces are summarized in Table 4.1. No measurements of the effective dielectric constant ε_1^{as} of the

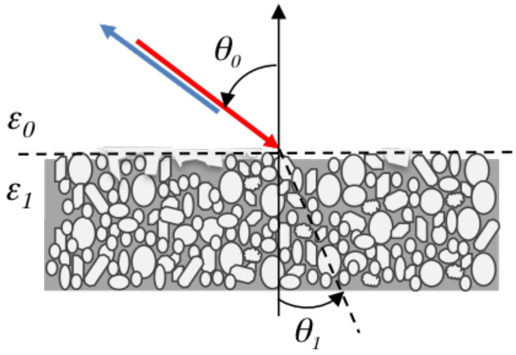

Figure 4.8: Depiction of scattering aggregates occupying the lower half-space.

Table 4.1: Roughness statistical parameters for the measured bare surfaces.

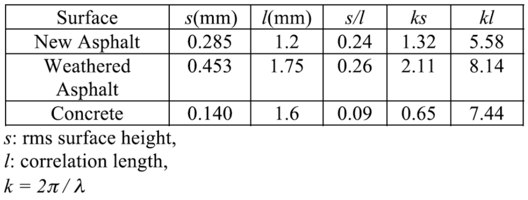

Surface	s(mm)	l(mm)	s/l	ks	kl
New Asphalt	0.285	1.2	0.24	1.32	5.58
Weathered Asphalt	0.453	1.75	0.26	2.11	8.14
Concrete	0.140	1.6	0.09	0.65	7.44

s: rms surface height,
l: correlation length,
$k = 2\pi / \lambda$

asphalt surfaces were performed at 222 GHz, and none is reported in the open literature at this frequency. However, it was measured at 94 GHz and was found to be $\varepsilon_1^{as} = 3.18$ [121].

In the case of concrete, water is added to cement to form a cement paste, which, in turn, is mixed with solid aggregates that act as a filler. The solid aggregates occupy between 60% and 75% in volume and include both coarse particles (gravel and crushed stones) and fine particles (sand). The cement paste (acts as binding agent) coats the aggregates completely and fills the gaps in between. The flowing consistency of freshly made and poured concrete mixture permits the creation of a very smooth air–concrete interface before it completely dries out. Surface profiles of the dry Concrete surface were collected according to the aforementioned procedure, and its roughness statistical parameters are summarized in Table 4.1. The closest frequency to 222 GHz at which the effective dielectric constant ε_1^{cn} of dry concrete was measured is 94 GHz [122]. It was found to be $\varepsilon_1^{cn} = 4.2$.

Dirt Surface Brick Wall

Figure 4.9: Close-up views of the measured Dirt surface and Brick Wall.

The Dirt surface consists of a loose mixture of common sand and gravel (no binding agent). Although it is initially compacted during construction, the surface becomes “electrically” quite rough over time, as shown in Fig.4.9. Although no measurements of the effective dielectric constant of dirt were performed at 222 GHz, earlier reported efforts at microwave frequencies indicate that the effective dielectric constant of dry soil is independent of frequency and varies between 2.5 and 3.5 depending on its density (compactness) [1]. The Brick Wall consists of fire-hardened bricks that are made of claybearing soil, sand, and lime. The surfaces of individual bricks are relatively smooth. Mortar is used between the individual bricks during wall construction, resulting in horizontal and vertical groves of varying lengths, as shown in Fig.4.9. The brick dimensions (relevant to the wall surface) are 22.5 cm × 5.5 cm, and the width of the mortar in between the bricks is 1.5 cm. Although no measurements of the effective dielectric constant of brick ε_1^{br} were reported at MMW frequencies, it is estimated that its value is $\varepsilon_1^{br} \approx 4.0$ since the effective dielectric constant of the solids in soil is reportedly 4 [1]. No surface profiles were collected for the Dirt and Brick Wall surfaces.

The measured vv- and vh-polarized backscattering coefficients (σ^0_{vv} and σ^0_{vh}, respectively) of the five bare surfaces are plotted as a function of the incidence angle in Fig.4.10. The two asphalt surfaces along with the dirt surface have essentially the same σ^0_{vv} and σ^0_{vh} responses, whereas the brick wall and the concrete surface have lower backscattering coefficients than

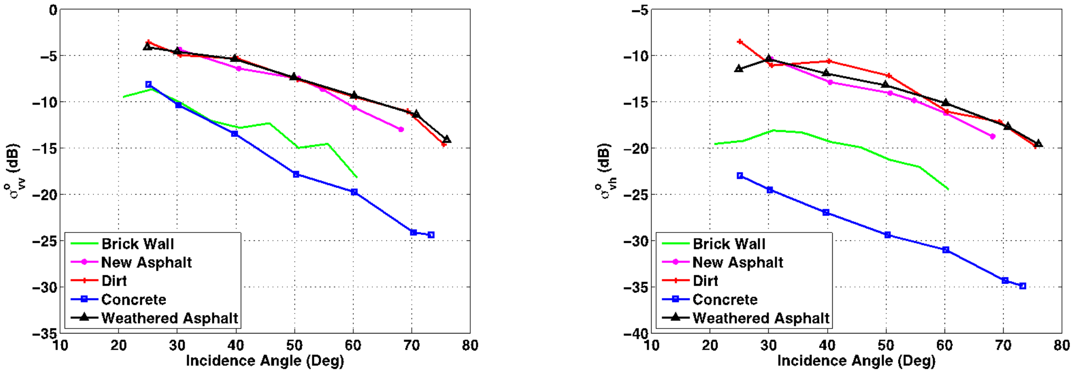

(a) (b)

Figure 4.10: Angular responses of measured (a) σ^0_{vv} and (b) σ^0_{vh} for all bare surfaces.

the first group. The copolarization ratio $p = \sigma^0_{hh}/\sigma^0_{vv}$ of the measured bare surfaces is plotted in Fig.4.11(a). It should be noted that, when $p < 0$ dB, it indicates that $\sigma^0_{hh} < \sigma^0_{vv}$. It is apparent from the figure that the separation between σ^0_{vv} and σ^0_{hh} increases as the incidence angle is increased for the asphalt and concrete surfaces. This suggests that use of the vv-polarization combination, as opposed to the hh-polarization, is preferred if surface detection is required in a given radar application. The depolarization ratio $\chi = 2\sigma^0_{vh}/\left(\sigma^0_{vv} + \sigma^0_{hh}\right)$ of the measured bare surfaces is plotted in Fig.4.11(b) as a function of the incidence angle. Strong depolarization is observed for all surfaces, with a ceiling level of -4 dB being observed. For the asphalt and dirt surfaces, the value of χ appears to be insensitive to the incidence angle. However, the response is quite different for the concrete and brick surfaces, where depolarization increases with incidence angle. This can be attributed to the fact that $\sigma^0_{hh} \ll \sigma^0_{vv}$ for these surfaces at high incidence angles.

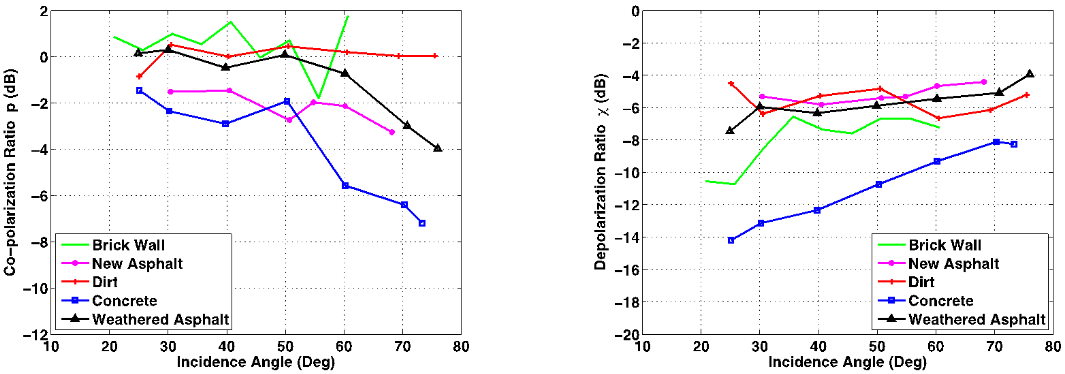

(a) (b)

Figure 4.11: Angular responses of measured (a) co-polarized ratio (p) and (b) depolarization ratio (χ) for all bare surfaces.

4.4.2 Vegetation-Covered Surfaces

Five different vegetation-covered surfaces were measured. The surfaces are as follows: 1) Short Grass #1; 2) Short Grass #2; 3) Short Grass #3; 4) Soybean; and 5) Tall (mixed) Grass. Short Grass #1 is a mixed-species grass field consisting of broad-leaf and thin blade-leaf plants. The grass is dense and completely covers the underlying soil surface. Short Grass #2 and Short Grass #3 are uniform-thickness grass fields of single grass species (thin blade leaves) completely covering the underlying soil surface. The Soybean-covered surface was measured during the growth period of the soybean plants. The soybean plants have broad leaves raised above soil. Plant density was 15 plants/m^2, and the mean main stem thickness was 0.5 cm. Tall (mixed) Grass is a field of multi-species grasses and different stand-alone weed-type plants. The field is spatially heterogeneous, with the different plants growing wildly, resulting in a vegetation layer with varying thickness and density. Photographs of selected surfaces are shown in Fig.4.12, and summary of additional ground truth data is listed in Table 4.2. The measured vv- and vh-polarized backscattering coefficients (σ^0_{vv} and


Short Grass#1 Tall (mixed) Grass

Figure 4.12: Photographic pictures of Short Grass #1 and Tall (mixed) Grass surfaces.

Table 4.2: Ground truth data of measured vegetation-covered surfaces.

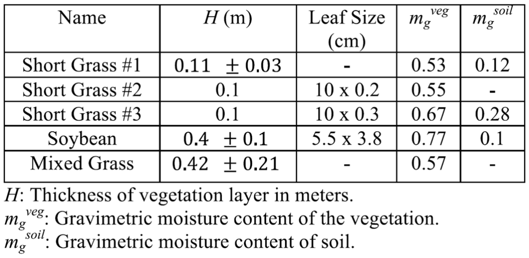

Name	H (m)	Leaf Size (cm)	m_g^{veg}	m_g^{soil}
Short Grass #1	0.11 ± 0.03	-	0.53	0.12
Short Grass #2	0.1	10 x 0.2	0.55	-
Short Grass #3	0.1	10 x 0.3	0.67	0.28
Soybean	0.4 ± 0.1	5.5 x 3.8	0.77	0.1
Mixed Grass	0.42 ± 0.21	-	0.57	-

H: Thickness of vegetation layer in meters.
m_g^{veg}: Gravimetric moisture content of the vegetation.
m_g^{soil}: Gravimetric moisture content of soil.

σ^0_{vh}, respectively) of the five vegetation-covered surfaces are plotted as a function of incidence angle in Fig.4.13. Although the vegetation-covered surfaces have significant differences in their physical properties, the measured backscattering coefficients of all surfaces span a narrow range of values, as shown in Fig.4.13. In addition, no substantial angular dependence is observed. The copolarization ratio p varies between ± 1 dB around a mean value of 0 dB, as shown in Fig.4.14(a), which indicates that both σ^0_{vv} and σ^0_{hh} are essentially the same for these surfaces ($\sigma^0_{vv} \approx \sigma^0_{hh}$). In addition, the depolarization ratio χ varies between ± 2 dB around a mean value of -9 dB with no apparent dependence on the incidence angle, as shown in Fig.4.14(b). Accordingly, cross-polarized return can be related to the copolarized return using the approximate relationship: $\sigma^0_{vh} \approx 0.125\sigma^0_{vv}$.

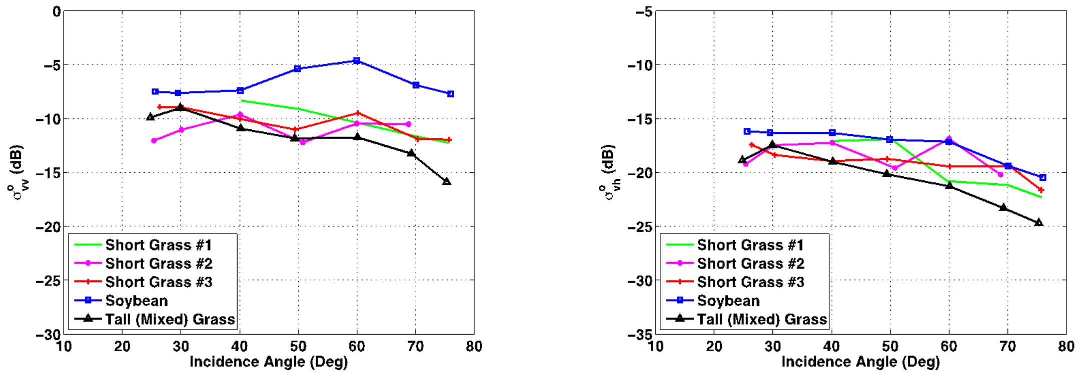

(a) (b)

Figure 4.13: Angular responses of measured (a) σ^0_{vv} and (b) σ^0_{vh} for all vegetation-covered surfaces.

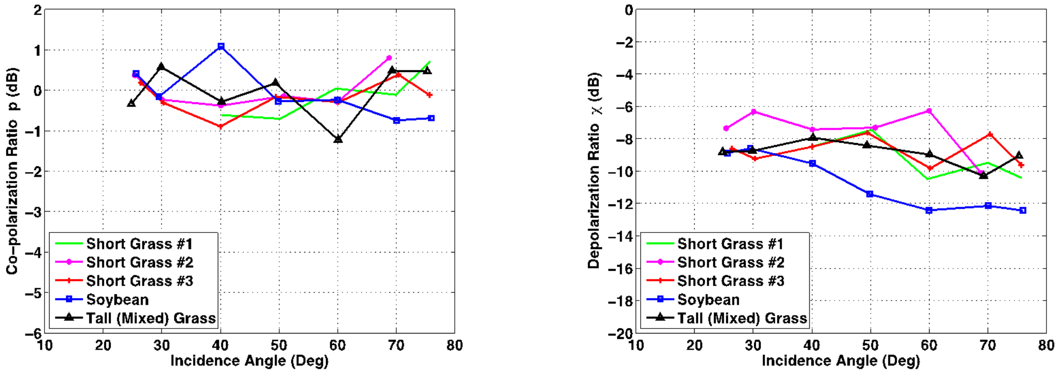

(a) (b)

Figure 4.14: Angular responses of measured (a) co-polarized ratio (p) and (b) depolarization ratio (χ) (for all vegetation-covered surfaces.

4.5 Emperical Backscatter Models

4.5.1 Bare Surfaces

There has been significant effort over the past two decades to study the phenomenology of radar return from bare surfaces, such as dry soil [118], [123], asphalt [121], [122], and dry sand [124], [125], at lower MMW frequencies (< 100 GHz). These studies have shown that the backscatter response of these surfaces is due to both surface scattering and volume scattering. Surface scattering is a function of surface roughness (characterized by its statistical parameters such as rms height and correlation length), radar frequency, incidence angle, and the effective permittivity of the material underneath the surface. Volume scattering, on the other hand, is a function of surface roughness statistics and its effective permittivity, subsurface particle size, dielectric constant, volume fraction, spatial particle distributions, radar frequency, and incidence angle. At sub-THz frequencies, the subsurface particles, such as sand particles, pebbles, and vegetation debris, are substantial fractions of the radar's wavelength, resulting in substantial volume scattering that may not be ignored. To first-order approximation, the total backscattering coefficient, σ^{0t}, can be expressed as studies

$$\sigma^{0t}_{mn} = \sigma^{0v}_{mn} + \sigma^{0s}_{mn}, \quad m, n = v \, or \, h \tag{4.1}$$

where σ^{0v}_{mn} and σ^{0s}_{mn} refer to volume and surface scattering contributions to the total backscattering coefficient, respectively. Roughness statistics of the bare surfaces (listed in Table 3.1) that were measured using the 222-GHz radar suggest that surface scattering from these surfaces may be substantial and cannot be ignored. The measured σ^0_{vv} and σ^0_{vh} of Dirt and Weathered Asphalt, representing the roughest surfaces, and Concrete, representing the smoothest surface, are compared with the backscattered response from three different models in Fig.4.15. The MMW surface model in Fig.4.15 refers to the semi-empirical surface scattering model that was developed in [123] using measured polarimetric MMW radar data of wet soil. The MMW surface model needs as inputs the roughness parameter ks, the effective permittivity of the surface ε_1, and the incidence angle θ_o. The model is described by the

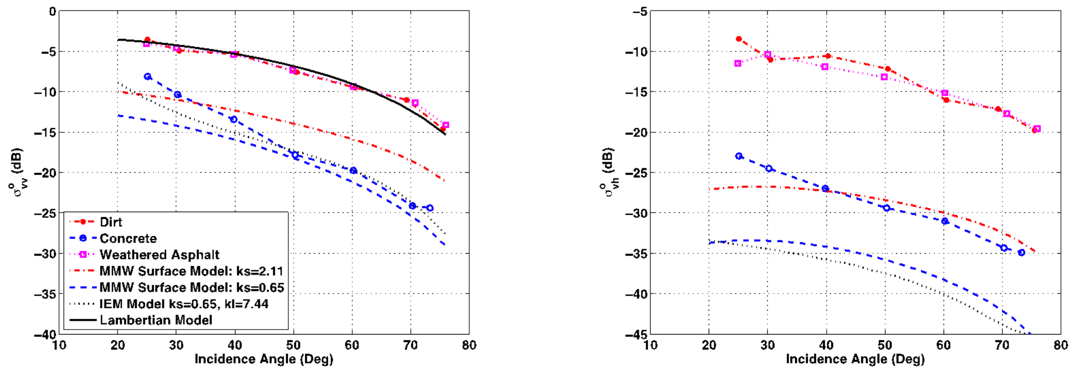

(a) (b)

Figure 4.15: Comparison between the measured backscattering coefficients and predictions by selected set of surface scattering models in case of (a) σ^{0}_{vv} and (b) σ^{0}_{vh}.

following equations:

$$
\begin{aligned}
\sigma^{0s}_{vv} &= g\frac{\cos^{\gamma}\theta_o}{\sqrt{p}}\left[\mathit{\Gamma}_v\left(\theta_o\right)+\mathit{\Gamma}_h\left(\theta_o\right)\right]\\
\sigma^{0s}_{hh} &= p\sigma^{0s}_{vv}\\
\sigma^{0s}_{vh} &= q\sigma^{0s}_{vv}\\
q &= 0.23\sqrt{\mathit{\Gamma}_v\left(0\right)}\left[1-e^{-0.5ks\sin\theta_o}\right]\\
p &= \left[1-\left(\frac{2\theta_o}{\pi}\right)^{1/3\mathit{\Gamma}_v\left(\theta_o\right)}e^{-0.4ks}\right]\\
g &= 2.2\left[1-e^{-0.2ks}\right]\\
\gamma &= 3.5+\frac{1}{\pi}\tan^{-1}\left[10\left(1.65-ks\right)\right]
\end{aligned}
\tag{4.2}
$$

where $\mathit{\Gamma}_v\left(\theta_o\right)$ and $\mathit{\Gamma}_h\left(\theta_o\right)$ are the Fresnel reflectivities at incidence angle θ_o for both v and h polarizations, respectively.

The IEM model refers to the integral equation surface scattering model [126]. It requires

ks, kl, ε_1, and θ_o for input. Its region of validity is restricted by the following constraints: $s/l \leq 0.25$ and $ks < 1$ [126]. In view of the surface roughness parameters in Table 4.1, the IEM model is applicable to the Concrete surface only. Both the MMW surface model and the IEM model match reasonably well with the measured σ^0_{vv} of the Concrete surface, particularly at high incidence angles, as shown in Fig.4.15(a). However, they do underestimate the measured σ^0_{vh} of Concrete, as shown in Fig.4.15(b). The difference between these surface models and the measured σ^0_{vh} of Concrete can be attributed to volume scattering, which has not been accounted for yet. The MMW surface model also significantly underestimates the measured σ^0_{vv} and σ^0_{vh} of Weathered Asphalt, as shown in Fig.4.15. This is expected since asphalt (and dirt, too) represents heterogeneous media with substantial volume scattering contribution that has not been accounted for in the MMW surface model [123].

One interesting observation of the measured σ^0_{vv} of the roughest surfaces (namely, the Dirt and Weathered Asphalt surfaces) is that its angular dependence closely matches that of a Lambertian surface [1], whose backscattering coefficient is given by $\sigma^0 = K\left(\cos\theta_o\right)^2$, where K is a constant that depends on the surface. The Lambertian model is based on Lambert's law for optics, where surface reradiation from a very rough surface is in accordance with a cosine law [1]. Setting $K = 0.5$ results in an excellent match with the measured σ^0_{vv} of the Dirt and Weathered Asphalt surfaces, as shown in Fig.4.15(a). The Lambertian model represents here an upper limit on the value of σ^0_{vv} that can be observed for bare surfaces.

Two semi-empirical volume scattering models were developed at MMW frequencies for asphalt [121] and dry sand [125]. The two models were based on the mathematical formulation resulting from the iterative solution of the vector radiative transfer equation [121] of a half-space random medium, as depicted in Fig.4.8. The expressions for the backscattering coefficients for the model reported in [121] are

$$\sigma_{mn}^{0v} = 4\pi \cos\theta_o \left|t_{n01}\right|^2 \left|t_{m10}\right|^2 \frac{p_{mn}}{2\kappa} \tag{4.3}$$

where subscripts m and n refer to v or h polarizations, t_{n01} is the field transmission coefficient from medium 0 to medium 1, p_{mn} is the mn element of the phase matrix of the scattering medium below the air–medium interface, and κ is the extinction rate through the medium. It was shown that p_{mn} for a given surface are independent of the incidence angle [121] and that $p_{vv} = p_{hh}$ and $p_{vh} = p_{hv}$ due to reciprocity [121]. The ratio $^{p_{mn}}/_{\kappa}$ is analytically unknown and is determined by fitting the model to measured data at a single incidence angle. The expressions for the backscattering coefficients for the model reported in [125] are

$$\sigma_{mn}^{0v} = 4\pi \frac{\varepsilon_0}{\varepsilon_1} \frac{\cos^2\theta_o}{\cos\theta_1} \left|t_{n01}\right|^2 \left|t_{m10}\right|^2 q_{mm} \tag{4.4}$$

Here, q_{mm} implicitly represents the ratio between the mn element of the phase matrix and the extinction rate. It was shown in [125] that q_{mm} are independent of the incidence angle and that $q_{vv} = q_{hh}$ and $q_{vh} = q_{hv}$ due to reciprocity [125]. Similar to the previous model, q_{mn} is determined by fitting the model to the measured data at a single incidence angle. The two models are fitted to the measured data at $\theta_o = 25^o$ for the Weathered Asphalt surface, as shown in Fig.4.16 (with surface scattering contribution being ignored for now). It is clear from the figure that the volume scattering model in (4.3) [121] fails to predict the angular dependence of the measured data, whereas the model in (4.4) [125] closely matches the data for both Weathered Asphalt and Dirt surfaces.

Next, we propose a semi-empirical hybrid model for predicting the total backscattering coefficients of bare surfaces at MMW frequencies. In this model, the backscattering coefficient

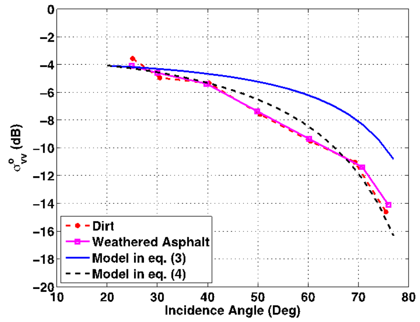

Figure 4.16: Comparison between the measured backscattering coefficients and selected set of semi-empirical volume scattering models.

of a bare surface is the sum of the backscattering coefficients due to surface scattering and volume scattering, as stated in (4.1). The surface scattering component is calculated using the MMW surface model in (4.2) [123], and the volume scattering component is calculated using the MMW volume model in (4.4) [125]. The surface scattering component can be calculated once ks and ε_1 are known for the surface. The volume scattering component needs the value of q_{mn} so it may be calculated properly. The value of q_{mn} depends on the particular random medium beneath the surface, and its value is not readily available. However, it can be estimated for the measured surfaces at hand by fitting the proposed hybrid model to the measured data at one incidence angle. This approach was applied to the bare surfaces reported in this study with the model being fitted to the measured data at incidence angle $\theta_o = 40^o$. The resulting q_{mn} values for the different surfaces are listed in Table 4.3, and the proposed model predictions are compared with the measured backscattering coefficients in Fig.4.17. Very good agreement is observed between the measured data and the proposed empirical model.

Table 4.3: Volume scattering model coefficients in (4.4) for the measured bare surfaces.

Bare Surface Type	q_{vv} $(= q_{hh})$	q_{vh} $(= q_{hv})$
New Asphalt	0.080	0.025
Weathered Asphalt	0.104	0.030
Dirt	0.067	0.022
Concrete	0.007	0.001

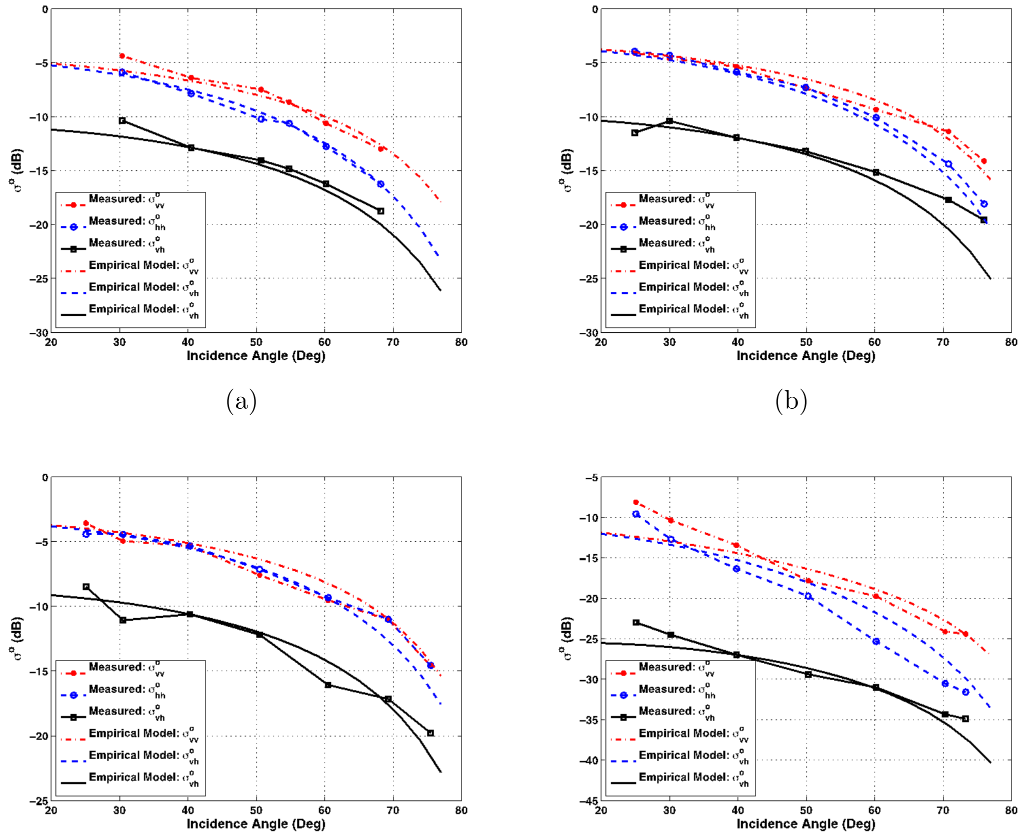

(a) (b)

(c) (d)

Figure 4.17: Comparison between measured backscattering coefficients and the semi-empirical hybrid model predictions for (a) New Asphalt, (b) Weathered Asphalt, (c) Dirt, and (d) Concrete surfaces.

4.5.2 Vegetation-Covered Surfaces

Unlike the case of bare surfaces, the measured backscattering coefficients of the vegetation-covered surfaces had shown either no angular dependence or weak dependence on the incidence angle, as observed in Fig.4.13. One possible modeling approach is to set $\sigma^0_{mn} = K_{mn}$, where K_{mn} is a constant dependent on the vegetation. However, this model is unrealistic since, as the incidence angle approaches grazing incidence (i.e., 90^o), the backscattering coefficients from these surfaces are expected to diminish.

It should be noted that the vegetation-covered surfaces are tenuous random media with very small fractional volumes. As such, the effective permittivity of the foliage layer ε_1 is expected to be close to that of air, namely, around 1. Furthermore, due to strong scattering from leaves and loss due to both absorption and scattering, the radar return from the soil underneath the foliage layer is expected to be insignificant at 222 GHz. Hence, the soil may be ignored, and the foliage layer may be considered as half-space medium. Since $\varepsilon_1 \approx 1$ for the foliage layer, then it can be shown that the two semi-empirical volume scattering models in [121] and [125] [reproduced in (4.3) and (4.4)] become indistinguishable and simplify to the following expression $\sigma^0_{mn} = K_{mn} \cos\theta_o$. Some of the measured data show $\cos\theta_o$ dependence, whereas others do have weaker dependence. Accordingly, we propose the following empirical model for vegetation-covered surfaces:

$$\begin{aligned}
\sigma^0_{vv} &= 0.12\,(\cos\theta_o)^x \\
\sigma^0_{hh} &= \sigma^0_{vv} \\
\sigma^0_{vh} &= 0.125\sigma^0_{vv} \qquad (4.5)
\end{aligned}$$

with $0 < x \leq 1$. The proposed model is compared with the measured σ^0_{vv} and σ^0_{vh} of the

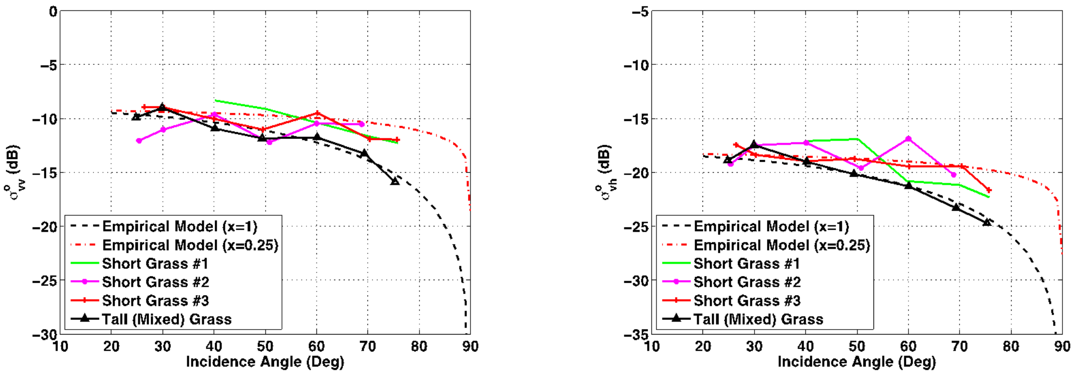

(a) (b)

Figure 4.18: Comparison between the measured backscattering coefficients of grass surfaces and the proposed empirical model (a) σ^0_{vv} and (b) σ^0_{vh}.

different grass surfaces in Fig.4.18 using two values for x : $x = 0.25$ and $x = 1$.

4.6 Conclusion

A newly constructed polarimetric instrumentation radar operating at 222 GHz has been used to conduct a series of outdoor measurements on both bare and vegetation-covered surfaces. Substantial backscattering was observed from both bare and vegetation-covered surfaces along with significant depolarization (up to -4 dB). Bare surfaces such as dirt and asphalt are electrically rough surfaces at 222 GHz, and their subsurface aggregates have sizes that are comparable with wavelength resulting in substantial radar backscatter response. The value of the copolarized backscattering coefficients of bare surface seems to quickly reach to a “ceiling” level as the surface roughness increased, and its dependence on the incidence angle follows that of a Lambertian surface. Despite the physical differences between the measured vegetation-covered surfaces, their backscattering coefficients exhibited similar values and demonstrated weak angular dependence on incidence angle. A hybrid empirical model is proposed for bare surfaces that combines two semi-empirical MMW models developed earlier to predict surface scattering and volume scattering from bare surfaces. Another empirical model is developed for vegetation-covered surfaces based on the data presented in this chapter. The measured data and models will be useful to radar engineers in future sensor designs at sub-THz frequencies.

CHAPTER V

Rectangular Waveguide Piezoelectric-Based Phase Shifter at Sub-THz Frequencies

5.1 Introduction

One of the main advantages of operating in the sub-THz frequency band, is the ability to realize very narrow beam antenna radiation pattern with a small physical aperture size leading to high resolution imaging. On the other hand, a large field of view (FoV) is required for most radar applications which mandates moving or scanning the antenna of the radar. In general, there are two methods to scan the antenna beam; mechanically and electronically. In the mechanical scheme, the radar's antenna (or the entire radar) is mechanically attached to a rotating platform. This scheme is conceptually easy and straight forward to implement, however, it yields slow beam steering as it involves mechanical movement of bulky antenna (or the entire radar) in addition to the rotating platform itself. This usually leads to slow refresh rate of radar images. The electronically beam steering scheme, on the other hand, is more complicated to implement but is much faster as the beam direction is controlled using an electrical signal rather than mechanical movement of heavy objects. For sub-THz radar

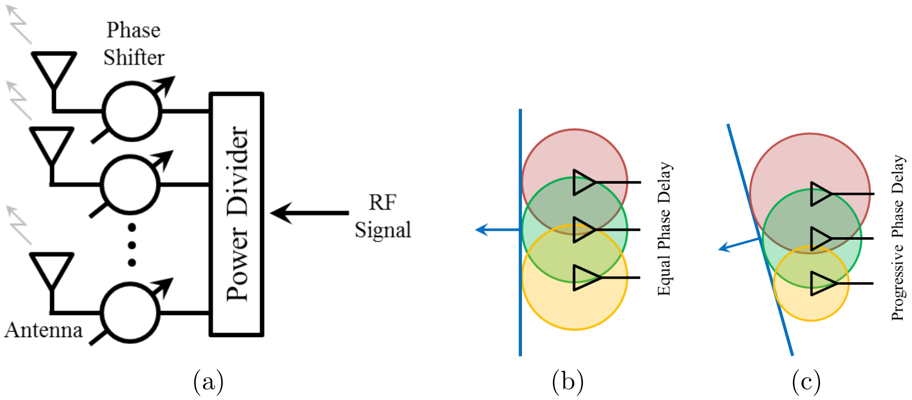

Figure 5.1: (a) Phased array architecture for realizing electronic beam steering radiation pattern. (b) In-phase feeding leading to broadside radiation direction. (c) Progressive phase feeding leading to steered radiation direction.

applications, the requirements of high resolution combined with large FoV and fast refresh rate mandates the application of the electronic beam steering scheme.

The conventional way to realize an electronic beam steering radiation pattern is through a phased array architecture as shown in Fig.5.1(a) [127], [128]. It is composed of an array of identical antennas with each one of them being fed through a dedicated phase shifter. By controlling the phase of the signal feeding each antenna element separately, the direction of the main beam can be controlled as shown in Fig.5.1(b) and (c). Different configuration for the feeding network can be used. The parallel (corporate) feed configuration is shown in Fig.5.2(a) which is composed of a cascade of power splitters creating a tree-like structure. Here, a separate control signal is needed for each phase shifter. This configuration is complex but it can give complete control over the radiation pattern were multiple peaks and multiple nulls can be realized at the same time (beam forming). Another feeding configuration is shown in Fig.5.2(b) and is called the series (end) feed configuration. Here, only one control signal is required to control all the phase shifters. This configuration is much simpler, but

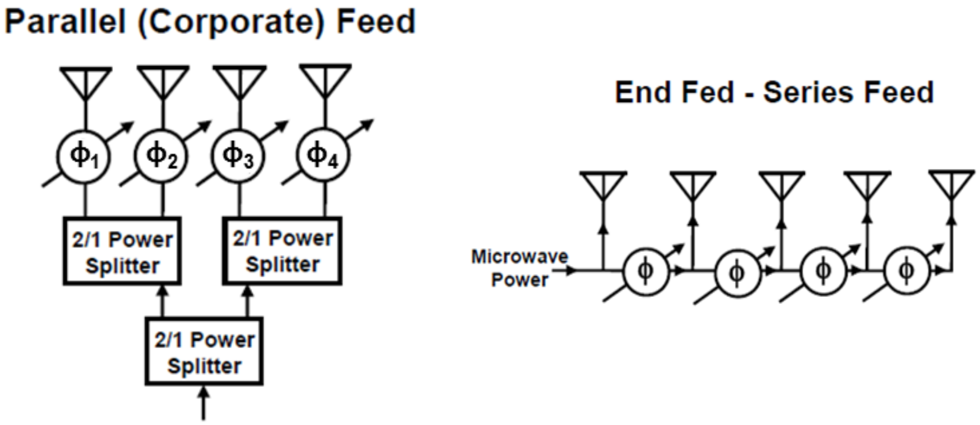

(a) (b)

Figure 5.2: Different feed configurations for the phased array architecture. (a) Parallel (corporate) feed. (b) Series (end) feed.

gives limited control over the radiation pattern as it is only suitable for beam steering and not beam forming applications.

From the previous discussion, it is clear that realizing very low loss phase shifters is essential to design efficient, electronic beam steering radars at sub-THz frequencies. This is especially true if a large number of array elements is required. Many novel designs have been proposed in the literature to realize phase shifters at MMW frequencies. This includes semiconductor devices based phase shifters (in the form of switches or varactor diodes) [129]–[136]. The basic idea here is to load a planar transmission line with variable capacitors to control the phase velocity of the EM signal and, consequently, its phase. Another approach is to switch the EM signal between different delay lines leading to a digital type phase shifter. In [137], tunable impedance surfaces were used to load rectangular waveguide walls in order to realize quasi-TEM transmission line with controllable dispersion relation. The structure showed 2π phase shift over the entire Ka-band but with an insertion loss of about 10 dB. In general, the performance of these phase shifters is limited by the series resistance of the semiconductor devices leading to a high insertion loss at the high end of the MMW frequency band. Furthermore, they have limited power handling capabilities. Instead of lumped semiconductor varactors, movable dielectric blocks [138]–[141] or movable capacitive MEMS bridges [142], [143] can be used to control the effective propagation constant of the transmission line. This technique was demonstrated for frequencies up to 100 GHz in the W-band [143], however, it showed poor insertion loss performance of about 1 dB per 60^o phase shift (i.e. 6 dB to obtain 360^o). Another category of phase shifters utilizes some exotic properties of special types of materials to realize the phase shift. This includes ferroelectric materials [144], [145] as well as liquid crystal materials [146]–[149] in which the dielectric permettivity of the material can be varied through the application of an external electric field. These materials suffer from increased losses at MMW frequency range and, generally, cannot be used at sub-THz frequencies. Based on the previous examples, two observations need be kept in mind when designing low-loss, phase shifters at sub-THz frequencies: 1) no dielectric material should be included as it will fundamentally contribute to dielectric losses, and 2) planar transmission lines like microstrip and coplanar waveguide should be avoided to eliminate the dielectric losses. Instead, a hollow metallic waveguide void of lossy dielectrics, like the rectangular waveguide, might be more appropriate.

In this part of the dissertation, we propose a novel piezoelectric-based phase shifter implemented in rectangular waveguide technology that can be realized using silicon microfabrication techniques for sub-THz applications. The design relies on actuating a metallic strip inside a rectangular wave to realize a tunable artificial perfect magnetic conductor (PMC) boundary condition. It is important to mention here that the idea of loading rectangular waveguide with perfect magnetic conductors was originally proposed in [150], and later used to realize phase shifters in [137]. The emphasis there was to realize the so-called quasi-TEM mode inside a rectangular waveguide configuration. Here, we are not trying to realize a quasi-TEM mode, but rather to tune the dispersion relation of the regular TE_{10} mode. The main emphasis here is to realize phase shifters at sub-THz frequencies with minimal loss that can be fabricated using silicon microfabrication techniques. This is reflected on the choice of the perfect magnetic conductor realization used as well as the actuation mechanism to achieve variable phase shift with minimal movement of a metallic membrane. The actuation is done using an external piezoelectric actuator with a 200 µm travel range. Although the design is implemented at 240 GHz, it can be scaled to higher frequencies in a straight forward manner.

In Section 5.2, the proposed structure is introduced and the theory of operation is discussed. The fabrication steps is presented in Section 5.3 together with the measurement results. Conclusions are summartized in Section 5.4.

5.2 Rectangular Waveguide Piezoelectric-Based Phase Shifter

The proposed phase shifter is shown in Fig.5.3. It is composed of three main parts: 1) an input/output upright rectangular waveguide supporting fundamental TE_{10} mode, 2) transition section from upright rectangular waveguide to PMC loaded rectangular waveguide and vice versa, and 3) PMC loaded rectangular waveguide composed of a vertically movable metallic strip inside a half-width, upright rectangular waveguide. The phase shifting action is achieved at the central section and is best explained through the yellow inset in Fig.5.3. The design starts with an upright rectangular waveguide. Using the image theory, it can be shown that this structure is electromagnetically equivalent to a half-width rectangular

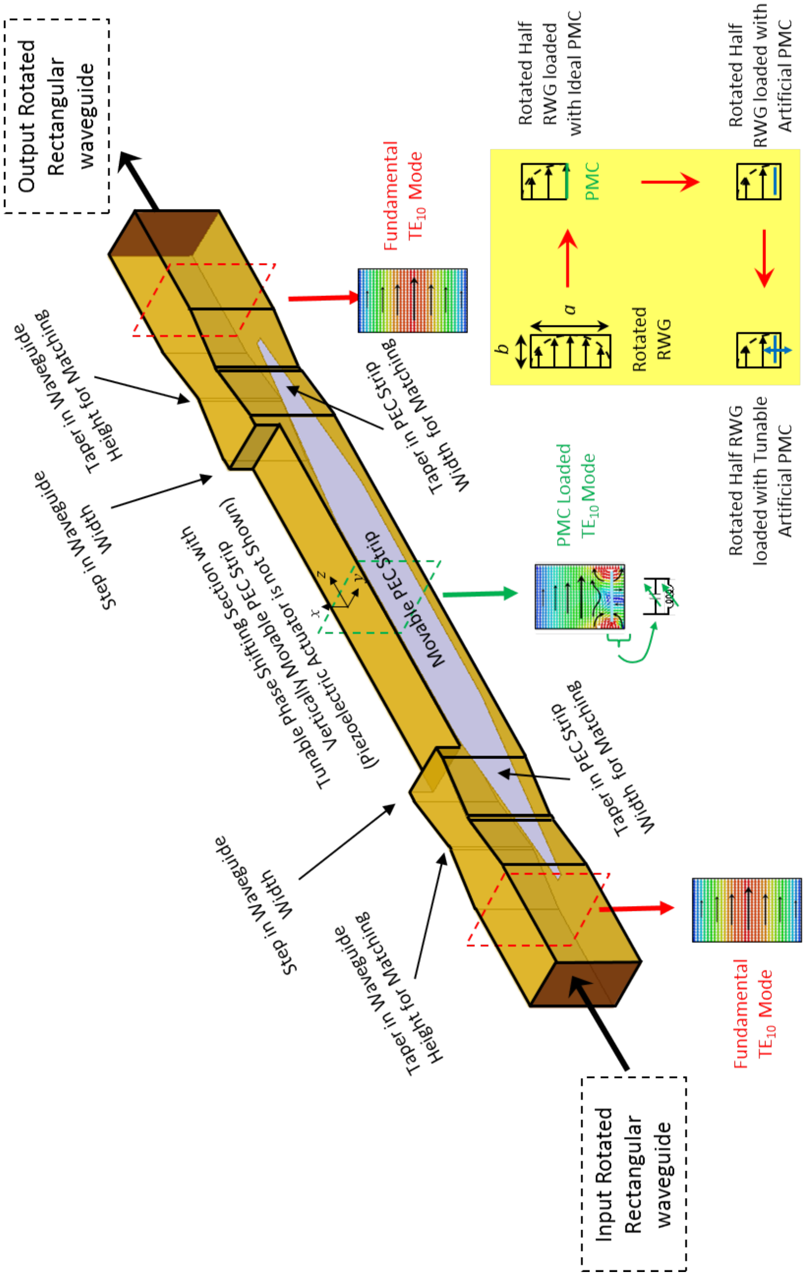

Figure 5.3: Proposed rectangular waveguide piezoelectric-based phase shifter. Electric field at selected cross sections is calculated using Ansys HFSS software (based on finite element method formulation). Piezoelectric actuator is not shown here.

waveguide, but with one of the short walls replaced with a PMC or, open circuit boundary condition. In other words, these two structures will have identical dispersion relation. Now, since a PMC does not exist, an artificial effective PMC is realized over a limited frequency bandwidth through suspending a perfect electric conductor (PEC) strip near the bottom wall of the half-width rectangular waveguide. The combination of the PEC strip together with the wall can be modeled as a shunt tank circuit. This equivalent circuit represents an open circuit boundary condition at its resonance frequency. By vertically actuating the PEC strip over the wall, both the inductance and capacitance of the tank circuit can be tuned leading to a variable resonance frequency. Consequently, the dispersion relation of the PMC loaded rectangular waveguide can be varied resulting in a variable phase shift for a signal traveling through it.

Although the previous concept was explained using a PMC boundary condition which has a reflection coefficient of $1\angle 0^o$ together with a half-width rectangular waveguide, it can be generalized to any artificial surface with unity reflection coefficient magnitude and arbitrary phase angle as long as the total round trip phase at the waveguide transverse cross section is multiple of 2π. The step in the waveguide width at the central section shown in Fig.5.3 is an extra degree of freedom that can be used to engineer the dispersion relation and will be explained in more details in the next section. At this stage, it is important to make the following observations. First, the PMC loaded rectangular waveguide has two separate conductors (waveguide walls and the PEC strip) and, in theory, can support pure TEM mode. However, the mode that is excited and supported is very similar to the TE_{10} mode as shown by the field plots in Fig.5.3. In fact, the pure TEM mode cannot be excited here since it has an electric field with even symmetry about the $x-z$ plane, while the fundamental TE_{10} mode of the feeding upright rectangular waveguide has an electric field with odd symmetry about the $x-z$. The transition from the regular TE$_{10}$ mode to the PMC loaded TE$_{10}$ mode and vice versa is facilitated through the use of gradual tapering in both the waveguide height as well as the PEC strip width along the propagation direction. Second, the phase shifter has only conductor losses and no dielectric losses improving the insertion loss. Finally, to further reduce losses, the simplest realization of PMC boundary condition is adapted here which is basically a conductor strip over a metallic ground, in comparison with more complex shapes like Jerusalem cross [150], or thin dipoles [151].

5.2.1 Analysis of PMC Loaded Rectangular Waveguide

Following [150], the dispersion relation for the proposed PMC loaded rectangular waveguide can be calculated using the transverse resonance technique [152]. Specifically, for closed waveguides with constant cross section along the propagation direction, the propagation constant (β) can be written as:

$$\beta = \sqrt{k_o^2 - k_c^2} \tag{5.1}$$

where $k_o = \omega\sqrt{\mu_o \epsilon_o}$ is the free space propagation constant, and k_c is the cut-off wavenumber which is a constant depending only on the cross-section geometry. The objective of the transverse resonance technique is to estimate k_c using a transmission line like model. This is shown in Fig.5.4(a). In the case of PMC loaded TE$_{10}$, the cut-off wavenumber is the one that solves the following equation:

$$Y_{up}(x) + Y_{dn}(x) = 0, \qquad for\, any\, cross\, section\, x \tag{5.2}$$

where $Y_{up}(x)$ is the admittance at cross section 'x' looking up, while $Y_{dn}(x)$ is the admittance looking down. If we take the cross-section to coincide with the PEC strip location and using simple transmission line theory, the previous equation takes the following form:

$$-jY_o \cot\left(k_x (t-h)\right) + Y_{strip} - jY_o \cot\left(k_x h\right) = 0 \tag{5.3}$$

where k_x is the transverse propagation constant in the $'x'$ direction, $Y_o = {}^{k_x}\!/\!_{\omega\mu_o}$ is the characteristic impedance for TE modes, and Y_{strip} is the equivalent admittance of the PEC strip inside the waveguide. Using the image theory and the fact that TE$_{10}$ of rectangular waveguide can be decomposed at cut-off into two plane waves bouncing up and down, it can be easily shown that the determining Y_{strip} is exactly equivalent to calculating the sheet admittance of 1D conductor grating over a ground plane as shown in Fig.5.4(b). This problem has received significant attention in the literature in the context of artificial magnetic conductors, frequency selective surfaces, and high impedance surfaces [153]–[156]. In [155], the capacitance value used was that of an infinite metallic grating in free space originally calculated by Markuvitz [152]. The problem with that model is that it did not account for the interaction between metallic strip and the upper and lower metallic walls. A more rigorous field approach that is valid for wide range of parameters and incident angles was presented in [156] and is adapted here. Without going into mathematical details, the equivalent admittance of periodic PEC strips over a top and bottom metallic walls under normal plane wave incidence, as show in Fig.5.4, can be written explicitly as:

$$Y_{strip} = \sum_{n=1}^{\infty} \left[2 \times \left(J_o \left(\pi n \left(1 - \frac{w}{b} \right) \right) \right)^2 \times \left(-jY_{o,n} \cot\left(k_{x,n}(t-h)\right) - jY_{o,n} \cot\left(k_{x,n} h\right) \right) \right]$$

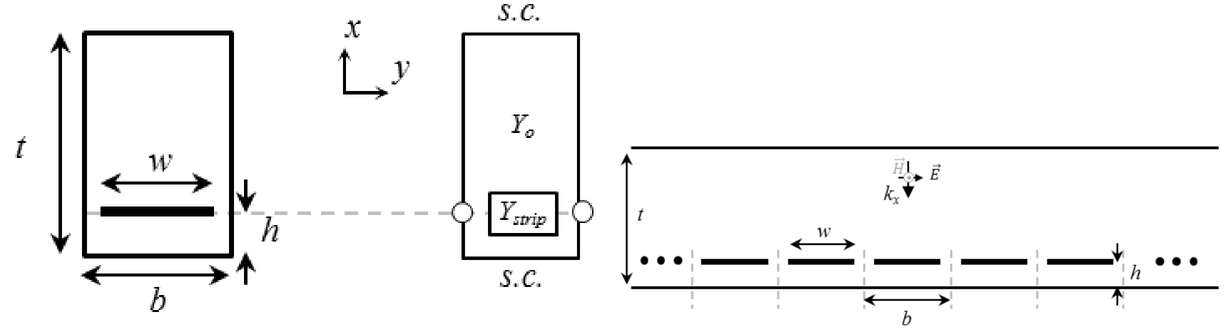

(a) (b)

Figure 5.4: (a) Transverse resonance technique applied on PMC loaded rectangular waveguide. (b) Equivalent problem to estimate Y_{strip}.

$$k_{x,n} = \sqrt{k_x^2 - \left(\frac{2\pi n}{b}\right)^2}, \quad Y_{o,n} = \frac{\omega\epsilon_o}{k_{x,n}} \tag{5.4}$$

where $J_o()$ is the zeroth order Bessel function. Substituting the above equation in (5.3), we can get an implicit equation that can be solved numerically for the cut-off wavenumber 'k_x'. This is done in Fig.5.5(a) for the shown geometrical dimensions. For comparison, the dispersion relations calculated numerically by a finite element method (FEM) solver (Ansys HFSS) are also shown and very good agreement is obtained. It can be observed that as the gap height 'h' increases from 20 μm to about 764/2 μm, the dispersion relation changes from that of a TE$_{10}$ mode in a regular rectangular waveguide with the same broadwall dimension to the dispersion relation of a TE$_{10}$ mode in a regular rectangular waveguide but with double the broadwall dimension. As a result, significant phase variation can be obtained over a relatively short length of the phase shifter. For example, about $85^o/mm$ variation in the propagation constant can be obtained at a frequency of 240 GHz ($\lambda_o = 1.25$ mm, $\lambda_g = 2.17$ mm at 240 GHz). It is also observed that the rate of change of β is large when h is small (from 0 to 170 μm) and after that, the effect of changing the gap height on

β becomes very small. Thus, when actuating the PEC strip, it might not be that useful to increase the gap height beyond 170 μm for this particular example. In Fig.5.5(b) and (c), the PEC strip width is reduced to 300 μm and 150 μm, respectively. It can be seen that the rate of change of β with the gap height h gets weaker as the resulting change in the propagation constant is only $50^o/mm$ and $15^o/mm$, respectively. Thus, when designing a phase shifter using this technique, the PEC strip width should be increased as much as the fabrication tolerance can allow. Another important factor that affect the dispersion relation is the waveguide width 't' shown in Fig.5.4(a). Changing this factor has the effect of shifting the entire dispersion relation band as demonstrated in Fig.5.6. Thus, as mentioned before, the step in waveguide width in Fig.5.3 is an additional degree of freedom that can be used to engineer the dispersion relation independent of the input/output feeding waveguide width.

To gain more insight of why such a significant phase shift change can be obtained from the proposed design, it is instructive to look at (5.3) as a summation of two terms: 1)Y_{cap} representing the capacitive part of the total admittance which corresponds to PEC strip sheet admittance (i.e. $Y_{cap} = Y_{strip}$), and 2) Y_{ind} representing the inductive part of the total admittance which corresponds to the top and bottom shorted transmission lines (i.e. $Y_{ind} = -jY_o \cot\left(k_x\left(t-g\right)\right) - jY_o \cot\left(k_x g\right)$). These two quantities are plotted in Fig.5.7 for different gap heights. It can be seen that both the capacitance and inductance of the tank circuit change with the gap height. This will result in large rate of change of the phase shift versus the gap height in comparison with tuning either the capacitance or inductance separately [137]. It also can be seen that the capacitive part changes significantly for small gap heights as the capacitance is dominated by the parallel plate capacitance and then reaches a saturated value that corresponds to the fringing capacitance between the PEC

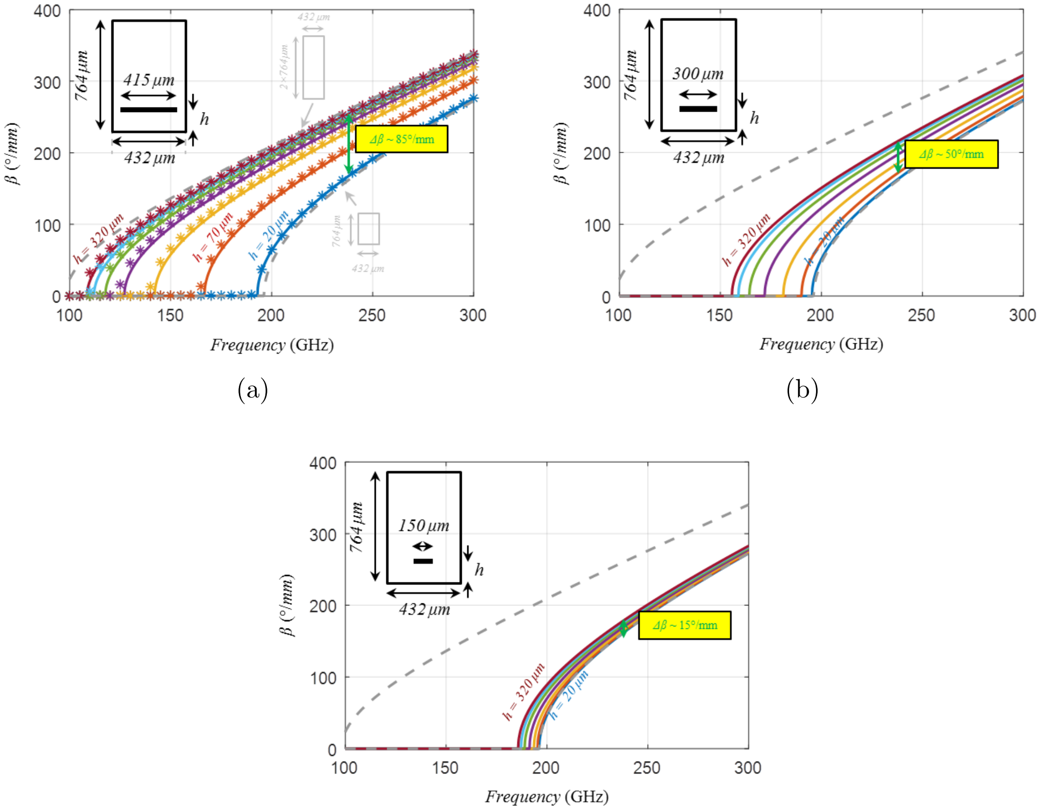

(a) (b)

(c)

Figure 5.5: Dispersion relation for PMC loaded rectangular waveguide at different gap heights (h). The solid lines are calculated using (5.3), while the star points are obtained from Ansys HFSS numerical simulation. Also shown in dashed lines the dispersion relation for regular TE_{10} modes in rectangular waveguides with the same broadwall dimensions as well as double broadwall dimensions. (a) PEC strip width = 415 μm. (b) 300 μm. (c) 150 μm.

strip and the waveguide broadwalls. This can justify the increased rate of change of β versus h for small gap heights that is observed in 5.5(a).

Another interesting point to mention is that although the focus of the design here is to realize phase shifters, the same design can be used to realize efficient switches with very good isolation performance. As can be seen from Fig.5.5(a), by changing the gap height

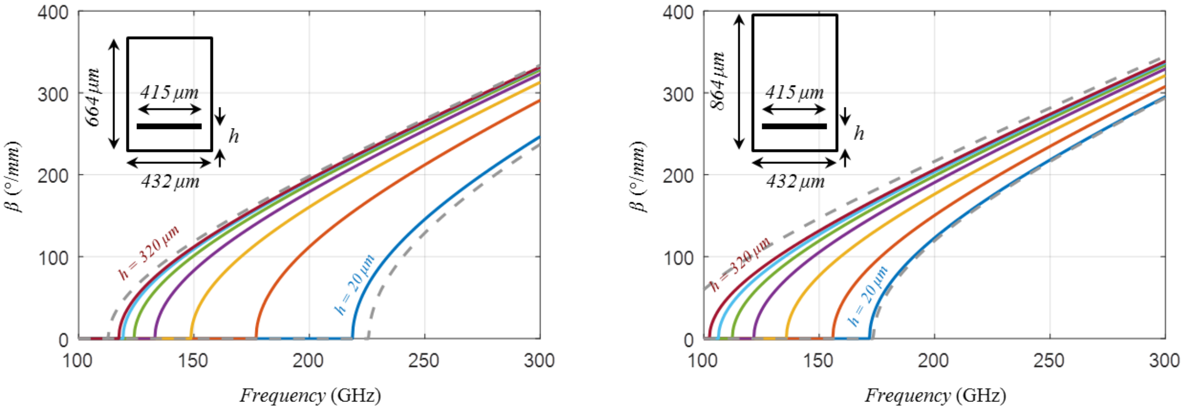

(a) (b)

Figure 5.6: Dispersion relation for PMC loaded rectangular waveguide at different gap heights (h). (a) $t = 664\ \mu m$. (b) $t = 864\ \mu m$.

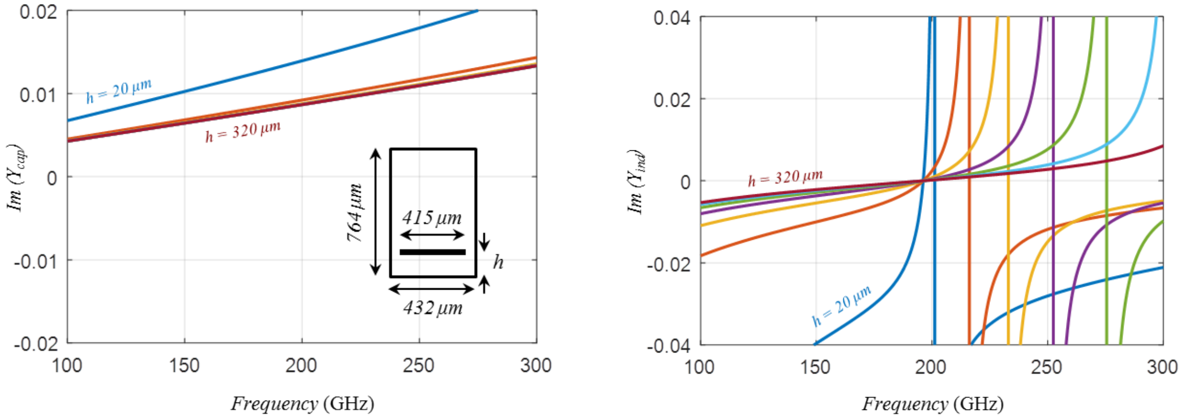

(a) (b)

Figure 5.7: Capacitive and inductive parts of the PMC loaded rectangular waveguide admittance at different gap heights (h). (a) Y_{cap}. (b) Y_{ind}

from 20 μm to 170 μm, a signal , at 150 GHz for example, can be transmitted (propagating mode) or entirely reflected (evanescent mode). Finally, in contrast with [137], [150], the dispersion relation at all gap heights shows the regular fast wave behavior of rectangular waveguide with no slow wave anomalies.

5.2.2 Phase Shifter Design

Form Fig.5.5(a), it can be observed that operating near the cut-off frequency of 200 GHz will result in the maximum phase sensitivity (i.e. phase variation versus gap height). However, there are two problems. First, dispersion effects are more dominant near the cut-off frequency limiting the available bandwidth. Second, it becomes very difficult to match the PMC loaded rectangular waveguide. In this work, we are interested in designing a phase shifter at 240 GHz. Choosing the cut-off frequency of the unloaded rectangular waveguide to be around 200 GHz is found to give a good compromise between phase sensitivity and impedance matching. By optimizing the dimensions of the taper in waveguide height as well as the taper in PEC strip width in Fig.5.3, the structure can be matched around the frequency of interest at all gap heights. The final structure dimensions are given in Fig.5.8. It is composed of the following sub-sections: 1) Two optimized H-bends to access the input and output ports of the phase shifter with external standard size WR-03 waveguides for measurements (WR-03 dimensions are $864\mu m \times 432\mu m$ leading to 173.5 GHz cut-off frequency for the fundamental TE_{10} mode) , 2) PMC loaded rectangular waveguide, and 3) four, two-stage RF choke sections to suspend the PEC strip inside the waveguide through connection to a supporting frame which itself is attached to a piezoelectric actuator (the actuator is not shown in Fig.5.8). Note that the step in waveguide width degree of freedom shown in Fig.5.3 is not utilized here in the final design, but rather the width of the entire phase shifter between the two H-bends is set to be 734 μm (instead of the standard WR-03 width of 864 μm) to avoid an extra fabrication step. Also, note that the PEC strip width is set to be 400 μm instead of $415\mu m$ for fabrication considerations. Next, the design parameters for each section of the phase shifter is described.

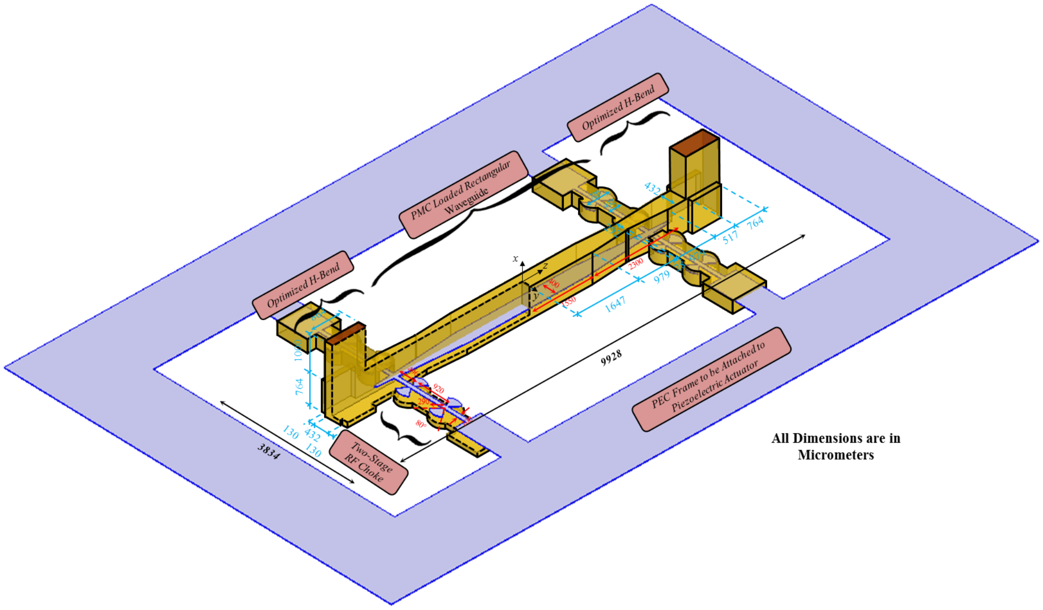

Figure 5.8: Complete phase shifter with dimensions.

Optimized H-Bend

As explained earlier, to characterize the phase shifter, connection to external waveguide probes are needed. Here, we design an H-bend to connect the on-wafer waveguide to the external standard WR-03 waveguide probe. A direct right-angle H-bend for a rectangular waveguide has poor performance in terms of power transfer and impedance matching [152]. In practice, a mitered bend or a radial bend with a large radius is typically used. Both of these techniques are not suitable for silicon microfabrication. Hence, another method is devised here which does not add any additional step to the fabrication process. The configuration of this proposed H-bend is shown in Fig.5.9. Basically, square indentations are created on both sides of the waveguide at the H-bend junction in order to create a reflected wave that can cancel the reflected wave from the right-angle bend at the design frequency. By optimizing the depth of the indentation, the impedance matching can be improved from 7 dB

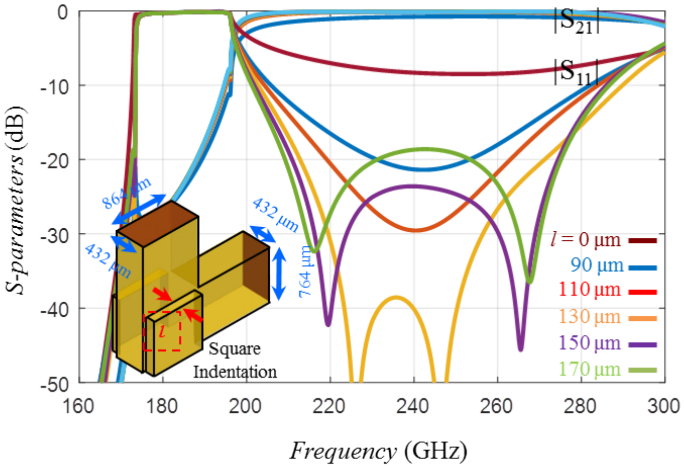

Figure 5.9: S-parameters for the optimized rectangular waveguide H-bend.

to more that 30 dB around 240 GHz. Compared to a mitered H-bend, the proposed design has a narrower bandwidth but is much easier to fabricate using silicon micro-fabrication. Note that the input rectangular waveguide has a broadside dimension of a standard WR-03 waveguide (864 μm), while the output rectangular waveguide has a broadside dimension of 764 μm.

PMC Loaded Rectangular Waveguide

Fig.5.3 shows that there are some differences in the electric field configuration between a regular TE_{10} mode and the PMC loaded TE_{10} mode. This can lead to poor matching if the fields near the transition are not treated properly. To mitigate this problem, tapering both the waveguide height as well as the PEC width is found to give a smooth transition between the two modes. The dimensions of the two tapers were optimized through full-wave simulations (Ansys HFSS) and the result is shown in Fig.5.10 where good matching is achieved for all gap heights around the center frequency of 240 GHz.

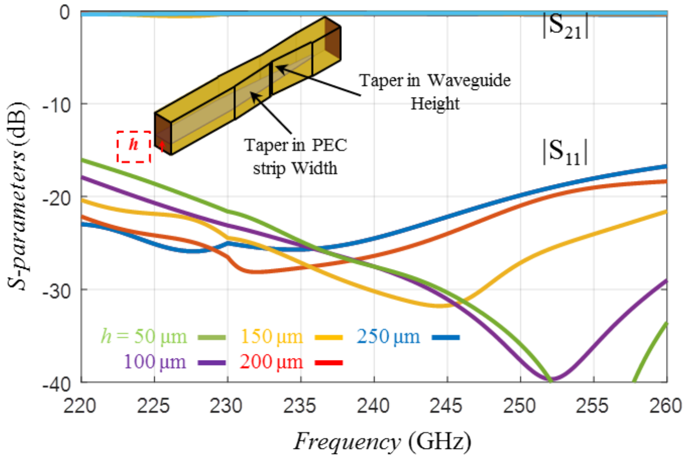

Figure 5.10: Transition from PMC loaded rectangular waveguide to a regular rectangular waveguide. Good matching is achieved at all gap heights.

Two-Stage RF choke

To enable vertical movement of the PEC strip inside the upright rectangular waveguide, the strip is anchored at four points through RF chokes as shown in Fig.5.8(a). An RF choke is typically composed of a $\lambda/4$ low impedance open circuited stub separated by a $\lambda/4$ high impedance transmission line from the main line. It is commonly used in bias networks to prevent the RF signal from leaking out of the main transmission line, while allowing the DC bias to pass through. In our case, it is used to confine the microwave signal inside the main rectangular waveguide, while being able to support the PEC strip in order to actuate it vertically. The width of the RF choke waveguide as well as the PEC strip inside it was chosen such that the cut-off frequency of the corresponding PMC loaded TE_{10} mode is much higher than 300 GHz at all gap heights. Hence, the only mode that is supported is the pure TEM mode. The dimensions of the RF chokes as well as the anchoring locations were optimized using full-wave simulations (Ansys HFSS) and the result is shown in Fig.5.11. To increase

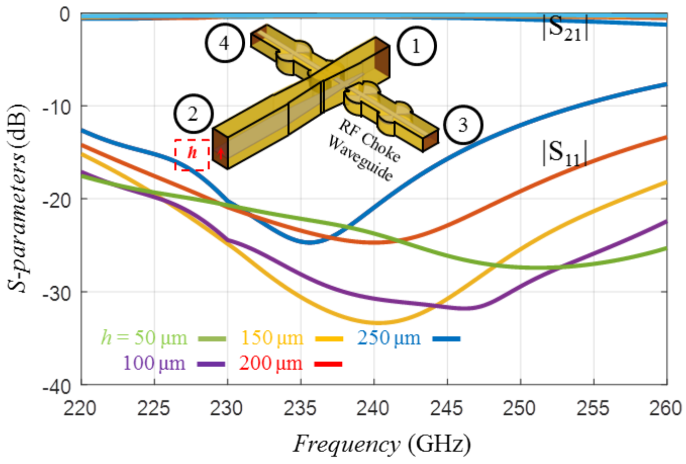

Figure 5.11: Effect of RF choke on S-parameters at different gap heights.

the isolation between port 1 and port 3 (port 4), two stage RF chokes are necessary. This resulted in $|S_{31}|$ and $|S_{41}|$ better than 40 dB across the band of interest at all gap heights (if one stage is used, the worst case isolation can be around 15 dB only).

Combining the previous three sections, full-wave simulation for the entire phase shifter is carried out and the results is shown in Fig.5.12 . The return loss is better than 10 dB, while the insertion loss is better than 1 dB across the band from 230 to 250 GHz at all gap heights (the simulation includes conductor losses). The phase shift versus gap height at 240 GHz is shown in Fig.5.12(b) where a 360^o phase shift can be achieved by changing the gap height from 30 μm to about 200 μm.

5.3 Fabrication and Measurement Results

The silicon microfabrication procedure is described in this section. The main process in this procedure is Deep Reactive Ion Etching (DRIE) of silicon through the Bosch process.

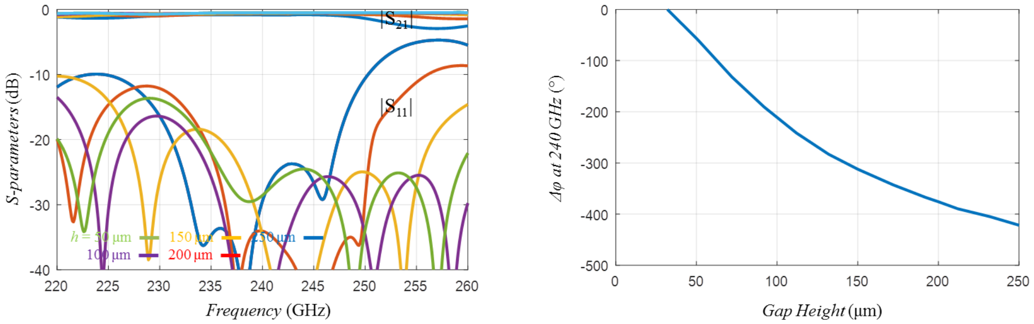

(a) (b)

Figure 5.12: Complete phase shifter full-wave simulations. (a) S-parameters at different gap heights. (c) Phase shift at 240 GHz versus gap height.

Basically, it is a fluorine-based plasma etching process that is commonly used to etch very deep trenches in silicon with etch rates as high as 20 μm/min [157]. The physics of the etching process will not be explained here, but the resulting trench characteristics will be discussed since it can have major implications on the device performance. All fabrication steps in this section are carried out at the Lurie Nanofabrication Facility at the University of Michigan.

To characterize the etching process, a test run was carried out on STS Pegasus DRIE tool with different trench dimensions. A typical trench profile is shown in Fig.5.13. Three main non-idealities can be identified: 1) The sidewalls are not vertical, but rather slightly slanted at 2.25^o. 2) The bottom of the trench is not flat, but rather curved. 3) Upon zooming on the sidewalls, surface roughness can be clearly identified which is a well know property of the Bosch process called "scalloping". The first two non-idealities need to be carefully included in the EM simulation model which is done for all simulation results in this chapter. The third non-ideality is found to be not important at this frequency range since the undulation period and depth is much smaller than the operating wavelength.

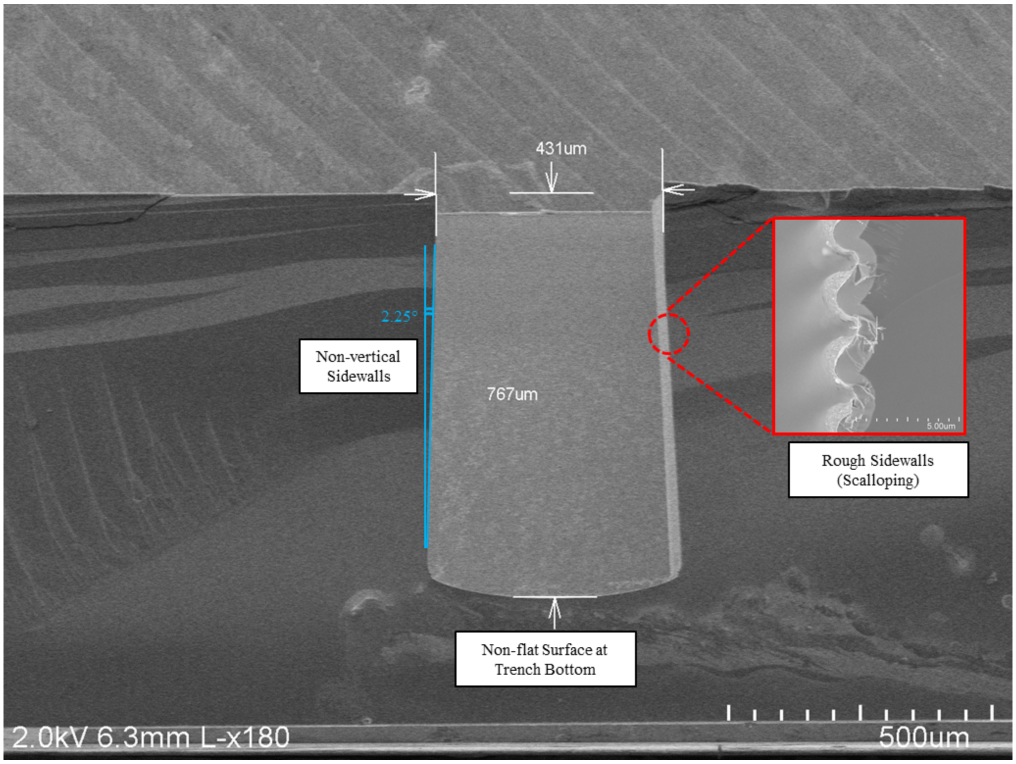

Figure 5.13: Typical DRIE silicon trench profile. After etching, a 2 μm of PECVD oxide was deposited.

The fabrication procedure is described in Fig.5.14. Basically, the phase shifter is divided into two halves (top half and bottom half) and each half is fabricated on a separate silicon wafer. Alignment between the two halves is done mechanically by fabricating an additional groove in the bottom half, and a matching protrusion on the top half (with dimensions smaller by 5 μm). Once the two halves are fabricated, the metal strip is carefully placed inside the bottom half, and then the top half is placed on top and aligned under an optical microscope. Thus, the top and bottom halves of the waveguide are aligned with accuracy better than 5 μm. Compared to previous research effort [158], [159], all of the fabrication steps are done at room temperature without the need of any high temperature wafer bonding step. This is possible since the surface currents for upright rotated rectangular waveguide supporting a TE_{10} mode (and for PMC loaded TE_{10} mode) in Fig.5.14 at the two wafer interface are only along the interface direction. Hence, even if there is a small air gap between the upper and bottom halves, the effect on performance will be minor. To validate this assumption, a full-wave simulation is carried out in which an air gap with irregular shape and 10 μm thickness is included. The S-parameters simulation is shown in Fig.5.15 where the return loss is still better than 10 dB, but the insertion loss is increased to 1.7 dB. The performance deteriorates with increasing the air gap thickness. It should be noted that the best insertion loss performance is found through full-wave simulation to happen when the mating interface, between the top and bottom waveguide halves, is shifted a little bit down from the center by 65 μm. Another important observation here is that most piezoelectric material, like Lead Zirconate Titanate (PZT), can work only up to 200^oC [160] or even less. Hence, the fabrication method must not have any step with temperature higher than 200^oC if such piezoelectric material is to be integrated with the fabrication process.

The process uses five lithography masks. For all lithography steps, a 5 um of photoresist (Shipley SPR-220) is used. Two step etching is done on the bottom wafer with 2 μm of PECVD oxide as one mask layer and SPR-220 as another mask layer. A similar two step etching is done on the top face of the top wafer to etch the input/output waveguide access ports, as well as the measurement probes access ports. A final DRIE etch is done on the bottom face of the top wafer to form the top half of the waveguide. Next, both wafers are metalized by sputtering 20 nm titanium adhesion layer, followed by 0.5 μm gold sputtering, followed by another 2 μm gold plating to ensure good gold coverage on the waveguide sidewalls. Finally, both wafers are diced.

For the aluminum frame, a standard duty aluminum foil of thickness 17 μm is laminated to a 2" × 3" microscope glass slide using a special water soluble glue called Crystalbond-555. This

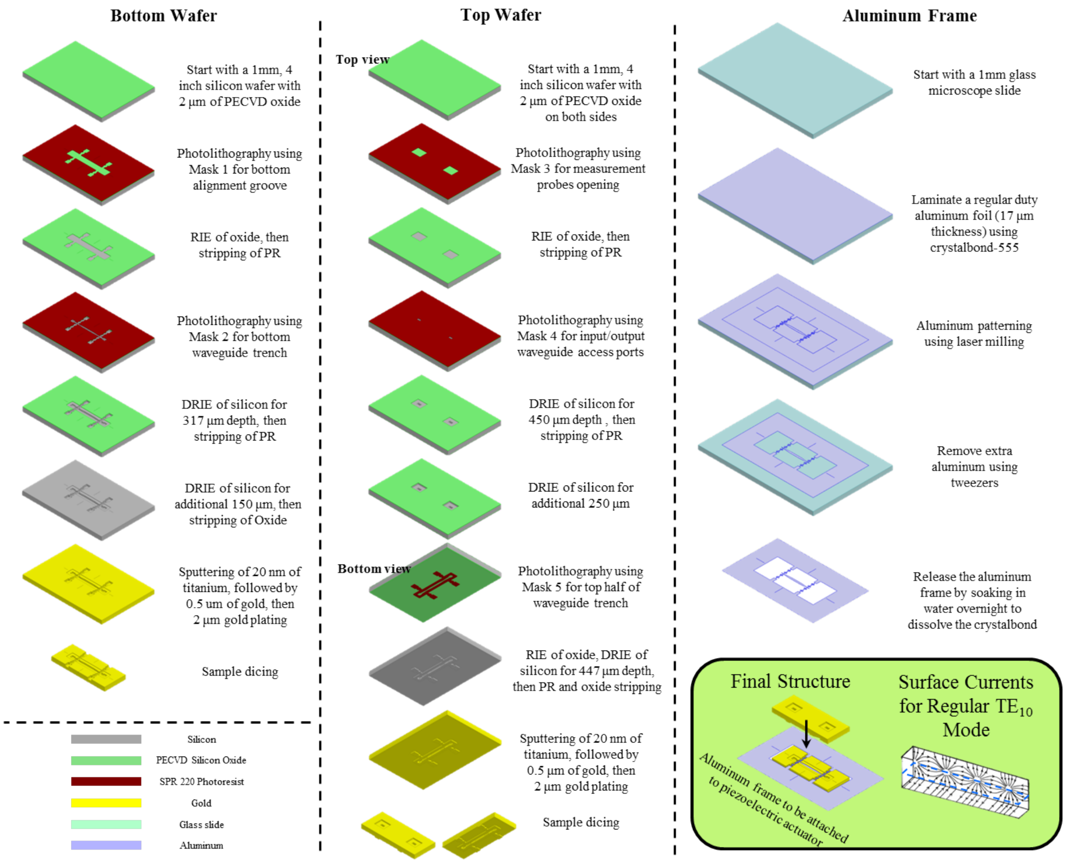

Figure 5.14: Fabrication procedure for the phase shifter.

glue is wax like and is solid at room temperature. It starts to melt by heating it up beyond 55^oC. The glass slide is first put on a hot plate at 80^oC. A piece of the glue is laid over the glass slide for about half a minute until it completely melted. Using a razor blade, the glue is carefully spread over the microscope glass. The aluminum foil sheet is then placed over the glue, and another glass slide is put on top. Next, the sandwich is removed from the hotplate and allowed to cool down to room temperature, while firmly pressing by hand to create a uniform and smooth glue layer under the aluminum sheet. Finally, the top glass layer is removed. This technique is found to give very good and repeatable lamination results

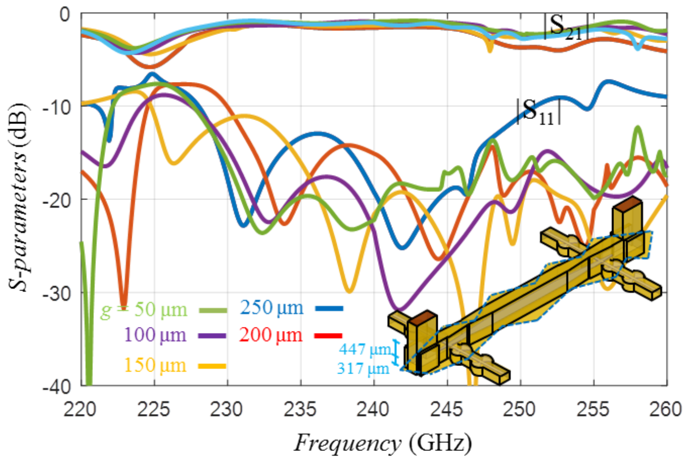

Figure 5.15: Effect of 10 μm air gap between the top and bottom waveguide halves on S-parameters.

between the aluminum foil sheet and the glass slide. Next, the laminated aluminum foil sheet is patterned through laser cutting. No patterning through RIE was attempted because the aluminum layer is very thick and no anisotropic aluminum etching recipe was available. The laser cutting machine used is ProtoLaser-S available from LPKF and originally used for copper laser cutting of printed circuit boards [161]. The tool has 25 μm beam diameter in focus, $\pm 2\,\mu m$ mechanical accuracy and 50 μm/ 25 μm minimum line/space. This resolution is found to be good enough for our application given that our minimum feature length is about 100 μm. After laser cutting, the excess aluminum is carefully removed manually by tweezers, and the sample is soaked in water overnight to dissolve the crystalbond and release the aluminum frame.

For the piezoelectric actuator, we decided to use AP350B from PiezoDrive which has the smallest footprint we could find with adequate travel range [162]. Specifically, the actuator has a size of 22 mm × 8 mm × 6 mm, a 350 μm travel range at 150 V maximum applied voltage, 400 Hz resonance frequency, and a weight of 7 grams. The actuator is externally

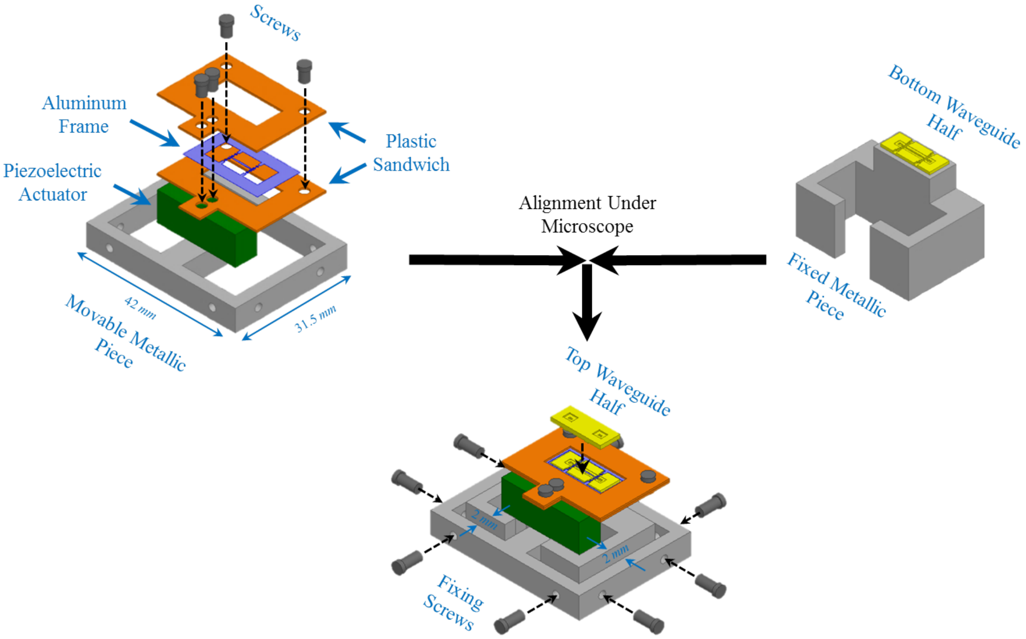

Figure 5.16: Integration of the entire phase shifter.

integrated with the phase shifter as shown in Fig..5.16. Basically, the actuator is attached to a thick metallic piece (called the movable piece). Then, the aluminum frame is sandwiched between two plastic pieces and attached to the actuator from the top. Next, the bottom waveguide half is placed over another metallic piece (called the fixed piece). The two pieces are brought together and carefully aligned under an optical microscope to make sure that the aluminum frame fits inside the bottom waveguide half. Once satisfactory alignment is achieved, the movable and fixed metallic pieces are locked together using eight fixing screws, and the top waveguide half is placed to form the complete phase shifter.

Once the phase shifter is assembled, its S-parameters are measured using the setup shown in Fig.5.17. It is composed of Agilent PNA-X (N5254A) vector network analyzer connected to two frequency extenders (V03VNA2) available from OML. The extenders cover the frequency range from 220 GHz - 325 GHz. Two custom made waveguide probes are connected to the frequency extenders. The probes have RF chokes machined at their tips to minimize the reflection from the possible gap at the interface between the probe and the on-wafer waveguide opening [163]. The VNA is calibrated using the through-reflect-line (TRL) technique up to the reference planes shown in Fig.5.17. The losses of the probes are calibrated out by measuring the reflection coefficient from a gold surface (short circuit) and estimating the two way propagation losses (about 2.5 dB each way). The piezoelectric is actuated using a 150V power supply, and the S-parameters are measured every 10 volt increment. The voltage readings are transformed to displacement in micrometer using the piezoelectric actuator deflection data sheet. The results are shown in Fig. 5.18. Without the aluminum frame, the insertion loss is around 1 dB, while the return loss is better than 10 dB across the band from 230 GHz to 250 GHz. After inserting the aluminum frame, the insertion loss showed a variation from 1.5 dB to 3 dB (2.25 dB average value) while the return loss is still better than 10 dB as the gap height is actuated between 40 μm and 200 μm (corresponding to 60V applied voltage on the piezoelectric actuator). These results include the mismatch at the probe-wafer interface as well as the H-plane right angle bend. They are a little bit worse than the simulation results shown in Fig.5.15. The achieved phase shift at 240 GHz is shown in Fig.5.18(b) where a total phase shift of 380^o is achieved as the gap height is varied from 40 μm to 200 μm. Actuating the frame beyond 200 μm is found to give a small phase change while heavily penalizing the insertion loss.

Next, two sets of measurements are performed to characterize the repeatability of the phase shifter. In the first set, the integrated phase shifter in Fig.5.16 is taken apart, then the aluminum frame is replaced with a new one, and then the phase shifter is assembled again. This measurement is conducted to characterize the repeatability of the optical alignment

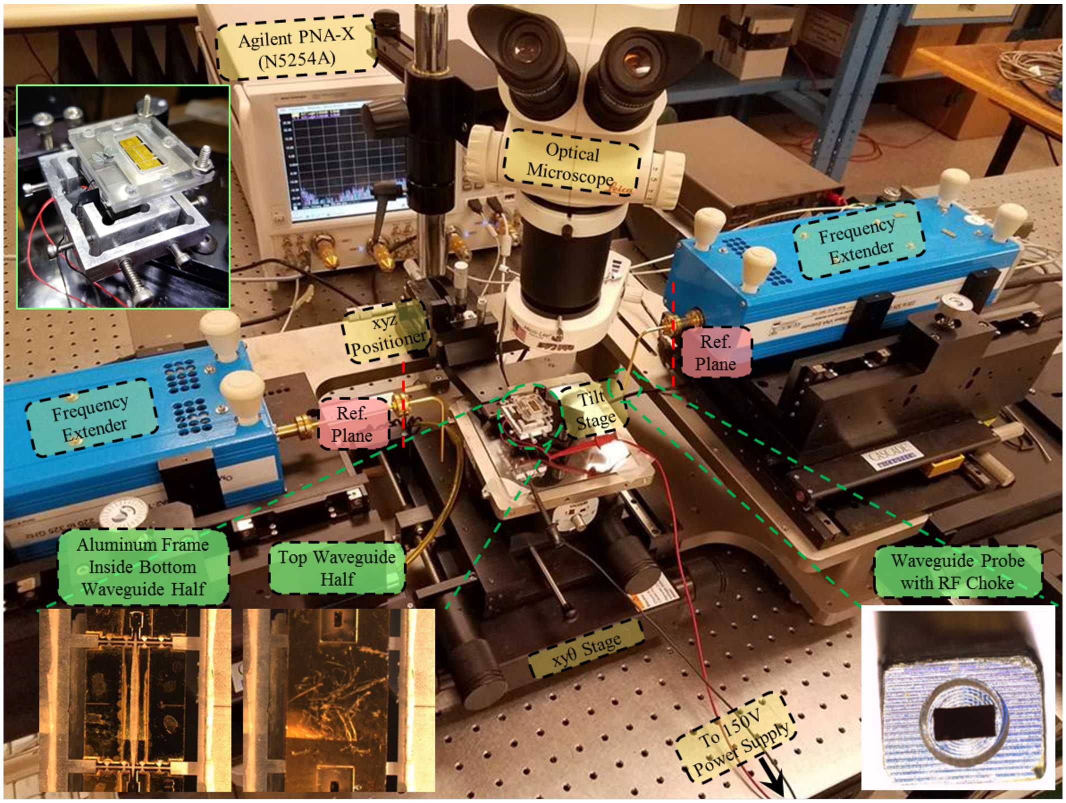

Figure 5.17: Alignment and Measurement Setup.

process and is repeated three times. The results are shown in Fig.5.19. The S-parameters are consistent for the three trials where the insertion loss varies between 1.5 and 3 dB, while the return loss is better than 10 dB for all gap heights. As for the phase at 240 GHz, discrepancies on the order of $\pm 25^o$are observed in Fig.5.19(e). The second set of measurement is intended to characterize the fatigue of the piezoelectric actuator and its effect on the phase shift. For that, the phase shift versus gap height is first measured, then the piezoelectric actuator is cycled for about 1.5 million cycle by applying a voltage sine wave at 30 Hz for about 14 continuous hours, then the phase shift versus gap height is measured again. Fig.5.20 shows the phase error at 240 GHz between the two measurements where a value

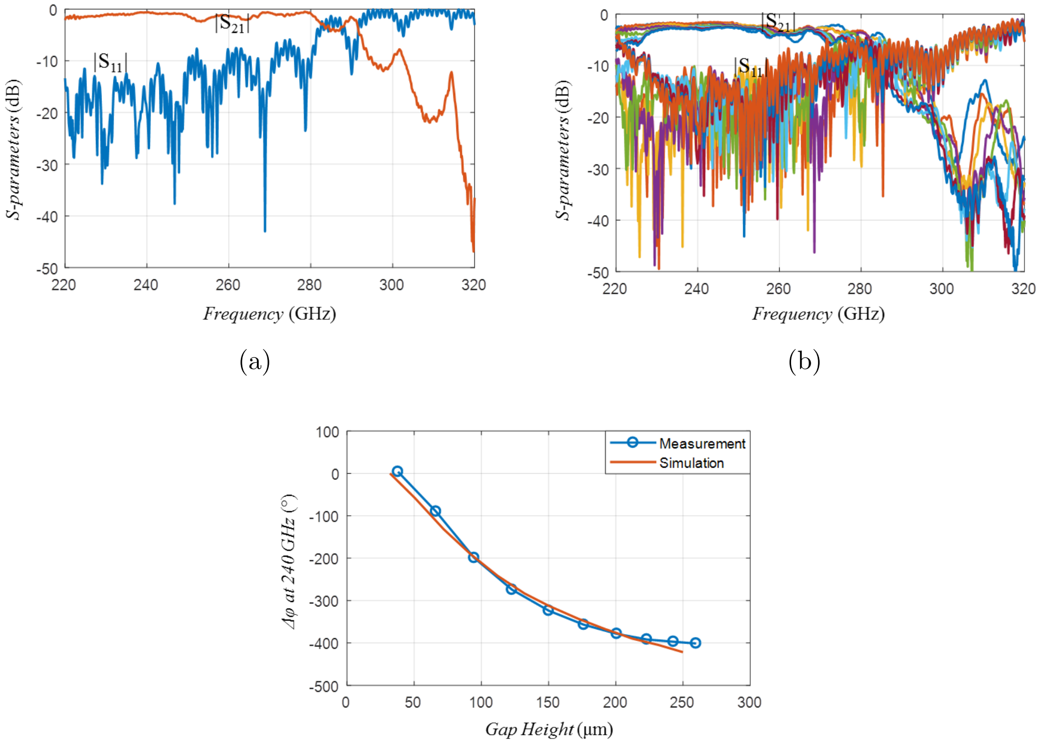

(a)

(b)

(c)

Figure 5.18: Measurement results of the phase shifter. (a) S-parameters with no aluminum frame. (b) S-parameters with aluminum frame at different gap heights. (c) Phase shift at 240 GHz versus gap height.

less than 10^o is observed. This value include both the effect of actuator fatigue as well as network analyzer phase drift with time. The network analyzer phase drift with time was monitored by taking measurements at a fixed actuation voltage every one hour for two days and is found to have fluctuations of about 10^o. Thus, the phase error due to actuator fatigue is probably much better than what is shown Fig.5.20.

Finally, a comparison between the proposed phase shifter and other state-of-the-art passive phase shifters operating beyond 60 GHz is presented in Table 5.1, [140], [149], [164]–[178]. The metric of comparison is what is called “Figure of Merit (FoM) “, which is defined as the

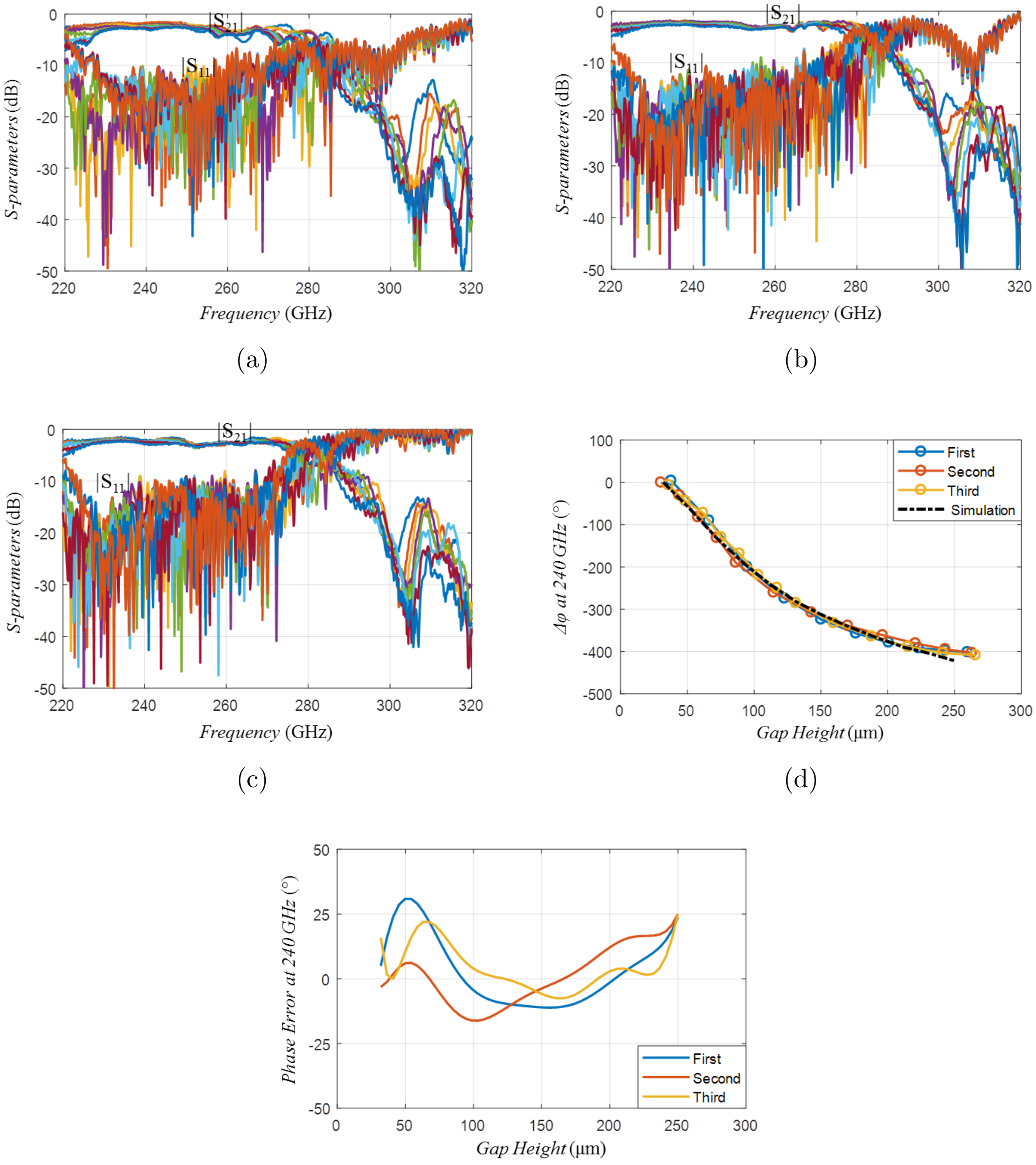

(a) (b)

(c) (d)

(e)

Figure 5.19: Optical slignment repeatability of the phase shifter. (a) S-parameters of first integration trial for different gap heights. (b) Second integration trial. (c) Third integration trial. (d) Phase shift at 240 GHz versus gap height for the three trials. (e) Phase error between measurement and simulation for the three trials.

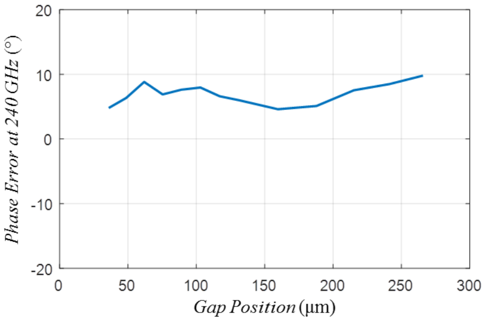

Figure 5.20: Phase error due to actuator fatigue.

maximum attainable phase shift divided by the maximum insertion loss. It describes the ability of the phase shifter to provide as much phase shift as possible with minimal insertion loss. The table includes technologies that use exotic materials like ferroelectric and liquid crystal materials. The dielectric constant of such materials can be changed through the application of external electric field. Being dielectric materials, they have associated dielectric losses, and the corresponding phase shifters usually have small FoM number. Integrated circuits based phase shifters on the other have the advantage of being compact in size, repeatable and consume low power. However, they also show small FoM. MEMS based phase shifters show relatively higher FoM numbers and have been demonstrated to frequencies up to 170 GHz. However, there is not a clear way of extending such performance to higher frequencies. A good review of MEMS based phase shifter can be found in [179]. Our proposed phase shifter shows a remarkable FoM of 127^o/dB. To the best of our knowledge, this is the best FoM performance reported for any passive phase shifter operating beyond 60 GHz. Furthermore, the performance of the phase shifter is expected to scale to higher frequencies in a strait forward manner.

Table 5.1: Comparison with passive state-of-the-art phase shifters operating at and beyond 60 GHz

Ref. #	Year	Type	Technology	Frequency (GHz)	Δφ (°)	Max Insertion Loss (dB)	Return Loss (dB)	FoM (°/dB)
[138]	2001	Analog	Ferroelectric material (BST) – Loaded TL	60	220	10	5.5	22
[146]	2015	Analog	Ferroelectric material (BST) – Loaded TL	60	150	5.9	12	25
[147]	2010	Analog	Liquid crystal material – Loaded TL	60	243	11.6	14	20
[162]	2011	Analog	Liquid crystal material – Loaded TL	65-97 (76)	92	2.4	15	38
[163]	2013	Analog	Liquid crystal material – Loaded TL	60	47	11	12	4
[164]	2009	Digital (4bits)	Integrated Circuits (BiCMOS) - TL loaded with switchable low pass networks	67-82 (77)	337	23	12	14.7
[165]	2009	Analog	Integrated Circuits (CMOS) - Reflection type with varactors reflective load	50-65 (65)	90	8	14	11.3
[166]	2011	Analog	Integrated Circuits (CMOS) - Reflection type with resonant reflective loads	50-65 (60)	180	8.3	15	21.7
[167]	2002	Digital (4bits)	MEMS - CPW distributed phase shifter with capacitive shunt switches	40-70 (65)	330	3.6	10	92
[168]	2004	Digital (4bits)	MEMS - CPW distributed phase shifter with capacitive shunt switches	75-110 (93)	342	4.2	15	81
[169]	2009	Digital (4.25 bits)	MEMS - CPW loaded with high resistivity silicon dielectric blocks	75-110 (110)	375	4	15	94
[170]	2011	Digital (2bits)	MEMS – CPW switched line	55-65 (60)	270	3	12	90
[171]	2013	Digital (1.5 bits)	MEMS – reflection type with bi-directional fishbone MEMS actuator as reflective load	55-65 (65)	144	3	14	48
[172]	2016	Digital (5-bits)	MEMS - Distributed CPW loaded with MEMS bridges	110-170 (140)	349	5.88	17	60
[173]	2013	Analog	Metallic fingers in a ridge waveguide	98	58	5.1	-	11.5
[174]	2014	Analog	loading a high-resistivity silicon image guide with piezoelectrically actuated dielectric slab	87-94(90)	85	2	15	42.5
[175]	2016	Digital (3.3 bits)	Rectangular waveguide loaded with MEMS reconfigurable E-plane Stubs	500-550 (500)	20	3	15	7
This Work		**Analog**	**Piezoelectric actuated, Tunable PMC in a rectangular waveguide**	**230-250**	**380**	**3**	**10**	**127**

5.4 Conclusions

A novel rectangular waveguide piezoelectric-based phase shifter suitable for sub-THz frequency range is designed, fabricated and measured. The phase shifter relies on mechanically actuating a metallic strip inside an upright rectangular waveguide to create a tunable artificial magnetic conductor boundary condition. By moving the metallic strip vertically inside the waveguide, its dispersion relation can be controlled leading to variable phase shift. An analytical model is introduced to calculate the dispersion relation and the corresponding phase shift performance. The model is verified using numerical simulation. Next, the phase shifter is designed on Ansys HFSS electromagnetic simulator and optimized for best insertion loss performance. Silicon microfabrication technology is used to fabricate the phase shifter where the structure is divided into two halves with each half fabricated on a separate 1mm thick silicon wafer. An external piezoelectric actuator is integrated with the phase shifter to provide the required vertical displacement. A phase shift of $380^o$is achieved at 240 GHz with displacement range of 40 - 200 μm above the bottom waveguide wall. The corresponding insertion loss showed an average value of about 2.25 dB and a return loss better than 10 dB. A FoM of 127^o/dB is measured for the phase shifter which is, to the best of the our knowledge, the best reported FoM for all passive phase shifters operating beyond 60 GHz. The phase shifter is designed to work at 240 GHz, but the design can be scaled to higher frequencies in a straight forward manner.

CHAPTER VI

Conclusions and Future Work

6.1 Summary and Conclusions

This thesis investigated the potential and performance limitations of using sub-THz radars at 240 GHz for short range applications. Three main research directions were pursued; modeling of radar environment, experimental measurement of radar targets, and hardware fabrication of some radar components. It began with the development of semi-numerical propagation model for long, discrete, sparse, two dimensional random media in Chapter 2. This type of random media can be used, in general, to model environment like rain, snow, or dust. The model is named Statistical S-matrix approach for Wave Propagation in Spectral Domain, or SSWaP-SD. In this model, the random medium is discretized into slabs with appropriate thickness, and each slab is represented by a high order bistatic scattering matrix. By cascading the scattering matrices of the individual slabs, the scattering matrix of the entire medium is calculated very efficiently. The model is a coherent one that can track both the magnitude and phase of the electromagnetic signal as it travels inside the random medium. The accuracy of the model is verified by comparison with full wave simulation combined with Monte Carlo analysis. An analytical expression is also developed for the special case of translationally invariant, discrete, sparse, random medium and is named Analytical SSWaP-SD or, ASSWaP-SD. The analytical model is used to accurately predict the dual-slope attenuation curve of such random media and to estimate the "knee point" after which the propagating wave becomes dominated by the incoherent component. The analytical model is then expanded and used to study the SAR resolution degradation in 2D sparse random medium in both cross-range and range directions. Appropriate correlation functions are defined to quantify the degradation in resolution. It is found that the degradation in the cross-range direction is severe and it gets worse as the imaging range increases until it saturates at a constant value. This value is related to the average center-to-center distance between a scatterer and its nearest neighbor which characterizes the scale at which the random medium can be considered translational invariant. Furthermore, the cross-range degradation increases with the surface fraction of the random medium. For the range resolution, however, it is found that the degradation is small even for a very large bandwidth. A novel method is proposed to reduce the speckle level of the SAR image without sacrificing the resolution at the end of the chapter.

The measurement research direction is covered in Chapter 3 and 4. Specifically, a network analyzer based dielectric measurement system working at J-band is reported in Chapter 3. The main objective is to report accurate measurements of the dielectric permittivity of different materials important for concealed object detection scenarios. For this purpose, different fabric materials under dry and wet conditions as well as human skin are reported. For the fabric materials, a free-space transmission only measurement procedure is used. The developed retrieval algorithm has the advantage of estimating both the complex dielectric constant as well as the sample thickness. It is shown that the dielectric constants of all the fabric materials considered are nearly the same under dry condition at the considered frequency band. For moist fabrics, the imaginary part of the complex permittivity increases significantly since it is dominated by the losses of the contained water. For in-vivo human skin dielectric measurement, a reflection measurement technique is used. A non-standard one-port calibration procedure is adapted to avoid issues associated with waveguide flange misalignment during calibration. In Chapter 4, a newly constructed polarimetric instrumentation radar operating at 222 GHz has been used to conduct a series of outdoor measurements on both bare and vegetation-covered surfaces. Substantial backscattering was observed from both bare and vegetation-covered surfaces along with significant depolarization (up to -4 dB). Bare surfaces such as dirt and asphalt are electrically rough surfaces at 222 GHz, and their subsurface aggregates have sizes that are comparable with wavelength resulting in substantial radar backscatter response. The value of the copolarized backscattering coefficients of bare surface seems to quickly reach to a "ceiling" level as the surface roughness increased, and its dependence on the incidence angle follows that of a Lambertian surface. Despite the physical differences between the measured vegetation-covered surfaces, their backscattering coefficients exhibited similar values and demonstrated weak angular dependence on incidence angle. A hybrid empirical model is proposed for bare surfaces that combines two semi-empirical MMW models developed earlier to predict surface scattering and volume scattering from bare surfaces. Another empirical model is developed for vegetation-covered surfaces based on the data presented in this chapter.

A novel rectangular waveguide piezoelectric-based phase shifter is presented in Chapter 5. The phase shifter is envisioned to be integrated in an electronic beam steering antenna at sub-THz frequencies. The design is optimized for minimal insertion loss performance. At the core of the design is a tunable artificial magnetic conductor that is realized by simply actuating a PEC strip against the short wall of the rectangular waveguide. This has the effect of changing the dispersion relation and consequently the phase shift through the proposed PMC loaded waveguide. An analytical formulation is presented to calculate the dispersion relation and good agreement with numerical simulation is obtained. A prototype is fabricated using silicon microfabrication techniques in the cleanroom. The waveguide is divided into two halves which are fabricated on two separate silicon wafers and then brought together into contact by mechanical pressure. The PEC strip is realized from Aluminum and is attached to an external piezoelectric actuator to proof the concept. A phase shift of $380^o$is achieved at 240 GHz with displacement of only 160 μm. The corresponding insertion loss showed an average value of about 2.25 dB and a return loss better than 10 dB. The phase shifter is designed to work at 240 GHz, but the design can be scaled to higher frequencies in a straight forward manner.

6.2 Future Work

Based on the work done in this thesis, many future research directions can be identified. For the modeling part, the proposed ASSWaP-SD technique can be expanded to the more realistic 3D rain case. The formulation can be extended in a straight forward manner, but the main problem is to verify the results against 3D full wave simulation as the simulation domain becomes huge. Another research direction that can be pursued is to adapt the technique to other types of random media, especially snow. Compared to rain, snow is a very dense random media that is governed by completely different statistics. However, it still can be treated as translationally invariant random media. One major challenge that comes to mind is how to obtain the bistatic scattering matrix of the individual snow slabs. A full wave simulation for the individual slabs is definitely an option, but faster methods are needed to yield an efficient solution.

As for the measurement part, we can say that we just scratched the surface in this thesis. Many measurement needs to be done if such a technology is to be used in driver-less cars, for example. This can include the measurement of RCS of different targets available in a typical road scene like vehicles, traffic signs, road shoulders, pavement curbs, ... etc. Near grazing angle (80^o to 90^o) RCS measurements of different road surfaces are also important as these are the typical angles of concern for forward looking radars in cars. Other interesting measurements include RCS comparison between an asphalt road with and without snow or rain. This kind of measurement is very important as it can be used to identify black ice on driving roads which is the cause of many car fatalities.

For the fabrication part, one extension of this work is to integrate the piezoelectric actuator in the fabrication process. In [180], a PZT piezoelectric actuator is fabricated and showed to achieve more than 430 μm with only 15V. If such actuator is integrated with our phase shifter in the same fabrication process, it will eliminate the external integration step and will lead to more reliable and repeatable design. This should not be a very difficult task since all of our fabrication steps are done at room temperature and will not deteriorate the PZT performance (PZT can work only up to 200^oC [160]). Another research direction is to use the phase shifter to realize electronic beam steering leaky wave antenna as conceptually depicted in Fig.6.1. The idea is to etch radiating slots in the top half of the waveguide to allow the electromagnetic wave to leak some of the energy as it experiences the phase shift inside the waveguide. For this design, a large phase shift between the consecutive radiating slots is required in order to steer the beam within a reasonable range ($\pm 45^o$, for example). This translates to increasing the separation between the slots. On the other hand, the spacing between the slots can not exceed $\lambda/2$ to avoid grating lobes. These two requirements can be

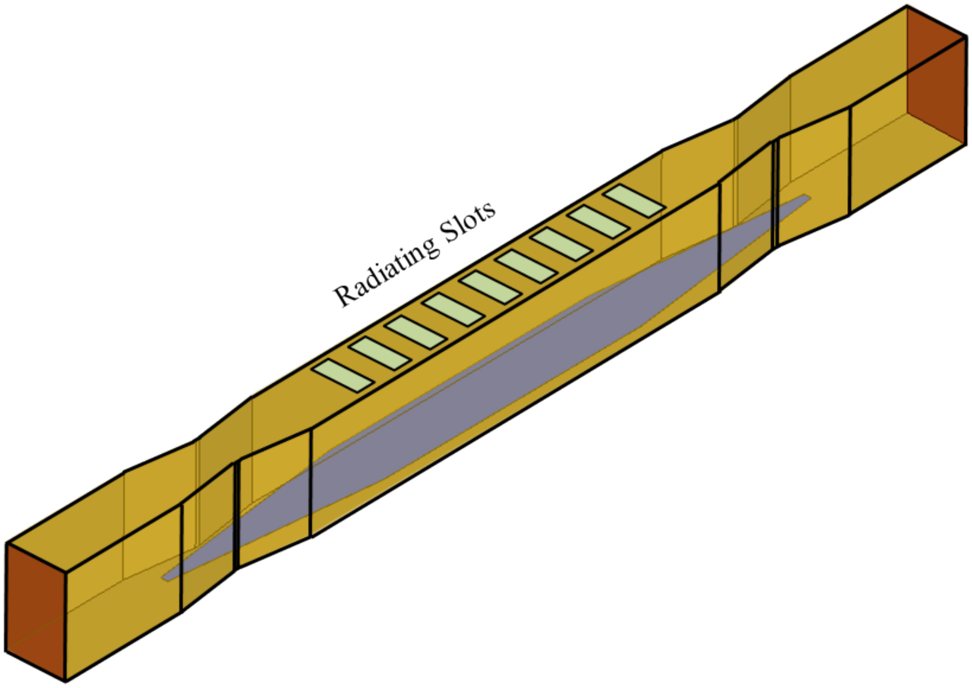

Figure 6.1: Possible electronic beam scanning leaky wave antenna concept using the proposed piezoelectric phase shifter.

simultaneously satisfied by meandering the waveguide, for example.

Bibliography

[1] F. T. Ulaby, D. G. Long, W. J. Blackwell, C. Elachi, A. K. Fung, C. Ruf, K. Sarabandi, H. A. Zebker, and J. Van Zyl, *Microwave radar and radiometric remote sensing.* University of Michigan Press Ann Arbor, 2014.

[2] M. I. Skolnik, *Introduction to radar systems.* McGraw Hill, 2001.

[3] B. R. Mahafza, *Radar systems analysis and design using MATLAB.* CRC press, 2002.

[4] I. F. Akyildiz, J. M. Jornet, and C. Han, "Terahertz band: Next frontier for wireless communications", *Physical Communication*, vol. 12, pp. 16–32, 2014.

[5] Y.-S. Lee, *Principles of terahertz science and technology.* Springer Science & Business Media, 2009, vol. 170.

[6] M. Tonouchi, "Cutting-edge terahertz technology", *Nature photonics*, vol. 1, no. 2, pp. 97–105, 2007.

[7] A. Rostami, H. Rasooli, and H. Baghban, *Terahertz technology: fundamentals and applications.* Springer Science & Business Media, 2010, vol. 77.

[8] B. Borden, *Radar imaging of airborne targets: A primer for applied mathematicians and physicists.* Taylor & Francis, 1999.

[9] E. Carey and S. Lidholm, *Millimeter-wave integrated circuits*. Springer Science & Business Media, 2005.

[10] L. A. Samoska, "An overview of solid-state integrated circuit amplifiers in the submillimeter-wave and THz regime", *IEEE Transactions on Terahertz Science and Technology*, vol. 1, no. 1, pp. 9–24, 2011.

[11] "International technology roadmap for semiconductors 2.0 2015 edition", Semiconductor Industry Assoc., Tech. Rep., 2015.

[12] H. Yu and Y. Shang, *Design of CMOS Millimeter-wave and Terahertz Integrated Circuits with Metamaterials*. CRC Press, 2015.

[13] W. Deal, X. B. Mei, K. M. K. H. Leong, V. Radisic, S. Sarkozy, and R. Lai, "THz monolithic integrated circuits using InP high electron mobility transistors", *IEEE Transactions on Terahertz Science and Technology*, vol. 1, no. 1, pp. 25–32, Sep. 2011.

[14] A. Tessmann, A. Leuther, V. Hurm, I. Kallfass, H. Massler, M. Kuri, M. Riessle, M. Zink, R. Loesch, M. Seelmann-Eggebert, M. Schlechtweg, and O. Ambacher, "Metamorphic HEMT MMICs and modules operating between 300 and 500 GHz", *IEEE Journal of Solid-State Circuits*, vol. 46, no. 10, pp. 2193–2202, Oct. 2011.

[15] M. Seo, M. Urteaga, A. Young, J. Hacker, A. Skalare, R. Lin, and M. Rodwell, "A single-chip 630 GHz transmitter with 210 GHz sub-harmonic PLL local oscillator in 130 nm InP HBT", in *Proc. IEEE/MTT-S Int. Microwave Symp. Digest*, Jun. 2012, pp. 1–3.

[16] A. M. Niknejad and H. Hashemi, *mm-Wave silicon technology: 60 GHz and beyond*. Springer Science & Business Media, 2008.

[17] J. D. Cressler and G. Niu, *Silicon-Germanium heterojunction bipolar transistors*. Artech house, 2002.

[18] R. Wang, Y. Sun, M. Kaynak, S. Beer, J. Borngräber, and J. C. Scheytt, “A micromachined double-dipole antenna for 122–140 GHz applications based on a SiGe BiCMOS technology”, in *2012 IEEE MTT-S International Microwave Symposium Digest (MTT)*, 2012, pp. 1–3.

[19] H. Rücker, B. Heinemann, and A. Fox, “Half-terahertz SiGe BiCMOS technology”, in *Silicon Monolithic Integrated Circuits in RF Systems (SiRF), 2012 IEEE 12th Topical Meeting on*, 2012, pp. 133–136.

[20] A. Ulusoy, S. Krone, G. Liu, A. Trasser, F. Guderian, B. Almeroth, A. Barghouthi, M. Hellfeld, S. Schumann, C. Carta, *et al.*, “A 60 GHz multi Gb/s system demonstrator utilizing analog synchronization and 1-bit data conversion”, in *2013 IEEE 13th Topical Meeting on Silicon Monolithic Integrated Circuits in RF Systems (SiRF)*, 2013, pp. 99–101.

[21] E. Öjefors, B. Heinemann, and U. R. Pfeiffer, “Subharmonic 220 and 320 GHz SiGe HBT receiver front-ends”, *IEEE Transactions on Microwave Theory and Techniques*, vol. 60, no. 5, pp. 1397–1404, 2012.

[22] E. Öjefors, J. Grzyb, Y. Zhao, B. Heinemann, B. Tillack, and U. R. Pfeiffer, “A 820 GHz SiGe chipset for terahertz active imaging applications”, in *2011 IEEE International Solid-State Circuits Conference Digest of Technical Papers (ISSCC)*, 2011, pp. 224–226.

[23] K. Sengupta and A. Hajimiri, “A 0.28 THz power-generation and beam-steering array in CMOS based on distributed active radiators”, *IEEE Journal of Solid-State Circuits*, vol. 47, no. 12, pp. 3013–3031, Dec. 2012.

[24] Y. Shang, H. Yu, C. Yang, Y. Liang, and W. M. Lim, “A 239 –281 GHz sub-THz imager with 100 MHz resolution by CMOS direct-conversion receiver with on-chip circular-polarized SIW antenna”, in *Proc. IEEE 2014 Custom Integrated Circuits Conf*, Sep. 2014, pp. 1–4.

[25] R. Han, Y. Zhang, Y. Kim, D. Y. Kim, H. Shichijo, E. Afshari, and O. Kenneth, “280 GHz and 860 GHz image sensors using Schottky-barrier diodes in 0.13 μm digital CMOS”, in *Proc. IEEE Int. Solid-State Circuits Conf*, Feb. 2012, pp. 254–256.

[26] T. Mitomo, N. Ono, H. Hoshino, Y. Yoshihara, O. Watanabe, and I. Seto, “A 77 GHz 90 nm CMOS transceiver for FMCW radar applications”, *IEEE Journal of Solid-State Circuits*, vol. 45, no. 4, pp. 928–937, Apr. 2010.

[27] B. H. Ku, P. Schmalenberg, O. Inac, O. D. Gurbuz, J. S. Lee, K. Shiozaki, and G. M. Rebeiz, “A 77–81-GHz 16-element phased-array receiver with beam scanning for advanced automotive radars”, *IEEE Transactions on Microwave Theory and Techniques*, vol. 62, no. 11, pp. 2823–2832, Nov. 2014.

[28] M. A. Henawy and M. Schneider, “Integrated antennas in eWLB packages for 77 GHz and 79 GHz automotive radar sensors”, in *Proc. 41st European Microwave Conf*, Oct. 2011, pp. 1312–1315.

[29] F. Schuster, H. Videlier, A. Dupret, D. Coquillat, M. Sakowicz, J. P. Rostaing, M. Tchagaspanian, B. Giffard, and W. Knap, “A broadband THz imager in a low-cost

CMOS technology", in *Proc. IEEE Int. Solid-State Circuits Conf*, Feb. 2011, pp. 42–43.

[30] R. Carrillo-Ramirez and R. W. Jackson, "A highly integrated millimeter-wave active antenna array using BCB and silicon substrate", *IEEE Transactions on Microwave Theory and Techniques*, vol. 52, no. 6, pp. 1648–1653, Jun. 2004.

[31] H. Sherry, R. A. Hadi, J. Grzyb, E. Ojefors, A. Cathelin, A. Kaiser, and U. R. Pfeiffer, "Lens-integrated THz imaging arrays in 65nm CMOS technologies", in *Proc. IEEE Radio Frequency Integrated Circuits Symp*, Jun. 2011, pp. 1–4.

[32] Y. A. Atesal, B. Cetinoneri, M. Chang, R. Alhalabi, and G. M. Rebeiz, "Millimeter-wave wafer-scale silicon BiCMOS power amplifiers using free-space power combining", *IEEE Transactions on Microwave Theory and Techniques*, vol. 59, no. 4, pp. 954–965, Apr. 2011.

[33] J. Hasch, E. Topak, R. Schnabel, T. Zwick, R. Weigel, and C. Waldschmidt, "Millimeter-wave technology for automotive radar sensors in the 77 GHz frequency band", *IEEE Transactions on Microwave Theory and Techniques*, vol. 60, no. 3, pp. 845–860, Mar. 2012.

[34] *Federal communications commission, fcc 47 cfr, section 15.515.*

[35] B. Y. Kapilevich, S. W. Harmer, and N. J. Bowring, *Non-Imaging Microwave and Millimetre-Wave Sensors for Concealed Object Detection.* CRC Press, 2014.

[36] J. W. Lamb, "Miscellaneous data on materials for millimetre and submillimetre optics", *International Journal of Infrared and Millimeter Waves*, vol. 17, no. 12, pp. 1997–2034, 1996.

[37] A. A. Ibrahim and K. Sarabandi, “Sub-terahertz dielectric measurement and its application to concealed object detection”, *IEEE Transactions on Terahertz Science and Technology*, vol. 5, no. 3, pp. 445–455, May 2015.

[38] T. Bryllert, K. B. Cooper, R. J. Dengler, N. Llombart, G. Chattopadhyay, E. Schlecht, J. Gill, C. Lee, A. Skalare, I. Mehdi, and P. H. Siegel, “A 600 GHz imaging radar for concealed objects detection”, in *Proc. IEEE Radar Conf*, May 2009, pp. 1–3.

[39] T. Jaeschke, C. Bredendiek, and N. Pohl, “A 240 GHz ultra-wideband FMCW radar system with on-chip antennas for high resolution radar imaging”, in *Proc. IEEE MTT-S Int. Microwave Symp. Digest (MTT)*, Jun. 2013, pp. 1–4.

[40] K. B. Cooper, R. J. Dengler, N. Llombart, B. Thomas, G. Chattopadhyay, and P. H. Siegel, “THz imaging radar for standoff personnel screening”, *IEEE Transactions on Terahertz Science and Technology*, vol. 1, no. 1, pp. 169–182, Sep. 2011.

[41] Y. Alvarez, R. Camblor, C. Garcia, J. Laviada, C. Vazquez, S. Ver-Hoeye, G. Hotopan, M. Fernandez, A. Hadarig, A. Arboleya, and F. Las-Heras, “Submillimeter-wave frequency scanning system for imaging applications”, *IEEE Transactions on Antennas and Propagation*, vol. 61, no. 11, pp. 5689–5696, Nov. 2013.

[42] S. Stanko, S. Palm, R. Sommer, F. Kloppel, M. Caris, and N. Pohl, “Millimeter resolution SAR imaging of infrastructure in the lower THz region using MIRANDA-300”, in *Proc. 46th European Microwave Conf. (EuMC)*, Oct. 2016, pp. 1505–1508.

[43] M. Moallem and K. Sarabandi, “Polarimetric study of MMW imaging radars for indoor navigation and mapping”, *IEEE Transactions on Antennas and Propagation*, vol. 62, no. 1, pp. 500–504, Jan. 2014.

[44] F. Nava, C. J. Scheytt, T. Zwick, M. Pauli, B. Göttel, and W. Winkler, “Ultra-compact 122 GHz radar sensor for autonomous aircrafts”, *Procedia Technology*, vol. 26, pp. 399–404, 2016.

[45] A. Pagels, M. Hagelen, G. Briese, and A. Tessmann, “Helicopter assisted landing system-millimeter-wave against brown-out”, in *Microwave Conference, 2009 German*, IEEE, 2009, pp. 1–3.

[46] G. Galati, E. G. Piracci, and M. Ferri, “High resolution, millimeter-wave radar applications to airport safety”, in *2016 8th International Conference on Ultrawideband and Ultrashort Impulse Signals (UWBUSIS)*, IEEE, 2016, pp. 21–26.

[47] M. Klenner, C. Zech, A. Hülsmann, J. Kühn, M. Schlechtweg, K. Hahmann, B. Kleiner, M. Ulrich, and O. Ambacher, “A portable W-band radar system for enhancement of infrared vision in fire fighting operations”, in *SPIE Security+ Defence*, International Society for Optics and Photonics, 2016, pp. 999 307–999 307.

[48] V. W. Richard, J. E. Kammerer, and H. B. Wallace, “Rain backscatter measurements at millimeter wavelengths”, *IEEE Transactions on Geoscience and Remote Sensing*, vol. 26, no. 3, pp. 244–252, May 1988.

[49] J. Nemarich, R. J. Wellman, and J. Lacombe, “Backscatter and attenuation by falling snow and rain at 96, 140, and 225 GHz”, *IEEE Transactions on Geoscience and Remote Sensing*, vol. 26, no. 3, pp. 319–329, May 1988.

[50] J. B. Mead and R. E. McIntosh, “Polarimetric backscatter measurements of deciduous and coniferous trees at 225 GHz”, *IEEE Transactions on Geoscience and Remote Sensing*, vol. 29, no. 1, pp. 21–28, Jan. 1991.

[51] J. B. Mead, P. M. Langlois, P. S. Chang, and R. E. McIntosh, "Polarimetric scattering from natural surfaces at 225 GHz", *IEEE Transactions on Antennas and Propagation*, vol. 39, no. 9, pp. 1405–1411, Sep. 1991.

[52] J. B. Mead, P. S. Chang, S. P. Lohmeier, P. M. Langlois, and R. McIntosh, "Polarimetric observations and theory of millimeter-wave backscatter from snow cover", *IEEE Transactions on Antennas and Propagation*, vol. 41, no. 1, pp. 38–46, Jan. 1993.

[53] A. Ishimaru, *Wave propagation and scattering in random media*. New York: Academic press, 1978, vol. 1-2.

[54] A. Tavakoli, K. Sarabandi, and F. Ulaby, "Microwave propagation constant for a vegetation canopy at X band", *Radio Science*, vol. 28, no. 04, pp. 549–558, Jul. 1993.

[55] L. L. Foldy, "The multiple scattering of waves", *Physical Review*, vol. 67, no. 3-4, pp. 107–119, 1945.

[56] L. Tsang, J. A. Kong, and K.-H. Ding, *Scattering of Electromagnetic Waves: Theories and Applications*. New York:Wiley, 2000.

[57] F. T. Ulaby, K. Sarabandi, K. Mcdonald, M. Whitt, and M. C. Dobson, "Michigan microwave canopy scattering model", *International Journal of Remote Sensing*, vol. 11, no. 7, pp. 1223–1253, 1990.

[58] Y.-C. Lin and K. Sarabandi, "A monte Carlo coherent scattering model for forest canopies using fractal-generated trees", *IEEE Transactions on Geoscience and Remote Sensing*, vol. 37, no. 1, pp. 440–451, Jan. 1999.

[59] J.-P. Fouque, J. Garnier, G. Papanicolaou, and K. Solna, *Wave propagation and time reversal in randomly layered media*. Springer Science & Business Media, 2007, vol. 56.

[60] F. K. Schwering, E. J. Violette, and R. H. Espeland, “Millimeter-wave propagation in vegetation: Experiments and theory”, *IEEE Transactions on Geoscience and Remote Sensing*, vol. 26, no. 3, pp. 355–367, May 1988.

[61] R. K. Tewari, S. Swarup, and M. N. Roy, “Radio wave propagation through rain forests of India”, *IEEE Transactions on Antennas and Propagation*, vol. 38, no. 4, pp. 433–449, Apr. 1990.

[62] F. Wang and K. Sarabandi, “A physics-based statistical model for wave propagation through foliage”, *IEEE Transactions on Antennas and Propagation*, vol. 55, no. 3, pp. 958–968, Mar. 2007.

[63] A. A. Ibrahim and K. Sarabandi, “Simulation of long distance wave propagation in 2-D sparse random media: A statistical S-matrix approach in spectral domain”, *IEEE Transactions on Antennas and Propagation*, vol. 62, no. 5, pp. 2708–2720, May 2014.

[64] ——, “Evaluation of SAR performance degradation in sparse random media: An analytical study with 2-D scatterers”, *IEEE Transactions on Antennas and Propagation*, vol. 62, no. 10, pp. 5219–5229, Oct. 2014.

[65] ——, “Simulation of wave propagation in 2D sparse random media at millimeter-wave frequencies”, in *Proc. IEEE Antennas and Propagation Society Int. Symp. (APSURSI)*, Jul. 2014, pp. 1562–1563.

[66] ——, “SAR resolution degradation estimation operating in sparse random media at millimeter-wave frequencies”, in *Proc. IEEE Geoscience and Remote Sensing Symp*, Jul. 2014, pp. 1113–1116.

[67] G. R. Simpson, “A generalized n-port cascade connection”, in *Proc. IEEE MTT-S Int. Microwave Symp. Digest*, Jun. 1981, pp. 507–509.

[68] K. Okamoto, *Fundamentals of optical waveguides*. Academic press, 2010.

[69] J. Saijonmaa and D. Yevick, "Beam-propagation analysis of loss in bent optical waveguides and fibers", *Journal of Optical Society of America*, vol. 73, no. 12, pp. 1785–1791, 1983.

[70] S.-C. Lee, "Dependent scattering of an obliquely incident plane wave by a collection of parallel cylinders", *Journal of Applied Physics*, vol. 68, no. 10, pp. 4952–4957, 1990.

[71] P. Bansal and A. J. Ardell, "Average nearest-neighbor distances between uniformly distributed finite particles", *Metallography*, vol. 5, no. 2, pp. 97–111, 1972.

[72] K. Sarabandi and P. R. Siqueira, "Numerical scattering analysis for two-dimensional dense random media: Characterization of effective permittivity", *IEEE Transactions on Antennas and Propagation*, vol. 45, no. 5, pp. 858–867, May 1997.

[73] L. Tsang, J. A. Kong, K.-H. Ding, and C. O. Ao, *Scattering of Electromagnetic Waves: Numerical Simulations*. New York:Wiley, 2001.

[74] S. Haykin, *Communication Systems*, 4th edition. New York: Wiley, 2001.

[75] D. M. Pozar, *Microwave engineering*, 3rd. New York: Wiley, 2005.

[76] L. Tsang and J. A. Kong, *Scattering of Electromagnetic Waves: Advanced Topics*. New York:Wiley, 2001, vol. 26.

[77] M. Mishchenko, "Enhanced backscattering of polarized light from discrete random media: Calculations in exactly the backscattering direction", *Journal of Optical Society of America A*, vol. 9, no. 6, pp. 978–982, 1992.

[78] H. Mott, *Remote Sensing with Polarimetric Radar*. New Jersey: Wiley, 2007.

[79] J. C. Souyris, C. Henry, and F. Adragna, “On the use of complex SAR image spectral analysis for target detection: Assessment of polarimetry”, *IEEE Transactions on Geoscience and Remote Sensing*, vol. 41, no. 12, pp. 2725–2734, Dec. 2003.

[80] M. Soumekh, “Automatic aircraft landing using interferometric inverse synthetic aperture radar imaging”, *IEEE Transactions on Image Processing*, vol. 5, no. 9, pp. 1335–1345, Sep. 1996.

[81] M. S. Moran, D. C. Hymer, J. Qi, and E. E. Sano, “Soil moisture evaluation using multi-temporal synthetic aperture radar (SAR) in semiarid rangeland”, *Agricultural and Forest meteorology*, vol. 105, no. 1, pp. 69–80, 2000.

[82] M. Dehmollaian and K. Sarabandi, “Refocusing through building walls using synthetic aperture radar”, *IEEE Transactions on Geoscience and Remote Sensing*, vol. 46, no. 6, pp. 1589–1599, Jun. 2008.

[83] G. Gouesbet and G. Gréhan, *Generalized Lorenz-Mie Theories.* Berlin, Germany: Springer, 2011.

[84] L.-F. Chen, C. Ong, C. Neo, V. Varadan, and V. K. Varadan, *Microwave electronics: measurement and materials characterization.* U.K.: Wiley, 2004.

[85] L. Duvillaret, F. Garet, and J. L. Coutaz, “A reliable method for extraction of material parameters in terahertz time-domain spectroscopy”, *IEEE Journal of Selected Topics in Quantum Electronics*, vol. 2, no. 3, pp. 739–746, Sep. 1996.

[86] L. Duvillaret, F. Garet, and J.-L. Coutaz, “Highly precise determination of optical constants and sample thickness in terahertz time-domain spectroscopy”, *Applied optics*, vol. 38, no. 2, pp. 409–415, 1999.

[87] T. D. Dorney, R. G. Baraniuk, and D. M. Mittleman, “Material parameter estimation with terahertz time-domain spectroscopy”, *Journal of Optical Society of America A*, vol. 18, no. 7, pp. 1562–1571, 2001.

[88] P. H. Bolivar, M. Brucherseifer, J. G. Rivas, R. Gonzalo, I. Ederra, A. L. Reynolds, M. Holker, and P. de Maagt, “Measurement of the dielectric constant and loss tangent of high dielectric-constant materials at terahertz frequencies”, *IEEE Transactions on Microwave Theory and Techniques*, vol. 51, no. 4, pp. 1062–1066, Apr. 2003.

[89] W. Withayachumnankul, B. M. Fischer, H. Lin, and D. Abbott, “Uncertainty in terahertz time-domain spectroscopy measurement”, *Journal of Optical Society of America B*, vol. 25, no. 6, pp. 1059–1072, 2008.

[90] W. L. Chan, J. Deibel, and D. M. Mittleman, “Imaging with terahertz radiation”, *Reports on progress in physics*, vol. 70, no. 8, pp. 1325–1379, 2007.

[91] I. Dunayevskiy, B. Bortnik, K. Geary, R. Lombardo, M. Jack, and H. Fetterman, “Millimeter-and submillimeter-wave characterization of various fabrics”, *Applied optics*, vol. 46, no. 24, pp. 6161–6165, 2007.

[92] J. E. Bjarnason, T. L. J. Chan, A. W. M. Lee, M. A. Celis, and E. R. Brown, “Millimeter-wave, terahertz, and mid-infrared transmission through common clothing”, *Applied Physics Letters*, vol. 85, no. 4, pp. 519–521, 2004.

[93] R. Appleby and H. B. Wallace, “Standoff detection of weapons and contraband in the 100 GHz to 1 THz region”, *IEEE Transactions on Antennas and Propagation*, vol. 55, no. 11, pp. 2944–2956, Nov. 2007.

[94] M. Vahidpour and K. Sarabandi, "Millimeter-wave doppler spectrum and polarimetric response of walking bodies", *IEEE Transactions on Geoscience and Remote Sensing*, vol. 50, no. 7, pp. 2866–2879, Jul. 2012.

[95] A. A. Ibrahim, A. Y. Nashashibi, and K. Sarabandi, "Dielectric characterization of thin materials at 240 GHz", in *Proc. IEEE Antennas and Propagation Society Int. Symp. (APSURSI)*, Jul. 2013, pp. 710–711.

[96] G. L. Friedsam and E. M. Biebl, "A broadband free-space dielectric properties measurement system at millimeter wavelengths", *IEEE Transactions on Instrumentation and Measurement*, vol. 46, no. 2, pp. 515–518, Apr. 1997.

[97] D. K. Ghodgaonkar, V. V. Varadan, and V. K. Varadan, "A free-space method for measurement of dielectric constants and loss tangents at microwave frequencies", *IEEE Transactions on Instrumentation and Measurement*, vol. 38, no. 3, pp. 789–793, Jun. 1989.

[98] J. Munoz, M. Rojo, A. Parrefio, and J. Margineda, "Automatic measurement of permittivity and permeability at microwave frequencies using normal and oblique free-wave incidence with focused beam", *IEEE Transactions on Instrumentation and Measurement*, vol. 47, no. 4, pp. 886–892, Aug. 1998.

[99] J. Baker-Jarvis, R. G. Geyer, and P. D. Domich, "A nonlinear least-squares solution with causality constraints applied to transmission line permittivity and permeability determination", *IEEE Transactions on Instrumentation and Measurement*, vol. 41, no. 5, pp. 646–652, Oct. 1992.

[100] C. Bourlier, N. Pinel, and G. Kubické, *Method of moments for 2D scattering problems: basic concepts and applications.* Wiley-ISTE, 2013.

[101] M. N. Afsar, I. I. Tkachov, and K. N. Kocharyan, "A novel W-band spectrometer for dielectric measurements", *IEEE Transactions on Microwave Theory and Techniques*, vol. 48, no. 12, pp. 2637–2643, Dec. 2000.

[102] Y. Lau, "Understanding the residual waveguide interface variations on millimeter wave calibration", in *Proc. 76th ARFTG Microwave Measurement Conf*, Nov. 2010, pp. 1–14.

[103] D. F. Williams, "500 GHz –750 GHz rectangular-waveguide vector-network-analyzer calibrations", *IEEE Transactions on Terahertz Science and Technology*, vol. 1, no. 2, pp. 364–377, Nov. 2011.

[104] Z. Liu and R. M. Weikle, "A reflectometer calibration method resistant to waveguide flange misalignment", *IEEE Transactions on Microwave Theory and Techniques*, vol. 54, no. 6, pp. 2447–2452, Jun. 2006.

[105] Z. Shen, C. L. Law, and R. H. MacPhie, "Application of anisotropic PML in mode-matching analysis of open-ended waveguides", *IEEE Transactions on Magnetics*, vol. 38, no. 2, pp. 733–736, Mar. 2002.

[106] K. J. Bois, A. D. Benally, and R. Zoughi, "Multimode solution for the reflection properties of an open-ended rectangular waveguide radiating into a dielectric half-space: The forward and inverse problems", *IEEE Transactions on Instrumentation and Measurement*, vol. 48, no. 6, pp. 1131–1140, Dec. 1999.

[107] C. Gabriel, "Compilation of the dielectric properties of body tissues at RF and microwave frequencies.", DTIC Document, Tech. Rep., 1996.

[108] A. Y. Nashashibi, A. A. Ibrahim, S. Cook, and K. Sarabandi, "Experimental characterization of the radar backscatter response of natural surfaces at 222 GHz", in *Proc.*

IEEE Int. Geoscience and Remote Sensing Symp. (IGARSS), Jul. 2015, pp. 2771–2773.

[109] ——, “Polarimetric backscatter response of targets at high millimeter-wave frequencies”, in *Proc. USNC-URSI Radio Science Meeting (Joint with AP-S Symp.)*, Jul. 2015, p. 285.

[110] ——, “Experimental characterization of polarimetric radar backscatter response of distributed targets at high millimeter-wave frequencies”, *IEEE Transactions on Geoscience and Remote Sensing*, vol. 54, no. 2, pp. 1013–1024, Feb. 2016.

[111] A. H. F. Van Vliet and T. De Graauw, “Quarter wave plates for submillimeter wavelengths”, *International Journal of Infrared and Millimeter Waves*, vol. 2, no. 3, pp. 465–477, 1981.

[112] A. Nashashibi, K. Sarabandi, and F. T. Ulaby, “A calibration technique for polarimetric coherent-on-receive radar systems”, *IEEE Transactions on Antennas and Propagation*, vol. 43, no. 4, pp. 396–404, Apr. 1995.

[113] S. A. Maas, *Microwave mixers*, 2nd. Norwood, MA: Artech House, 1993.

[114] I. Mehdi, S. M. Marazita, D. A. Humphrey, T.-H. Lee, R. J. Dengler, J. E. Oswald, A. J. Pease, S. C. Martin, W. L. Bishop, T. W. Crowe, and P. H. Siegel, “Improved 240-GHz subharmonically pumped planar Schottky diode mixers for space-borne applications”, *IEEE Transactions on Microwave Theory and Techniques*, vol. 46, no. 12, pp. 2036–2042, Dec. 1998.

[115] M. Moallem and K. Sarabandi, “Miniaturized-element frequency selective surfaces for millimeter-wave to terahertz applications”, *IEEE Transactions on Terahertz Science and Technology*, vol. 2, no. 3, pp. 333–339, May 2012.

[116] K. Sarabandi, F. T. Ulaby, and M. A. Tassoudji, “Calibration of polarimetric radar systems with good polarization isolation”, *IEEE Transactions on Geoscience and Remote Sensing*, vol. 28, no. 1, pp. 70–75, Jan. 1990.

[117] K. Sarabandi and F. T. Ulaby, “A convenient technique for polarimetric calibration of single-antenna radar systems”, *IEEE Transactions on Geoscience and Remote Sensing*, vol. 28, no. 6, pp. 1022–1033, Nov. 1990.

[118] F. T. Ulaby, A. Nashashibi, A. El-Rouby, E. S. Li, R. D. D. Roo, K. Sarabandi, R. J. Wellman, and H. B. Wallace, “95-GHz scattering by terrain at near-grazing incidence”, *IEEE Transactions on Antennas and Propagation*, vol. 46, no. 1, pp. 3–13, Jan. 1998.

[119] E. F. Knott, *Radar cross section measurements.* Springer Science & Business Media, 2012.

[120] F. T. Ulaby, K. Sarabandi, and A. Nashashibi, “Statistical properties of the mueller matrix of distributed targets”, *IEE Proceedings F-Radar and Signal Processing*, vol. 139, no. 2, pp. 136–146, Apr. 1992.

[121] K. Sarabandi, E. S. Li, and A. Nashashibi, “Modeling and measurements of scattering from road surfaces at millimeter-wave frequencies”, *IEEE Transactions on Antennas and Propagation*, vol. 45, no. 11, pp. 1679–1688, 1997.

[122] E. S. Li and K. Sarabandi, “Low grazing incidence millimeter-wave scattering models and measurements for various road surfaces”, *IEEE Transactions on Antennas and Propagation*, vol. 47, no. 5, pp. 851–861, May 1999.

[123] A. Nashashibi, F. T. Ulaby, and K. Sarabandi, “Measurement and modeling of the millimeter-wave backscatter response of soil surfaces”, *IEEE Transactions on Geoscience and Remote Sensing*, vol. 34, no. 2, pp. 561–572, Mar. 1996.

[124] A. Y. Nashashibi, K. Sarabandi, F. A. Al-Zaid, and S. Alhumaidi, “Characterization of radar backscatter response of sand-covered surfaces at millimeter-wave frequencies”, *IEEE Transactions on Geoscience and Remote Sensing*, vol. 50, no. 6, pp. 2345–2354, Jun. 2012.

[125] ——, “An empirical model of volume scattering from dry sand-covered surfaces at millimeter-wave frequencies”, *IEEE Transactions on Geoscience and Remote Sensing*, vol. 51, no. 6, pp. 3673–3682, Jun. 2013.

[126] A. K. Fung and K. S. Chen, *Microwave scattering and emission models for users.* Norwood, MA: Artech house, 2009.

[127] N. Fourikis, *Advanced array systems, applications and RF technologies.* Academic Press, 2000.

[128] D. Liu, U. Pfeiffer, J. Grzyb, and B. Gaucher, *Advanced millimeter-wave technologies: antennas, packaging and circuits.* John Wiley & Sons, 2009.

[129] B. Glance, “A fast low-loss microstrip p-i-n phase shifter”, *IEEE Transactions on Microwave Theory and Techniques*, vol. 27, no. 1, pp. 14–16, Jan. 1979.

[130] V. Sokolov, J. J. Geddes, A. Contolatis, P. E. Bauhahn, and C. Chao, “A Ka-band GaAs monolithic phase shifter”, *IEEE Transactions on Microwave Theory and Techniques*, vol. 31, no. 12, pp. 1077–1083, Dec. 1983.

[131] H. A. Atwater, “Circuit design of the loaded-line phase shifter”, *IEEE Transactions on Microwave Theory and Techniques*, vol. 33, no. 7, pp. 626–634, Jul. 1985.

[132] C.-L. Chen, W. E. Courtney, L. J. Mahoney, M. J. Manfra, A. Chu, and H. A. Atwater, “A low-loss Ku-band monolithic analog phase shifter”, *IEEE Transactions on Microwave Theory and Techniques*, vol. 35, no. 3, pp. 315–320, Mar. 1987.

[133] P. R. Shepherd and M. J. Cryan, “Schottky diodes for analogue phase shifters in GaAs MMICs”, *IEEE Transactions on Microwave Theory and Techniques*, vol. 44, no. 11, pp. 2112–2116, Nov. 1996.

[134] A. Megej and V. F. Fusco, “Low-loss analog phase shifter using varactor diodes”, *Microwave and Optical Technology Letters*, vol. 19, no. 6, pp. 384–386, Dec. 1998.

[135] A. S. Nagra and R. A. York, “Distributed analog phase shifters with low insertion loss”, *IEEE Transactions on Microwave Theory and Techniques*, vol. 47, no. 9, pp. 1705–1711, Sep. 1999.

[136] C. Jin, E. Okada, M. Faucher, D. Ducatteau, M. Zaknoune, and D. Pavlidis, “A GaN Schottky diode-based analog phase shifter MMIC”, in *Proc. 9th European Microwave Integrated Circuit Conf*, Oct. 2014, pp. 96–99.

[137] J. A. Higgins, H. Xin, A. Sailer, and M. Rosker, “Ka-band waveguide phase shifter using tunable electromagnetic crystal sidewalls”, *IEEE transactions on microwave theory and techniques*, vol. 51, no. 4, pp. 1281–1288, 2003.

[138] T.-Y. Yun and K. Chang, “Piezoelectric-transducer-controlled tunable microwave circuits”, *IEEE Transactions on Microwave Theory and Techniques*, vol. 50, no. 5, pp. 1303–1310, May 2002.

[139] Y. Poplavko, V. Kazmirenko, Y. Prokopenko, M. Jeong, and S. Baik, “Low loss phase shifter based on piezo-controlled layered dielectric structure”, in *Proc. IEEE MTT-S Int. Microwave Symp. Digest*, vol. 1, Jun. 2003, 437–440 vol.1.

[140] N. Somjit, G. Stemme, and J. Oberhammer, “Binary-coded 4.25-bit w-band monocrystalline-silicon MEMS multistage dielectric-block phase shifters”, *IEEE Transactions on Microwave Theory and Techniques*, vol. 57, no. 11, pp. 2834–2840, Nov. 2009.

[141] ——, “Deep-reactive-ion-etched wafer-scale-transferred all-silicon dielectric-block millimeter-wave MEMS phase shifters”, *Journal of Microelectromechanical Systems*, vol. 19, no. 1, pp. 120–128, Feb. 2010.

[142] J.-H. Park, H.-T. Kim, K. Kang, Y. Kwon, and Y.-K. Kim, “A micromachined millimeter wave phase shifter using semi-lumped elements”, in *Transducers 01 Eurosensors XV*, Springer, 2001, pp. 1524–1527.

[143] N. S. Barker and G. M. Rebeiz, “Optimization of distributed MEMS transmission-line phase shifters-U-band and W-band designs”, *IEEE Transactions on Microwave Theory and Techniques*, vol. 48, no. 11, pp. 1957–1966, Nov. 2000.

[144] A. Tagantsev, V. Sherman, K. Astafiev, J. Venkatesh, and N. Setter, “Ferroelectric materials for microwave tunable applications”, *Journal of electroceramics*, vol. 11, no. 1-2, pp. 5–66, 2003.

[145] P. Kužel, F. Kadlec, H. Němec, R. Ott, E. Hollmann, and N. Klein, “Dielectric tunability of SrTiO3 thin films in the terahertz range”, *Applied physics letters*, vol. 88, no. 10, p. 102 901, 2006.

[146] S. Mueller, C. Felber, P. Scheele, M. Wittek, C. Hock, and R. Jakoby, “Passive tunable liquid crystal finline phase shifter for millimeter waves”, in *2005 European Microwave Conference*, vol. 1, Oct. 2005, 4 pp.-.

[147] S. Mueller, F. Goelden, P. Scheele, M. Wittek, C. Hock, and R. Jakoby, “Passive phase shifter for W-band applications using liquid crystals”, in *Proc. European Microwave Conf*, Sep. 2006, pp. 306–309.

[148] S. Bulja and D. Mirshekar-Syahkal, “Meander line millimetre-wave liquid crystal based phase shifter”, *Electronics Letters*, vol. 46, no. 11, pp. 769–771, May 2010.

[149] C. Fritzsch, F. Giacomozzi, O. H. Karabey, F. Goelden, A. Moessinger, S. Bildik, S. Colpo, and R. Jakoby, “Continuously tunable W-band phase shifter based on liquid crystals and MEMS technology”, in *2011 41st European Microwave Conference*, Oct. 2011, pp. 1083–1086.

[150] F.-R. Yang, K.-P. Ma, Y. Qian, and T. Itoh, “A novel TEM waveguide using uniplanar compact photonic-bandgap (UC-PBG) structure”, *IEEE Transactions on Microwave Theory and Techniques*, vol. 47, no. 11, pp. 2092–2098, Nov. 1999.

[151] M. N. M. Kehn, M. Nannetti, A. Cucini, S. Maci, and P. S. Kildal, “Analysis of dispersion in dipole-FSS loaded hard rectangular waveguide”, *IEEE Transactions on Antennas and Propagation*, vol. 54, no. 8, pp. 2275–2282, Aug. 2006.

[152] N. Markuvitz, *Waveguide Handbook*. The Institution of Engineering and Technology, 1986.

[153] M. Guglielmi and A. A. Oliner, “Multimode network description of a planar periodic metal-strip grating at a dielectric interface–Part I: Rigorous network formulations”, *IEEE Transactions on Microwave Theory and Techniques*, vol. 37, no. 3, pp. 534–541, Mar. 1989.

[154] O. Luukkonen, C. Simovski, G. Granet, G. Goussetis, D. Lioubtchenko, A. V. Raisanen, and S. A. Tretyakov, “Simple and accurate analytical model of planar grids and

high-impedance surfaces comprising metal strips or patches", *IEEE Transactions on Antennas and Propagation*, vol. 56, no. 6, pp. 1624–1632, Jun. 2008.

[155] S. Makino, T. Moroya, S. Betsudan, K. Itoh, K. Noguchi, and T. Hirota, "PMC characteristics of capacitance grid with metal plate", in *2012 IEEE-APS Topical Conference on Antennas and Propagation in Wireless Communications (APWC)*, Sep. 2012, pp. 969–972.

[156] R. Rodriguez-Berral, C. Molero, F. Medina, and F. Mesa, "Analytical wideband model for strip/slit gratings loaded with dielectric slabs", *IEEE Transactions on Microwave Theory and Techniques*, vol. 60, no. 12, pp. 3908–3918, Dec. 2012.

[157] S. Franssila, *Introduction to microfabrication*, 2nd. John Wiley & Sons, 2010.

[158] M. Moallem and K. Sarabandi, "A non-contact submillimeter-wave s-parameters measurement technique for multiport micromachined devices", *IEEE Transactions on Terahertz Science and Technology*, vol. 4, no. 3, pp. 338–346, 2014.

[159] A. Jam, M. Vahidpour, J. East, and K. Sarabandi, "Microfabricaion and measurement of a sub-millimeterwave beam-scanning antenna array at Y-band", in *2014 XXXIth URSI General Assembly and Scientific Symposium (URSI GASS)*, IEEE, 2014, pp. 1–2.

[160] [Online]. Available: `https://www.americanpiezo.com/apc-materials/piezoelectric-properties.html`.

[161] [Online]. Available: `https://www.lpkfusa.com/products/pcb_prototyping/machines/protolaser_s/`.

[162] [Online]. Available: `https://www.piezodrive.com/actuators/ap-series-amplified-piezoelectric-actuators/`.

[163] A. Jam and K. Sarabandi, “A submillimeter-wave near-field measurement setup for on-wafer pattern and gain characterization of antennas and arrays”, *IEEE Transactions on Instrumentation and Measurement*, vol. 66, no. 4, pp. 802–811, 2017.

[164] A. B. Kozyrev, A. V. Ivanov, O. I. Soldatenkov, A. V. Tumarkin, S. V. Razumov, and S. Y. Aigunova, “Ferroelectric (Ba,Sr)TiO3 thin-film 60 GHz phase shifter”, *Technical Physics Letters*, vol. 27, no. 12, pp. 1032–1034, Dec. 2001.

[165] R. D. Paolis, S. Payan, M. Maglione, G. Guegan, and F. Coccetti, “High-tunability and high-q-factor integrated ferroelectric circuits up to millimeter waves”, *IEEE Transactions on Microwave Theory and Techniques*, vol. 63, no. 8, pp. 2570–2578, Aug. 2015.

[166] S. Bulja, D. Mirshekar-Syahkal, M. Yazdanpanahi, R. James, S. E. Day, and F. A. FernÃ¡ndez, “Liquid crystal based phase shifters in 60 ghz band”, in *The 3rd European Wireless Technology Conference*, Sep. 2010, pp. 37–40.

[167] P. Deo, D. Mirshekar-Syahkal, L. Seddon, S. E. Day, and F. A. Fernandez, “Development of 60 GHz phased antenna arrays using liquid crystal phase-shifters”, in *4th Annual Seminar on Passive RF and Microwave Components*, Mar. 2013, pp. 1–4.

[168] S. Y. Kim and G. M. Rebeiz, “A 4-bit passive phase shifter for automotive radar applications in 0.13 μm CMOS”, in *2009 Annual IEEE Compound Semiconductor Integrated Circuit Symposium*, Oct. 2009, pp. 1–4.

[169] B. Biglarbegian, M. R. Nezhad-Ahmadi, M. Fakharzadeh, and S. Safavi-Naeini, “Millimeter-wave reflective-type phase shifter in CMOS technology”, *IEEE Microwave and Wireless Components Letters*, vol. 19, no. 9, pp. 560–562, Sep. 2009.

[170] M. Tabesh, A. Arbabian, and A. Niknejad, “60 GHz low-loss compact phase shifters using a transformer-based hybrid in 65nm CMOS”, in *2011 IEEE Custom Integrated Circuits Conference (CICC)*, Sep. 2011, pp. 1–4.

[171] H.-T. Kim, J.-H. Park, S. Lee, S. Kim, J.-M. Kim, Y.-K. Kim, and Y. Kwon, “V-band 2-b and 4-b low-loss and low-voltage distributed MEMS digital phase shifter using metal-air-metal capacitors”, *IEEE Transactions on Microwave Theory and Techniques*, vol. 50, no. 12, pp. 2918–2923, Dec. 2002.

[172] J.-J. Hung, L. Dussopt, and G. M. Rebeiz, “Distributed 2- and 3-bit w-band mems phase shifters on glass substrates”, *IEEE Transactions on Microwave Theory and Techniques*, vol. 52, no. 2, pp. 600–606, Feb. 2004.

[173] S. Gong, H. Shen, and N. S. Barker, “A 60 GHz 2-bit switched-line phase shifter using SP4T RF-MEMS switches”, *IEEE Transactions on Microwave Theory and Techniques*, vol. 59, no. 4, pp. 894–900, Apr. 2011.

[174] C. C. Chang, Y. C. Chen, and S. C. Hsieh, “A V-band three-state phase shifter in cmos-mems technology”, *IEEE Microwave and Wireless Components Letters*, vol. 23, no. 5, pp. 264–266, May 2013.

[175] Y. Du, W. Su, X. Li, Y. Huang, and J. Bao, “A novel MEMS distributed phase shifter for D-band application”, in *2016 IEEE International Conference on Microwave and Millimeter Wave Technology (ICMMT)*, vol. 1, Jun. 2016, pp. 542–544.

[176] Y. Li, D. Psychogiou, S. Kuhne, J. Hesselbarth, C. Hafner, and C. Hierold, “Large stroke staggered vertical comb-drive actuator for the application of a millimeter-wave tunable phase shifter”, *Journal of Microelectromechanical Systems*, vol. 22, no. 4, pp. 962–975, Aug. 2013.

[177] A. Abdellatif, A. Taeb, N. Ranjkesh, S. Gigoyan, and S. Safavi-Naeini, “W-band piezoelectric transducer-controlled low insertion loss variable phase shifter”, *Electronics Letters*, vol. 50, no. 21, pp. 1537–1538, Oct. 2014.

[178] U. Shah, E. Decrossas, C. Jung-Kubiak, T. Reck, G. Chattopadhyay, I. Mehdi, and J. Oberhammer, “Submillimeter-wave 3.3-bit RF MEMS phase shifter integrated in micromachined waveguide”, *IEEE Transactions on Terahertz Science and Technology*, vol. 6, no. 5, pp. 706–715, Sep. 2016.

[179] A. Chakraborty and B. Gupta, “Paradigm phase shift: RF MEMS phase shifters: An overview”, *IEEE Microwave Magazine*, vol. 18, no. 1, pp. 22–41, Jan. 2017.

[180] J. Choi, Z. Qiu, C.-H. Rhee, T. Wang, and K. Oldham, “A three-degree-of-freedom thin-film PZT-actuated microactuator with large out-of-plane displacement”, *Journal of Micromechanics and Microengineering*, vol. 24, no. 7, p. 075 017, 2014.